

Advancements in Luminescent Periodic Mesoporous Organosilicas for Ion Sensing and Thermometry

Chunhui Liu
Ghent University

COMOC-Center for Ordered Materials,
Organometallics, and Catalysis
Lumilab
NanoSensing Group

Dissertation submitted in fulfillment of the requirements for the degree of
Doctor of Science: Physics

March 2024



Promoters

Promoter: Prof. Dirk Poelman

Department of Solid

State Sciences

Promotor: Prof. Anna Kaczmarek

Department of Chemistry

Promotor: Prof. Pascal Van Der Voort

Department of Chemistry

Members of the Jury

Prof. Dr. Pegie Cool

University of Antwerp

Prof. Dr. Markus Suta

Heinrich Heine University Düsseldorf

Dr. Ian Pompermayer Machado

Ghent University

Dr. David Van der Heggen

Ghent University

Prof. Dr. ir. Pieter Geiregat

Ghent University

Dr. Jeet Chakraborty

Ghent University

Ghent University

Faculty of Sciences

Department of Chemistry

Krijgslaan 281 S3, 9000 Ghent, Belgium

This research was funded by China Scholarship Council (CSC)

(201908110280).



©2023 Ghent University, Department of Chemistry, COMOC-Center for Ordered Materials, Organometallics & Catalysis, Krijgslaan 281-S3, 9000 Gent, Belgium

Alle rechten voorbehouden. Niets uit deze uitgave mag worden gereproduceerd, opgeslagen in een geautomatiseerd gegevensbestand, of openbaar gemaakt, in enige vorm of op enige wijze, hetzij elektronisch, mechanisch, door printouts, kopieën, of op welke manier dan ook, zonder voorafgaande schriftelijke toestemming van de uitgever.

All rights reserved. No part of this publication may be reproduced, stored in a retrieval system or transmitted in any form or by any means, electronic, mechanical, photocopying, recording or otherwise, without prior permission from the publisher.

ACKNOWLEDGEMENTS

This work was carried out within the Center for Ordered Materials, Organometallics, and Catalysis (COMOC) at the Department of Chemistry, Faculty of Science, Ghent University. Funding was provided by the China Scholarship Council (CSC) and Ghent University BOF (extension funding).

Upon completing this dissertation, I am overwhelmed with gratitude for the immense support I received throughout my doctoral studies. My experience at COMOC over the past four and a half years has been an enriching and invaluable chapter in my life. I am deeply honored to express my sincere thanks to my promoters, colleagues, friends, and family in this formal setting.

Firstly, my deepest gratitude and respect go to my promotor, Prof. Pascal Van Der Voort, for offering me the opportunity to pursue my PhD studies. His guidance, unwavering support, and constant inspiration have been crucial throughout my journey. I am truly grateful for his dedication to my academic development.

I extend my sincere thanks to my promoters, Prof. Anna Kaczmarek and Prof. Dirk Poelman, for their valuable guidance and insightful suggestions. Prof. Kaczmarek provided me with the opportunity to work on a luminescence PMOs project, significantly broadening my research experience. Prof. Dirk Poelman offered me the opportunity to embark on my PhD journey and provided invaluable guidance throughout. Their combined expertise and support have been crucial in shaping my research endeavors.

Special thanks go to my master's promoters, Prof. Mikhail Baklanov, Prof. Shuhua Wei, and Prof. Jing Zhang. You ignited my passion for research, introduced me to COMOC, and provided crucial guidance in applying for the CSC scholarship. Your thoughtful suggestions and warm support have been instrumental in shaping my academic journey.

I also express my heartfelt gratitude to my previous COMOC colleagues, Himanshu and Mahdieh. Himanshu, your countless support, valuable suggestions, and friendship have been deeply appreciated. I wish you continued success in your future endeavors. Mahdieh, I am grateful for sharing your lab expertise in PMO synthesis and catalysis experiments, enriching my scientific understanding.

Furthermore, I extend my heartfelt thanks to both my former and current colleagues at COMOC, Lumilab, and NanoSensing. To Sara, Parviz, Chidharth, Roy, Xiao, Jiaren, Min Zeng, Wanlu, Hui, Geert, Andreas, Laurens, Jeet, Ipsita, Wafaa, Yoran, Gilles, Diem, Sonali, and Simona, your kindness and companionship made my time at UGent truly enjoyable. I cherish every moment spent together. I am also grateful to Karen, Katrien, Kathleen, Bart, Pat, Funda, and Pierre for their kind assistance.

My sincere thanks go to my dearest friends and colleagues in S3 and S1: Jiamin (Dengxin), Yaxu, Xinyuan (Chuanguo), Zetian, Maojun (Maofan), Linyang (Wenlong), Zhongliang, Rundong, Tingting, Min Peng, and Meng. We are like a family, offering each other consistent support and encouragement throughout our journeys. You made my life in Ghent truly fulfilling and meaningful.

My deepest gratitude extends to my parents for their limitless support. Your constant encouragement and love have been my source of strength throughout my PhD journey. 谁言寸草心，报得三春晖。

I am also incredibly grateful to my girlfriend, Yanjue, for her dedicated support and invaluable contributions throughout my PhD journey. Your love and understanding have been essential to my success.

I sincerely thank the members of my PhD examination committee for dedicating their valuable time to reviewing and correcting my thesis.

Finally, I express my gratitude to the China Scholarship Council (CSC) and Ghent University (UGent) for the financial support that made this PhD journey possible.

Chunhui Liu(刘春晖)

Ghent, March 2024

SCIENTIFIC A1 PUBLICATIONS

As First Author

1. Periodic mesoporous organosilica based sensor for broad range mercury detection by simultaneous downshifting/upconversion luminescence.
Chunhui Liu, Anna M. Kaczmarek, Himanshu Sekhar Jena, Zetian Yang, Dirk Poelman and Pascal Van Der Voort, 2023, *Journal of Materials Chemistry C*, 11(17), pp.5634-5645.
2. Ratiometric Dual-Emitting Thermometers Based on Rhodamine B Dye-Incorporated (Nano) Curcumin Periodic Mesoporous Organosilicas for Bioapplications
Chunhui Liu, Simona Premcheska , Andre Skirtach, Dirk Poelman, Anna M. Kaczmarek, and Pascal Van Der Voort, 2024, accepted by *Journal of Materials Chemistry C*.
3. Acetylacetone Functionalized Periodic Mesoporous Organosilicas: from Sensing to Catalysis
Chunhui Liu, Mahdiah Haghighat, Himanshu Sekhar Jena, Dirk Poelman, Nathalie De Geyter, Rino Morent, Anna M. Kaczmarek, and Pascal Van Der Voort, 2024, submitted to *Journal of Materials Chemistry A*.

As Co-author

1. Two in one: A Brønsted acid grafted photoactive covalent organic framework as metal-free dual photocatalyst for aerobic oxidative CC cleavage.
Chen, H., Liu, W., **Liu, C.**, Sun, J., Bourda, L., Morent, R., De Geyter, N., Van Deun, R., Van Hecke, K., Leus, K. and Van Der Voort, P., 2022. *Applied Catalysis B:Environmental*, 319, p.121920.
2. Understanding photocatalytic hydrogen peroxide production in pure water for benzothiadiazole-based covalent organic frameworks
Wang, L., Sun, J., Deng, M., **Liu, C.**, Cayan, S.A., Molken, K., Geiregat, P., Morent, R., De Geyter, N., Chakraborty, J. and Van Der Voort, P., 2023. *Catalysis Science & Technology*, 13(22), pp.6463-6471.
3. Lanthanide-grafted hollow bipyridine-based periodic mesoporous organosilicas as chemical sensors
Liu, W., **Liu, C.**, Pilia, L., Zhang, H., Van Der Voort, P., Kaczmarek, A.M. and Van Deun, R., 2023. *Dalton Transactions*, 52(34), pp.11949-11957.
4. Extending the π -conjugation system of covalent organic frameworks for more efficient photocatalytic H₂O₂ production
Deng, M., Sun, J., Laemont, A., **Liu, C.**, Wang, L., Bourda, L., Chakraborty, J., Van Hecke, K., Morent, R., De Geyter, N. and Leus, K., 2023. *Green Chemistry*, 25(8), pp.3069-3076.
5. Engineering Porosity and Functionality in a Robust Two-Fold Interpenetrated Bismuth-Based MOF: Towards a Porous, Stable, and Photo-Active Material
A. Mohamed, W., Chakraborty, J., Bourda, L., Lavendomme, R., **Liu, C.**, Morent, R., De Geyter, N., Van Hecke, K., Kaczmarek, A.M. and Van Der Voort, P., 2024. *Journal of the American Chemical Society*.
6. Decoding Excimer Formation in Covalent Organic Frameworks Induced by Morphology and Ring Torsion
Chakraborty, J., Chatterjee, A., Molken, K., Nath, I., Esteban, D.A., Bourda, L., Watson, G., **Liu, C.**, Van Thourhout, D., Bals, S. and Geiregat, P., 2024. *Advanced Materials*, p.2314056.

ENGLISH SUMMARY

The PhD thesis investigates the advanced applications of luminescent periodic mesoporous organosilicas (LPMOs) in ion sensing and thermometry, exploring their unique structural, functional, and luminescent properties. The thesis is organized into several chapters, each focusing on different aspects of LPMOs:

Chapter 1 introduces the concept and significance of luminescence, focusing on the principles governing the absorption and emission of radiation by matter. It highlights the diverse applications of luminescent materials across various fields such as physics, chemistry, biology, medicine, and engineering, underscoring the interdisciplinary nature of luminescence research. The chapter delves into the fundamental theories of luminescence, including quantum mechanics and photophysics, and discusses the design and synthesis of luminescent materials. It also explores the application of these materials in sensing and thermometry, emphasizing the innovative use of luminescent periodic mesoporous organosilicas (LPMOs) for enhanced performance in these areas.

Chapter 2 introduces a material for sensitive and selective detection of mercury (Hg^{2+}) ions in water. It addresses limitations of current methods by combining the advantages of two existing technologies: lanthanide periodic mesoporous organosilicas (LnPMOs) and upconversion luminescent nanoparticles (UCNPs). LnPMOs offer good stability, biocompatibility, and potential for large-scale production, but have limited detection range. Conversely, UCNPs exhibit high sensitivity towards Hg^{2+} ions, yet suffer from a narrow detection range. The proposed material, a yolk-shell structure with a Tb^{3+} complex-grafted hollow PMO (shell) encapsulating UCNPs (yolk), aims to overcome these limitations by combining the broad detection range of LnPMOs with the high sensitivity of UCNPs for Hg^{2+} sensing. The paper details the motivation for this research, the advantages and

limitations of the chosen materials, the design and synthesis strategy for the yolk-shell structure, and the planned characterization and performance evaluation of the material in both downshifting and upconversion modes.

Chapter 3 details the innovative synthesis and multifunctional applications of acetylacetonate-functionalized periodic mesoporous organosilicas (acac-PMOs), highlighting their role in sensing and catalysis. By embedding acetylacetonate (acac) within the PMO framework, this research introduces a novel class of PMOs with enhanced sensitivity for copper ion detection and improved catalytic efficiency in Mannich reactions. The incorporation of lanthanide complexes enhances the properties of these materials, offering a promising avenue for selective ion sensing. This chapter underscores the significance of acac-PMOs in advancing material science, demonstrating their potential in environmental monitoring, catalysis, and beyond.

Chapter 4 introduces ratiometric dual-emitting thermometers based on curcumin and curcumin-pyrazole functionalized periodic mesoporous organosilicas (PMOs), integrated with Rhodamine B (RhB) dye. These innovative materials, denoted as C-PMO and CP-PMO, exploit the stable, porous structure of PMOs and the luminescent properties of curcumin derivatives for enhanced temperature sensitivity and biocompatibility. Encapsulation of RhB within these frameworks, further enveloped by a lipid bilayer, significantly amplifies their temperature-dependent fluorescence response, achieving exceptional sensitivity within physiological ranges. This advancement shows precise, non-invasive temperature monitoring for biomedical applications, characterized by their dual-emitting capabilities, optimized for accurate and reliable sensing.

DUTCH SUMMARY

Dit proefschrift onderzoekt de geavanceerde toepassingen van luminescerende periodieke mesoporiöse organosilicaten (LPMO's) in ionensensoren en thermometers. Hierbij worden hun unieke structurele, functionele en luminescerende eigenschappen verkend.

Het proefschrift is verdeeld in verschillende hoofdstukken, elk gericht op verschillende aspecten van LPMO's:

Hoofdstuk 1: introduceert het concept en belang van luminescentie. De nadruk ligt op de principes die de absorptie en emissie van straling door materie bepalen. De diversiteit aan toepassingen van luminescerende materialen in verschillende vakgebieden, zoals natuurkunde, scheikunde, biologie, geneeskunde en techniek, wordt benadrukt, wat het interdisciplinaire karakter van luminescentieonderzoek onderstreept. Het hoofdstuk behandelt de fundamentele theorieën van luminescentie, waaronder quantummechanica en fotofysica, en bespreekt het ontwerp en de synthese van luminescerende materialen. Daarnaast wordt de toepassing van deze materialen in sensortechnologie en thermometers behandeld, met nadruk op het innovatieve gebruik van luminescerende periodieke mesoporiöse organosilicaten (LPMO's) voor verbeterde prestaties op deze gebieden.

Hoofdstuk 2: introduceert een materiaal voor gevoelige en selectieve detectie van kwik (Hg^{2+}) -ionen in water. Het pakt de beperkingen van huidige methoden aan door de voordelen te combineren van twee bestaande technologieën: lanthanide-periodieke mesoporiöse organosilicaten (LnPMO's) en upconversie-luminescente nanodeeltjes (UCNP's). LnPMO's bieden goede stabiliteit, biocompatibiliteit en potentie voor grootschalige productie, maar hebben een beperkt detectiebereik. UCNP's daarentegen vertonen een hoge gevoeligheid voor Hg^{2+} -ionen, maar hebben een smal detectiebereik. Het voorgestelde materiaal, een dooier-schilstructuur met

een Tb³⁺-complex-geënt holle PMO (schil) die UCNP's (dooier) inkapselt, beoogt deze beperkingen te overwinnen door het brede detectiebereik van LnPMO's te combineren met de hoge gevoeligheid van UCNP's voor Hg²⁺-detectie. In dit hoofdstuk worden de motivatie voor dit onderzoek, de voordelen en beperkingen van de gekozen materialen, de ontwerp- en synthese-strategie voor de dooierschilstructuur en de geplande karakterisering en prestatie-evaluatie van het materiaal in zowel downshifting- als upconversie-modi gedetailleerd beschreven.

Hoofdstuk 3: beschrijft de innovatieve synthese en multifunctionele toepassingen van acetylaceton-gefunctionaliseerde periodieke mesoporiöse organosilicaten (acac-PMO's), met de nadruk op hun rol in sensortechnologie en katalyse. Door acetylaceton (acac) in het PMO-framework te embedden, introduceert dit onderzoek een nieuwe klasse PMO's met een verhoogde gevoeligheid voor koperionendetectie en een verbeterde katalytische efficiëntie in Mannich-reacties. De integratie van lanthanidecomplexen verbetert de eigenschappen van deze materialen, wat een veelbelovende weg biedt voor selectieve ionensensoren. Dit hoofdstuk onderstreept het belang van acac-PMO's in de vooruitgang van materiaalwetenschappen en toont hun potentieel in milieumonitoring, katalyse en andere toepassingen.

Hoofdstuk 4: introduceert ratiometrische dubbel-emitterende thermometers gebaseerd op curcumine en curcumine-pyrazole gefunctionaliseerde periodieke mesoporiöse organosilicaten (PMO's), geïntegreerd met Rhodamine B (RhB) kleurstof. Deze innovatieve materialen, genaamd C-PMO en CP-PMO, benutten de stabiele, poreuze structuur van PMO's en de luminescerende eigenschappen van curcuminederivaten voor verbeterde temperatuurgevoeligheid en biocompatibiliteit. Inkapseling van RhB in deze frameworks, verder omhuld door een lipide-dubbellaag, versterkt hun temperatuurafhankelijke fluorescentiereactie.

LIST OF ABBREVIATIONS AND ACRONYMS

A

acac-Br 1,3-bis(4-bromophenyl)propane-1,3-dione

acac-Si 1,3-bis(4-((E)-2-(triethoxysilyl)vinyl)phenyl)propane-1,3-dione

APTES 3-aminopropyltriethoxysilane

B

BA-Si 3,5-bis(3-(3-(triethoxysilyl)propyl)ureido)benzoic acid

BTESE 1,2-bis(triethoxysilyl)ethane

C

CDCl₃ deuterated chloroform

CHNS elemental analysis

COFs covalent Organic Frameworks

CTAB cetyltrimethylammonium bromide

Curcumin-Pyrazole Analog 4,4'-((1E,1'E)-(1H-pyrazole-3,5-diyl) bis(ethene-2,1-diyl)) bis(2-methoxyphenol)

Curcumin-Pyrazole-Si 2,2'-(((1E,1'E)-(1H-pyrazole-3,5-diyl) bis(ethene-2,1-diyl)) bis(2-methoxy-4,1-phenylene))bis(N-(3-(triethoxysilyl)propyl)acetamide)

Curcumin-Si 4-((1E,4Z,6E)-5-hydroxy-7-(3-methoxy-4-((3-(triethoxysilyl)propyl) carbamoyl)oxy)phenyl)-3-oxohepta-1,4,6-trien-1-yl)-2-methoxyphenyl (3-(triethoxysilyl)propyl) carbamate

D

DMEM	Dulbecco's Modified Eagle Medium
DMF	dimethylformamide
DMSO	dimethyl sulfoxide
DMSO-d₆	Dimethyl sulfoxide-d ₆
DOPC	1,2-dioleoyl-sn-glycero-3-phosphocholine
DRIFTS	diffuse reflectance infrared Fourier transform spectroscopy
DS	downshifting
E	
EDX	energy dispersive X-ray
ETS	energy transfer from singlet
ETT	energy transfer from triplet
F	
FBS	Fetal Bovine Serum
FRET	Förster resonance energy transfer
FT-IR	Fourier Transform Infrared
H	
Hacac	acetylacetone
Hdbm	dibenzoylmethane
Hhfa	hexafluoroacetone
HPMO	hollow periodic mesoporous organosilica
HRTEM	high-resolution transmission electron microscopy
Htfac	1,1,1-trifluoroacetylacetone
Htta	2-thenoyltrifluoroacetone
I	
ICP-MS	inductively coupled plasma mass spectrometry

ICPTES	(3-Isocyanatopropyl)triethoxysilane
ISC	intersystem crossing
L	
LB	lipid bilayer
Ln	lanthanide
Ln³⁺	lanthanide ions
Ln-CQDs	lanthanide hybridized carbon quantum dots
LnMOFs	lanthanide metal-organic frameworks
LOD	limit of detection
M	
MCT	Mercury Cadmium Telluride
MOFs	metal organic frameworks
MR	multiphonon relaxation
N	
NaH	Sodium hydride
NHDF	
NIR	near-infrared
NMR	Nuclear Magnetic Resonance
NPs	nanoparticles
P	
PEO	polyethylene oxide
PL	photoluminescence
PMO	periodic mesoporous organosilica
PMOs	periodic mesoporous organosilicas
PPO	polypropylene
PSD	Pore Size Distribution THF Tetrahydrofuran

PXRD	powder X-ray diffraction
Q	
QC	quantum cutting
QDs	quantum dots
S	
S_{0,1}	singlet
SEM	scanning electron microscopy
SiO₂	silica
STEM	scanning transmission electron microscopy
T	
T₁	triplet
Tb(hfac)₃·n(H₂O)	Tb(III) tris-hexafluoroacetylacetonate hydrates
TEM	transmission electron microscopy
TEOS	tetraethyl orthosilicate
TGA	thermogravimetry
THF	tetrahydrofuran
TOF	Turnover Frequency
TON	Turnover Number
tta	2-Thenoyltrifluoroacetone
U	
UC	upconversion
UCNP	upconversion nanoparticle
UV	ultraviolet
V	
V₂O₅	Vanadium(V) oxide

VO(acac)₂	Vanadyl acetylacetonate
X	
XPS	X-ray Photoelectron Spectroscopy
XRD	X-ray Diffraction
XRF	X-ray Fluorescence

Contents

Chapter 1. Introduction.....	21
1.1 The Essence of Luminescence	22
1.2 Luminescence Terminology: Clarifying Key Concepts	23
1.3 Lanthanide Luminescence	28
1.4 Periodic Mesoporous Organosilicas (PMOs): Structure, Luminescence, and Functionalization	37
1.4.1 Structural Characteristics of PMOs	37
1.4.2 Synthesis of PMO hybrids	40
1.4.3 Luminescent PMOs	42
1.5 Luminescent PMOs in Sensing Applications.....	49
1.5.1 PMOs as sensors	49
1.5.2 Metal ion sensors.....	51
1.5.3 Temperature sensors	52
1.6 Aims of This Thesis	54
1.7 Reference	56
Chapter 2. Periodic Mesoporous Organosilica Based Sensor for Broad Range Mercury Detection by Simultaneous Downshifting / Upconversion Luminescence	59
2.1 Introduction.....	61
2.2 Experimental.....	66
2.2.1 Materials and Instrumentation	66
2.2.2 Synthesis.....	67
2.3 Results and Discussion.....	70
2.3.1 Characterization of LnHPMO@UCNP.....	70
2.3.2 Downshifting mode: sensing performance of the shell, LnHPMO	74
2.3.3 Upconversion mode: sensing performance of the yolk: UCNP+RBT	81
2.3.4 Revalidation of the DS mode: sensing performance of LnHPMO@UCNP.....	86
2.4 Conclusions.....	88
2.5 Supporting information	89
2.6 Reference.....	91
Chapter 3. Acetylacetone Functionalized Periodic Mesoporous Organosilicas: from Sensing to Catalysis.....	94

3.1 Introduction.....	96
3.2 Experimental.....	98
3.2.1 Materials and Instrumentation	98
3.2.2 Synthesis.....	99
3.2.2.1 1,3-bis(4-bromophenyl)propane-1,3-dione (acac-Br)	99
3.2.2.2 1,3-bis(4-((E)-2-(triethoxysilyl)vinyl)phenyl)propane-1,3-dione (acac-Si)	99
3.2.2.3 Synthesis of mesoporous Acetylacetonate-PMO (acac-PMO)	100
3.2.2.4 Synthesis of the Eu(III) complex [Eu(tta) ₃ (H ₂ O) ₂]	101
3.2.2.5 Synthesis of Eu grafted Acetylacetonate-PMO (acac-PMO@Eu_tta).....	101
3.2.2.6 Synthesis of V grafted Acetylacetonate-PMO (acac-PMO@VO_acac).....	102
3.3 Results and discussion	102
3.3.1 Synthesis and characterization of acac-PMOs	102
3.3.2 Luminescence properties.....	106
3.3.3 Catalytic properties.....	113
3.4 Conclusions.....	119
3.5 Supporting information.....	121
3.6 Reference	125
Chapter 4. Ratiometric Dual-Emitting Thermometers Based on Rhodamine B Dye-Incorporated (Nano) Curcumin Periodic Mesoporous Organosilicas for Bioapplications	128
4.1 Introduction.....	130
4.2 Experimental.....	134
4.2.1 Materials and Instrumentation	134
4.2.2 Synthesis	135
4.2.2.1 Synthesis of 4-((1E,4Z,6E)-5-hydroxy-7-(3-methoxy-4-((3-(triethoxysilyl) propyl) carbamoyl)oxy)phenyl)-3-oxohepta-1,4,6-trien-1-yl)-2-methoxyphenyl (3- (triethoxysilyl) propyl) carbamate (Curcumin-Si, 1b)	135
4.2.2.2 Synthesis of 4,4'-((1E,1'E)-(1H-pyrazole-3,5-diyl) bis(ethene-2,1-diyl)) bis(2- methoxyphenol) (Curcumin-Pyrazole Analog, 1c).....	136
4.2.2.3 Synthesis of 2,2'-(((1E,1'E)-(1H-pyrazole-3,5-diyl) bis(ethene-2,1-diyl)) bis(2- methoxy-4,1-phenylene))bis(N-(3-(triethoxysilyl)propyl)acetamide) (Curcumin- Pyrazole-Si, 1d).....	136

4.2.2.4 Synthesis of mesoporous Curcumin-PMO (C-PMO) nanoparticles and Curcumin-Pyrazole PMO(CP-PMO).....	137
4.2.2.5 Preparation of PMO@dye	137
4.2.2.6 Preparation of PMO@dye@LB (hybrid nanocomposites with lipid bilayer)...	138
4.2.3 Cytotoxicity test.....	138
4.2.3.1 Cell cultures:	138
4.2.3.2 Cell viability assay:	138
4.3 Results and discussion	140
4.3.1 Structural characteristics of PMO@dye@LB	140
4.3.2 Temperature-Related Fluorescence of PMO@dye@LB.....	144
4.3.2.1 Fluorescence of the prepared PMO@dye@LB.....	144
4.3.2.2 Ratiometric temperature sensing properties of PMO@dye@LB	147
4.3.3 PrestoBlue™ HS cell viability assay conducted on NHDF cell line.....	153
4.4 Conclusions.....	157
4.5 Supporting information	159
4.6 Reference	171
CHAPTER 5. Conclusion and Perspectives	173

Chapter 1. Introduction

1.1 The Essence of Luminescence

Light, a form of electromagnetic radiation, requires energy conversion for its creation. Two main mechanisms achieve this: incandescence and luminescence. This study explores luminescence, a process that generates light at low temperatures through electronic transitions. This is distinct from thermal emission, which produces light due to heat, as observed in the black-body radiation of incandescent lamps.

The term "luminescence" was first introduced by Eilhard Wiedemann, a German physicist and science historian, deriving from the Latin word "Lumen," which means light.¹ Luminescence, broadly defined, encompasses the study of the principles governing the absorption and emission of radiation by matter.² This phenomenon is characterized as a cool emission, resulting from the transition of electrons within a substance from higher to lower energy states. Notably, this process of light emission occurs at normal or low temperatures, distinguishing it from processes that generate heat. Luminescence can be triggered by various mechanisms, including the absorption of photons, chemical or biochemical reactions, the action of subatomic particles, exposure to radiation, or mechanical stress applied to a crystal.

A unique aspect of luminescence is that the wavelength of the emitted light is specific to the luminescent material itself, rather than being dependent on the wavelength of the incident radiation.^{3, 4} This principle is encapsulated in the law of luminescence (downshifting), which states that the wavelength of emitted radiation (λ_{emi}) is always longer than that of the exciting radiation (λ_{exc}). Materials that exhibit luminescence are referred to as luminophores or phosphors.⁵ An illustration of the luminescence process is provided in Figure 1.1.

Luminescence is a multidisciplinary field, finding applications in various domains such as physics, chemistry, biological science, medical science, forensic science, geology, material science, and engineering. The current research landscape in this area is marked by a significant interplay among different branches of solid-state science and various subfields of luminescence, involving both inorganic and organic materials.

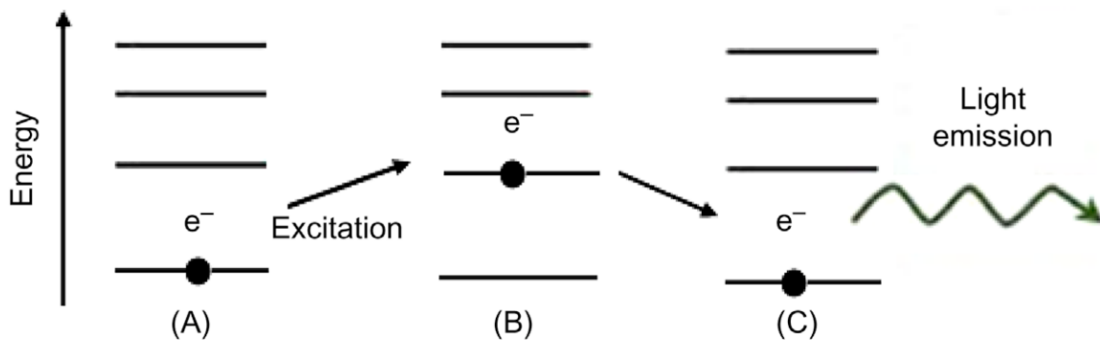


Figure 1.1 Schematic diagram of the luminescence process: (A) electron in lowest energy state, (B) excited state, and (C) light emission.⁶

1.2 Luminescence Terminology: Clarifying Key Concepts

This section aims to provide clear and concise definitions of essential terms related to the phenomenon of luminescence.

1. Phosphor:

A phosphor refers to a solid material, either naturally occurring or synthetic, that exhibits luminescence, characterized by the emission of light upon exposure to various forms of energy, including radiation, ultraviolet (UV) light, or electron beams. These materials are also known as luminescent materials. Typically, phosphors appear as microcrystalline powders or thin films designed to emit visible colors. In a broader sense, the term "phosphor" can be used interchangeably with "solid luminescent material" and has been in use since the early 17th century.

2. Luminescence Center:

The crystal lattice of a phosphor often incorporates activator ions, introducing localized energy levels within the forbidden band gap. These localized levels, referred to as luminescence centers, play a crucial role in enabling efficient luminescence. They absorb excitation energy and subsequently convert it into visible radiation through an electron transition process. In essence, luminescence centers act as the sites where absorbed energy is captured, leading to its subsequent re-emission as light.

- Dopant: also known as a doping agent, refers to a trace amount of a foreign element intentionally introduced into a material. Doping is typically employed to modify the material's electrical or optical properties in a controlled manner. The concentration of the dopant is generally very low, often representing a small fraction of a percent.
- Activator: In the context of luminescent materials like phosphors and scintillators, an activator is a specific type of dopant used in minute quantities to enhance the luminescence process. Activators introduce additional energy levels within the host material, facilitating efficient conversion of absorbed energy into light emission.

3. Chromophore:

A chromophore is a group of atoms within a molecule that interacts with light. This interaction can manifest in two ways: absorption of specific wavelengths of visible light or emission of light at different wavelengths. The absorbed wavelengths correspond to the energy difference between the chromophore's ground state and its excited electronic states. This interaction with light is responsible for a molecule's color and can also lead to the emission of light, a phenomenon known as luminescence.

4. Sensitizer:

Not all luminescent materials involve direct excitation of the activator. In certain cases, a different ion or molecule within the material can absorb the excitation energy and subsequently transfer it to the activator. This intermediary species responsible for energy transfer is known as a sensitizer.

5. Quenching:

Quenching refers to the deactivation of an excited state through a non-radiative pathway, meaning energy is lost without the emission of light. Two common types of quenching are:

- Concentration quenching: This phenomenon occurs when the concentration of activators in the host material exceeds a critical value. At high activator concentrations, the probability of energy transfer between neighboring activators increases, leading to non-radiative energy loss before emission can occur (Figure 1.2).

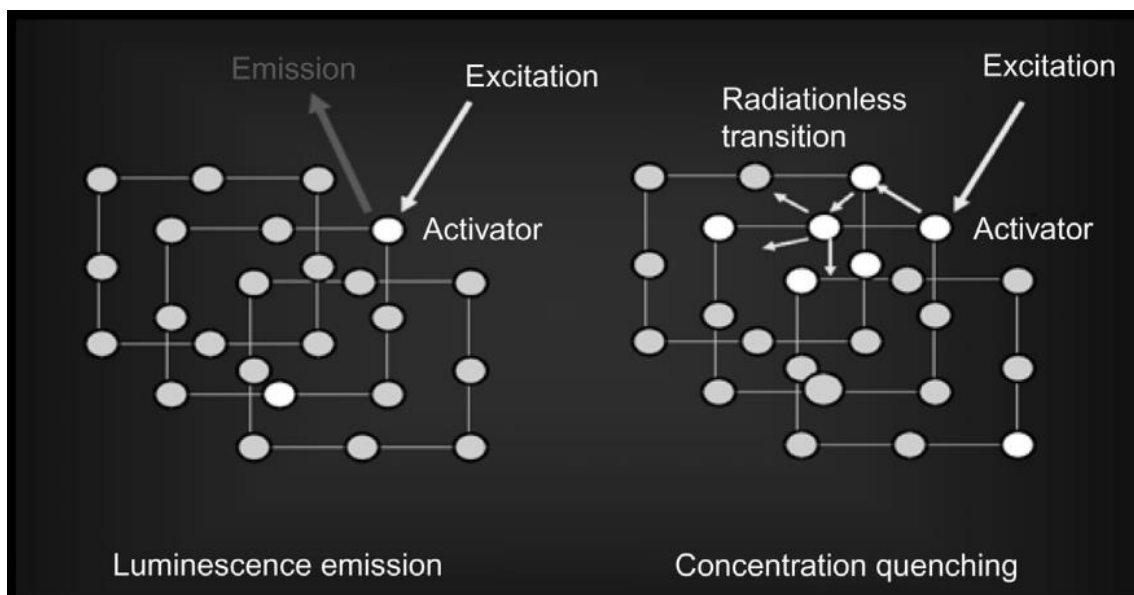


Figure 1.2 Concentration quenching.⁶

- Thermal quenching: At elevated temperatures, the increased thermal energy within the host lattice can contribute to non-radiative energy loss, diminishing the luminescence efficiency. This phenomenon is known as

thermal quenching. For optimal luminescence performance at elevated temperatures, materials with low phonon frequencies are often preferred. Lower phonon frequencies within the host lattice minimize the probability of non-radiative energy transfer to lattice vibrations, thereby reducing thermal quenching. For example, some inorganic compounds like Yttrium Aluminum Garnet (YAG) exhibit relatively low phonon frequencies, making them suitable hosts for lanthanide ions in high-power applications like solid-state lighting.⁷

6. Singlet State:

In the context of molecular electronic states, a singlet state refers to a state where all electron spins are paired. In other words, the spin of the excited electron in the singlet state remains paired with the spin of the electron in the ground state.

7. Triplet State:

In the realm of quantum mechanics, a triplet state refers to a specific type of quantum state exhibited by a system, such as a molecule or atom. This state is characterized by a total spin quantum number (S) of 1. As a consequence, the spin component (M_s) can possess three allowed values: -1, 0, and +1. Figure 1.3 visually depicts the energy level diagram illustrating the spin configuration in both singlet and triplet states.

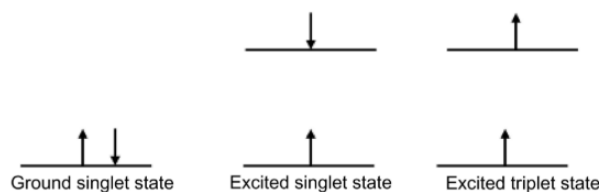


Figure 1.3 Energy-level diagram showing singlet and triplet states.⁶

8. Relaxation Processes:

Following excitation, molecules or excitons can undergo various relaxation processes to return to their ground state:

- **Internal Conversion:** This process describes the non-radiative transition of a molecule from a higher to a lower electronic state within the same spin multiplicity (e.g., singlet-to-singlet or triplet-to-triplet). During internal conversion, the excess energy is dissipated through various non-radiative pathways, such as vibrations within the molecule. The efficiency of internal conversion is often higher when the energy levels involved are close enough to allow for significant overlap between their associated vibrational levels.
- **Intersystem Crossing:** In contrast to internal conversion, intersystem crossing involves the transition between electronic states of different spin multiplicity. For example, this process could describe the conversion of a molecule from a singlet state to a triplet state (or vice versa). Intersystem crossing is generally a slower process compared to internal conversion due to the selection rules governing these transitions.

9. Stokes Shift:

Named after Irish physicist George G. Stokes, the Stokes shift refers to the difference in wavelength or frequency between the absorption and emission maxima of the same electronic transition within a molecule or material (Figure 1.4). This difference arises because the equilibrium positions of atoms within a molecule or crystal lattice can differ between the ground and excited states. Larger Stokes shifts are often associated with lower thermal quenching at elevated temperatures.

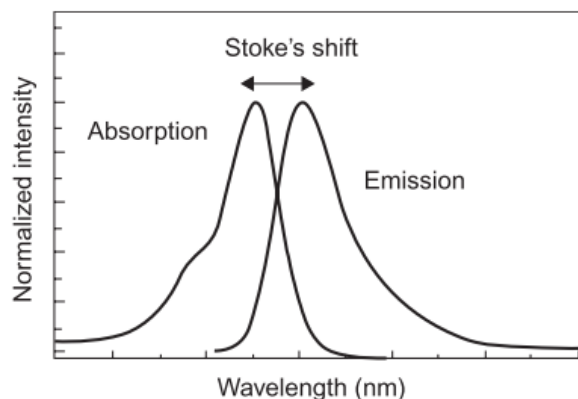


Figure 1.4 Absorption and emission spectra showing Stokes shift.⁶

1.3 Lanthanide Luminescence

Trivalent lanthanide (Ln^{3+}) ions exhibit unique luminescent properties due to their electronic configurations and the energy level distribution within their partially filled 4f subshells. Unlike most transition metals, the 4f electrons in lanthanides are shielded from the surrounding chemical environment by filled $5s^2$ and $5p^6$ orbitals. This shielding effect minimizes interactions with the surrounding ligands, leading to the characteristic sharp and narrow emission bands observed in lanthanide luminescence.⁸ The specific electron configuration adopted by a trivalent lanthanide element, either $[\text{Xe}]4f^n6s^2$ or $[\text{Xe}]4f^{n-1}5d^16s^2$, is governed by the relative energy levels of these configurations (Table 1.1). This is illustrated in Figure 1.5. An exception exists for cerium (Ce^{3+}). Due to the unique energy level structure, its first excited state involves the 5d orbital, resulting in broader absorption and emission bands compared to other lanthanides.⁹

Table 1.1 Electron configurations of the lanthanides and their common ions.⁸

	Atom	Ln ³⁺	Ln ⁴⁺	Ln ²⁺
La	[Xe] 5d ¹ 6s ²	[Xe]		
Ce	[Xe] 4f ¹ 5d ¹ 6s ²	[Xe] 4f ¹	[Xe]	
Pr	[Xe] 4f ³ 6s ²	[Xe] 4f ²	[Xe] 4f ¹	
Nd	[Xe] 4f ⁴ 6s ²	[Xe] 4f ³	[Xe] 4f ²	[Xe] 4f
Pm	[Xe] 4f ⁵ 6s ²	[Xe] 4f ⁴		
Sm	[Xe] 4f ⁶ 6s ²	[Xe] 4f ⁵		[Xe] 4f ⁶
Eu	[Xe] 4f ⁷ 6s ²	[Xe] 4f ⁶		[Xe] 4f ⁷
Gd	[Xe] 4f ⁷ 5d ¹ 6s ²	[Xe] 4f ⁷		
Tb	[Xe] 4f ⁹ 6s ²	[Xe] 4f ⁸	[Xe] 4f ⁷	
Dy	[Xe] 4f ¹⁰ 6s ²	[Xe] 4f ⁹	[Xe] 4f ⁸	[Xe] 4f ¹⁰
Ho	[Xe] 4f ¹¹ 6s ²	[Xe] 4f ¹⁰		
Er	[Xe] 4f ¹² 6s ²	[Xe] 4f ¹¹		
Tm	[Xe] 4f ¹³ 6s ²	[Xe] 4f ¹²		[Xe] 4f ¹³
Yb	[Xe] 4f ¹⁴ 6s ²	[Xe] 4f ¹³		[Xe] 4f ¹⁴
Lu	[Xe] 4f ¹⁴ 5d ¹ 6s ²	[Xe] 4f ¹⁴		

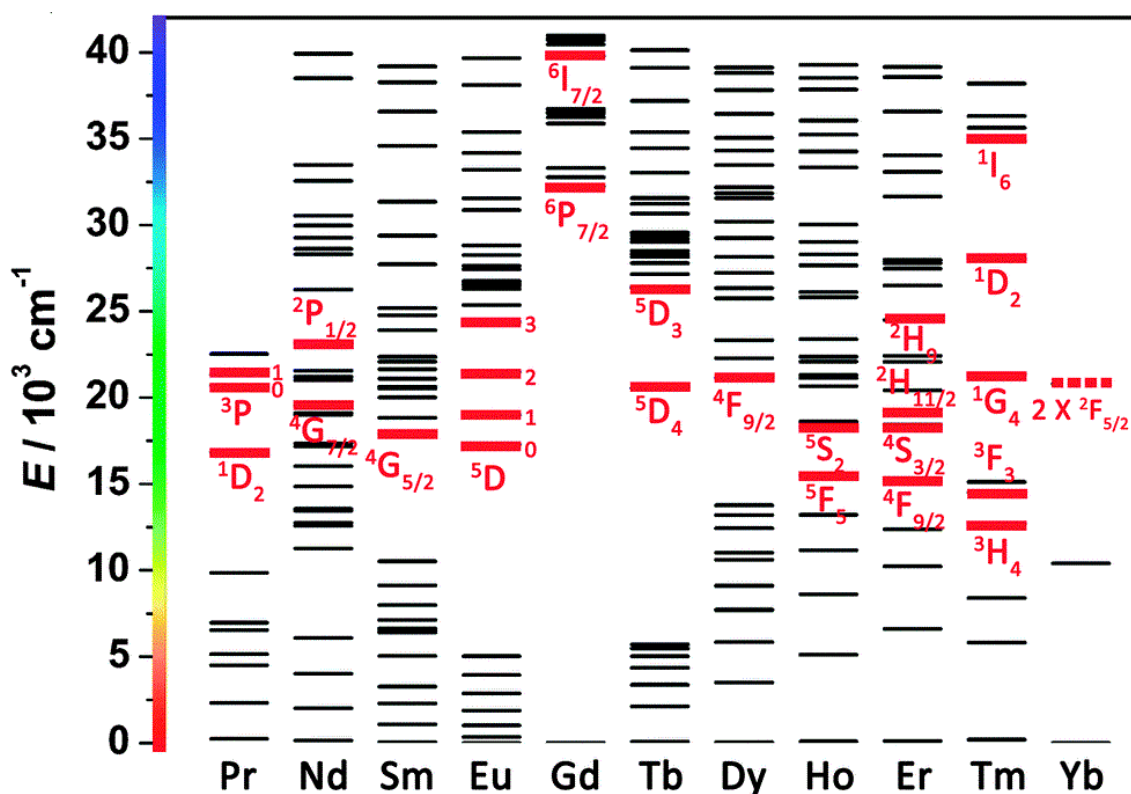


Figure 1.5 Energy level diagrams of trivalent Ln³⁺ ions (except Ce³⁺, La³⁺, and Lu³⁺). Corresponding typical upconversion emissive excited levels are highlighted with red bold lines, which will be further explained.⁹

The Antenna Effect: Sensitized Emission

Nature, through the process of evolution, has remarkably engineered light-harvesting antenna systems in organisms. These systems efficaciously capture solar energy and subsequently transfer it as electronic excitation energy to reaction centers. This excitation ultimately drives the conversion of light energy into chemical

energy through redox reactions.¹⁰ In the realm of artificial systems, the term "antenna effect" was introduced to describe the phenomenon in sensitized luminescence.¹¹ This effect involves the enhancement of the luminescence from weakly absorbing lanthanide ions through the excitation of strongly absorbing ligands, which then transfer the energy to the lanthanide ions.

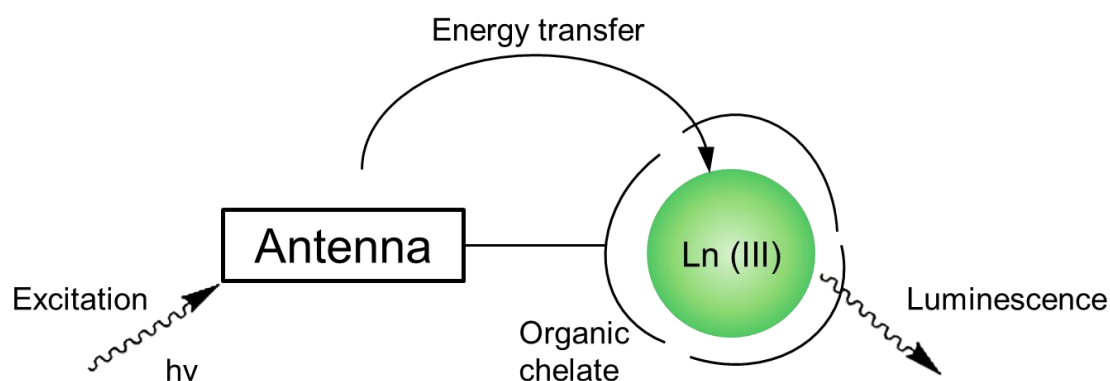


Figure 1.6 Illustration of antenna effect.

The antenna effect, prominent in lanthanide-organic chelate complexes, is exemplified in Figure 1.6. By incorporating an antenna, an alternative energy transfer pathway facilitates enhanced excitation of the lanthanide emitting levels, which subsequently emit light upon relaxation to the ground state.¹²⁻¹⁴

For optimal sensitization in lanthanide complexes, an antenna chromophore should generally fulfill the following criteria:

- High molar extinction coefficient: Ensures efficient light absorption for high photoluminescence quantum yield;
- Energy level compatibility: The triplet state energy of the antenna should align closely with the lanthanide luminescent states, promoting effective energy transfer while minimizing back-transfer due to thermal activation;
- Spatial proximity: Close proximity between the antenna and lanthanide ion is essential for effective energy transfer;

- High intersystem crossing (ISC) yield: Promotes efficient population of the triplet state;
- Coordination saturation: The antenna should fully occupy the inner coordination sphere of the lanthanide (coordination number of at least 8) to minimize quenching by water or other solvent molecules.

The selection of antenna ligands for lanthanide ions critically depends on their emission wavelengths:

- Visible-emitting Ln^{3+} ions: These require UV-absorbing chromophores as antenna ligands;
- NIR (Near-infrared)-emitting Ln^{3+} ions: These necessitate antenna ligands with singlet and triplet state energies closely matching the accepting levels of the Ln^{3+} ions for efficient energy transfer.

Commonly employed organic antenna ligands for Ln^{3+} coordination include:

- β -Diketones: These encompass ligands like acetylacetonate (Hacac), 1,1,1-trifluoroacetylacetonate (Htfac), hexafluoroacetonate (Hhfa), 2-thenoyltrifluoroacetonate (Htta), and dibenzoylmethane (Hdbm);
- Dipicolinic acid and its derivatives: These offer further options for antenna design;
- Macrocyclic ligands: These provide additional avenues for tailoring luminescent properties.

Ligand and Lanthanide Ion Excitation: Jablonski Diagram

The process of ligand-enhanced lanthanide luminescence can be summarized in three key steps:¹³

- Ligand Excitation: Light absorption promotes the ligand from its ground state (S_0) to a short-lived singlet excited state (S_1);

- Intersystem Crossing (ISC): The S_1 state rapidly undergoes ISC, populating the ligand's longer-lived triplet state (T_1). This process is typically faster than radiative or non-radiative decay from S_1 ;
- Energy Transfer: The excited ligand transfers energy to the lanthanide ion, exciting its electrons to higher energy levels. While direct transfer from S_1 to the lanthanide can occur, it's less efficient than energy transfer from T_1 due to the short lifetime of S_1 .

Importantly, the energy levels of the ligand play a crucial role in this process. The ligand's singlet (S_1) and triplet (T_1) states must be positioned energetically close to facilitate efficient energy transfer to the emissive states of the lanthanide ion. The Jablonski diagram (Figure 1.7) provides a schematic representation of the energy levels and transitions associated with lanthanide luminescence. Energy states of both the ligand and lanthanide are arranged vertically according to energy, while horizontal groupings denote distinct spin multiplicities. This simplifies the diagram for overall energy transfer processes. The energy from the excited rare earth ion (Eu^{3+}) needs an acceptor to be efficiently transferred via RET. This acceptor could be:

Another ligand molecule: In this case, the RET would be followed by ligand emission at a longer wavelength (Stokes shift) compared to the initial excitation energy.

A solvent molecule: Similar to ligand acceptor, the solvent molecule would accept the energy and emit luminescence at a lower energy.

A quencher molecule: This molecule would absorb the emission energy from Eu^{3+} , preventing luminescence altogether.

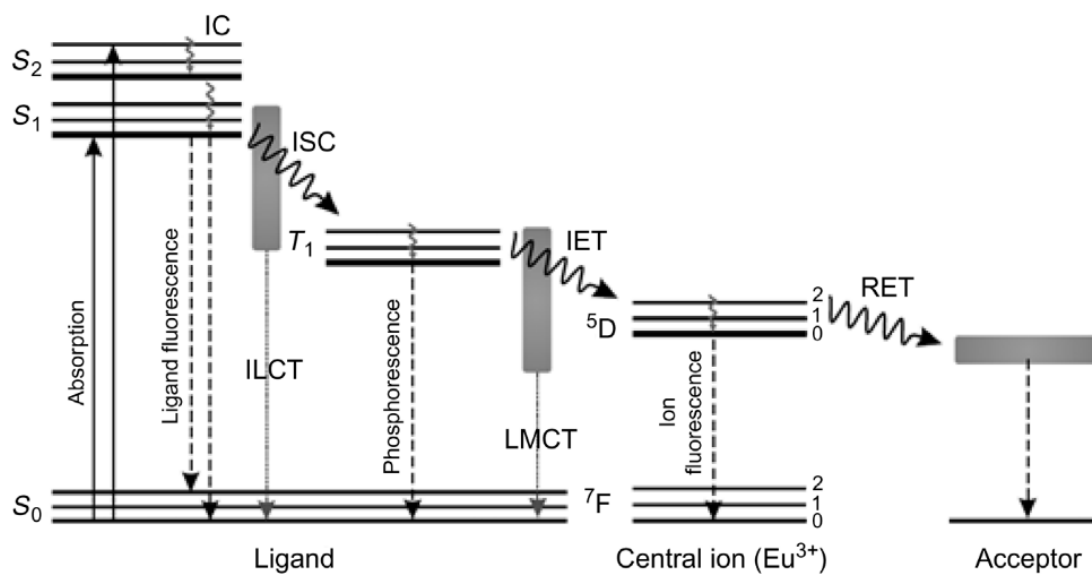


Figure 1.7 Illustration of lanthanide luminescence by the Jablonski diagram,^{6, 15} where IC, internal conversion; ISC, intersystem crossing; ILCT, intraligand charge-transfer; LMCT, ligand-to-metal charge transfer; IET, intramolecular energy transfer; RET, rare earth transition.

Lanthanide complexes exhibit exceptionally rapid absorption of photons, occurring on a timescale of approximately 10^{-15} seconds. This phenomenon can be attributed to the inherent tendency of electrons in unexcited molecules to occupy the energetically lowest available orbitals, known as the ground state. Notably, most lanthanide complexes are excited by light in the near-ultraviolet (near-UV) region, with wavelengths typically not exceeding 350 nm. This specific excitation wavelength range is crucial for initiating the luminescence process. Following excitation by a photon, the initially populated singlet excited state of the ligand can undergo non-radiative decay via a process termed internal conversion. This process occurs within a picosecond (10^{-12} s) and involves the relaxation of the excited electron to a higher vibrational level within the same electronic state, ultimately reaching the lowest excited electronic level. The subsequent sensitization process, which involves the transfer of excitation energy to the central lanthanide ion, can proceed through various pathways. These pathways encompass diverse ligand states, including singlet and triplet excited states as well as intraligand charge-transfer (ILCT) states. Traditionally, the predominant understanding suggests that

energy transfer commences with intersystem crossing from the ligand's singlet state to its triplet state.¹⁶⁻¹⁸ This is followed by intramolecular energy transfer from the lowest-lying ligand triplet state to the excited energy levels of the central lanthanide ion. While less common, direct energy transfer from the ligand's singlet state to the central ion can occur. However, the short lifetime of the singlet state renders this pathway inefficient.¹⁹

Lanthanide Sensitization Mechanisms: Förster Resonance Energy Transfer (FRET) and Dexter Energy Transfer

Ligand-to-metal energy transfer (LMET) in lanthanide complexes plays an important role in their luminescence properties. Two primary mechanisms govern LMET: Förster resonance energy transfer (FRET) and Dexter energy transfer (Figure 1.8).

Förster Resonance Energy Transfer (FRET):²⁰

FRET is a through-space mechanism dependent on Coulombic dipole-dipole interaction between the excited ligand (donor) and the Ln³⁺ ion (acceptor). The transfer operates effectively over larger donor-acceptor distances (1-10 nm), exhibiting a characteristic 1/r⁶ dependence. Efficient FRET necessitates spectral overlap between the ligand's emission spectrum and the Ln³⁺ ion's absorption spectrum.

Dexter Energy Transfer:²¹

Dexter energy transfer relies on electron exchange between the ligand and the Ln³⁺ ion. Due to its dependence on electron exchange, Dexter transfer is limited to very close proximity (<1 nm), exhibiting an exponential distance dependence (e^{-r}). Similar to FRET, Dexter transfer also requires spectral overlap between the ligand's emission spectrum and the Ln³⁺ ion's absorption spectrum.

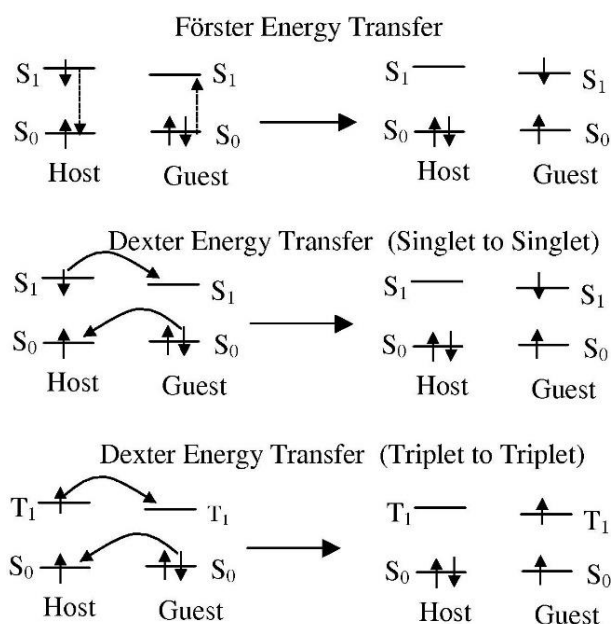


Figure 1.8 Schematics of the Förster and Dexter mechanisms.²²

Lanthanide Luminescence Processes: Downshifting, Quantum Cutting, and Upconversion

Lanthanide ions (Ln^{3+}) exhibit diverse luminescence processes, offering a spectrum of potential applications in various fields. This section delves into three prominent categories of these processes: downshifting, quantum cutting, and upconversion (Figure 1.9).

Downshifting (DS),²³ also known as photoluminescence (PL) or Stokes shift, refers to the standard luminescence process. It involves the absorption of a high-energy photon followed by the emission of one lower-energy photon. This process inherently limits its quantum efficiency to 100% or less.

Quantum Cutting (QC),²⁴ is a fascinating process where the energy of a single absorbed photon is converted into two or more lower-energy photons. This process can achieve a quantum efficiency exceeding 100% (up to 200%). QC can occur within single lanthanide ions, particularly Pr^{3+} and Gd^{3+} , or between different sets of Ln^{3+} ions through energy transfer. Notably, the most efficient energy transfer has been

observed between Gd^{3+} (in the host matrix) and other Ln^{3+} ions like Eu^{3+} , Tb^{3+} , and Er^{3+} .

Upconversion (UC),²⁵ is a non-linear process where two or more photons (often in the infrared range) are converted into a single, higher-energy photon (typically visible or UV). Due to its non-linear nature, UC exhibits a considerably lower quantum efficiency, typically well below 50%. It means that UC typically requires a high pump power (Figure 1.9 right). Furthermore, minimizing non-radiative losses is crucial, which necessitates the use of low phonon frequency hosts. Lanthanide ions like Er^{3+} , Ho^{3+} , and Tm^{3+} are frequently employed as activators due to their favorable ladder-like energy level structures, enabling efficient visible emissions under low pump power densities.²⁶ Yb^{3+} is commonly co-doped as an effective sensitizer due to its large absorption cross-section in the 900-1100 nm range, corresponding to the $^2F_{5/2} \rightarrow ^2F_{7/2}$ transition.²⁷ Typical doping concentrations range from 18-25% for Yb^{3+} and 0.3-2% for Tm^{3+} and Er^{3+} to achieve optimal emission intensity.²⁸

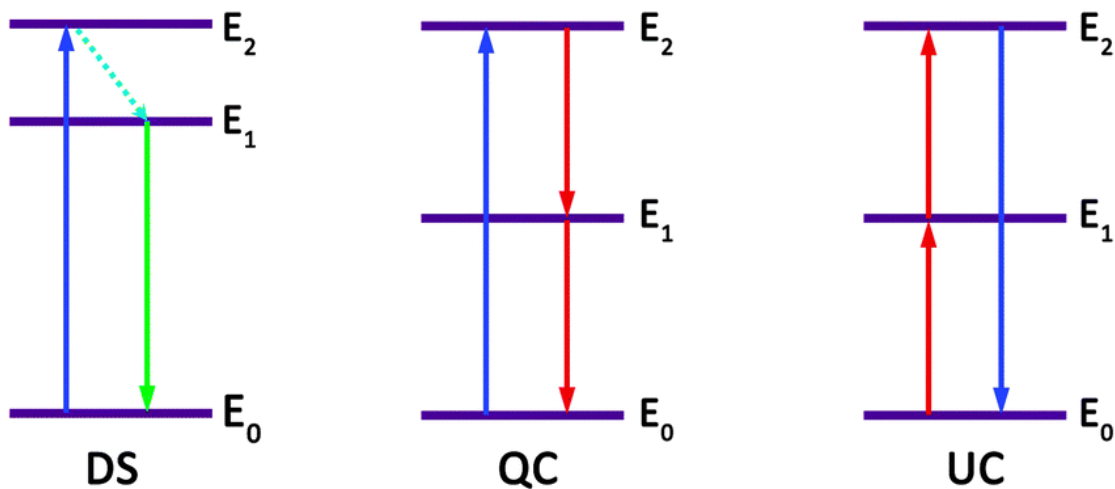


Figure 1.9 Schematic illustrating three energy transfer modes of Ln^{3+} . From left to right, these are downshifting (DS), quantum cutting (QC), and upconversion (UC). Upward and downward full arrows stand for photon excitation and emission processes, respectively. The dashed line represents a non-radiative relaxation process.⁹

1.4 Periodic Mesoporous Organosilicas (PMOs): Structure, Luminescence, and Functionalization

Periodic mesoporous organosilicas (PMOs) represent a novel category of materials characterized by their regularly arranged mesopores, ranging from 1.5 to 30 nm in diameter, and nanometric pore walls composed of organosilica. In this structure, each organic moiety is covalently bonded to multiple silicon atoms, ensuring a uniform distribution of these bridging organic groups both within and on the surface of the pore walls. The initial synthesis of PMOs was independently achieved by three groups in 1999, marking a significant milestone in the field.²⁹⁻³¹ Since then, PMOs with diverse organic bridging groups and varying pore sizes and geometries have been synthesized and characterized. The evolving research in PMOs now extends beyond synthesis and structural analysis to explore their functional applications across scientific and engineering disciplines, including biology and medicine. This transition underscores the interdisciplinary potential of PMOs and their role as a hallmark of nanotechnology.³²

1.4.1 Structural Characteristics of PMOs

Mesoporous Design: In 1999, three distinct research teams independently achieved the synthesis of mesoporous organosilica hybrids using dipodal alkoxy silane precursors with the general formula $((R'O)_3Si-R-Si(OR')_3)$; where R represents an organic bridging group and R' is either methyl or ethyl.²⁹⁻³¹ These novel mesoporous hybrids, derived from bridged organosilane precursors $(R[Si(OR')_3]_n)$; with $n \geq 2$, have been categorized as periodic mesoporous organosilicas (PMOs). The synthesis of PMO hybrids was conceptualized by adapting the methodology used in surfactant-directed synthesis of ordered mesoporous silica,

this approach was notably inspired by successful research on organosilsesquioxane gels (Figure 1.10).

The defining feature of PMOs is their well-defined mesopores, whose diameters can be precisely controlled within the range of 1.5–30 nm. This control is achieved through the strategic selection of template surfactants and additives during the polycondensation process. While ionic surfactant templates have traditionally been favored for synthesizing conventional PMOs, the use of amphiphilic block copolymer templates, along with the incorporation of salts, has facilitated the successful creation of large-pore PMOs. These PMOs exhibit varying symmetries in their mesostructures, expanding the potential applications and functionalities of these materials.³³

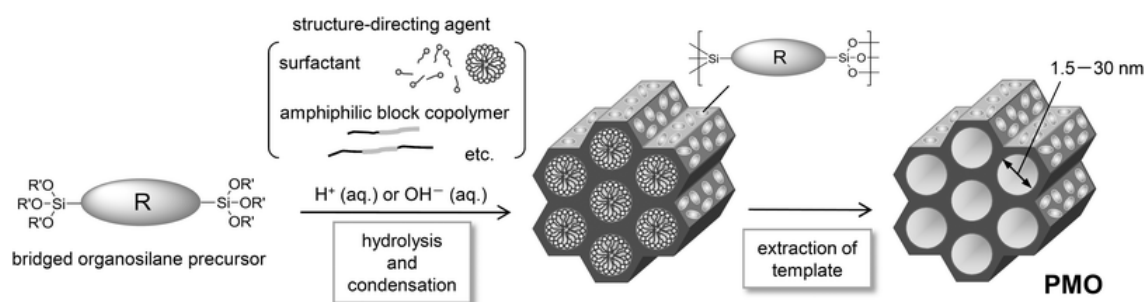
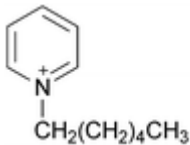
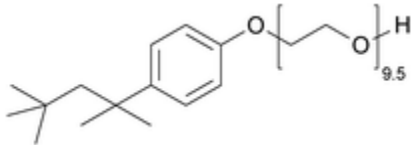
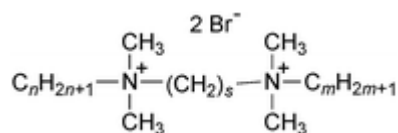


Figure 1.10 Synthesis of periodic mesoporous organosilica (PMO) from organic-bridged alkoxy silane precursors.³³

A diverse range of surfactants can serve as templates for the synthesis of mesoporous materials. Table 1.2 summarizes the most commonly employed surfactants, along with their chemical structures. These surfactants can be broadly categorized into two classes: ionic and nonionic.

Table 1.2 List of frequently used surfactants in PMO synthesis.³⁴

CTAC/CTAB	Cetyltrimethylammonium chloride/bromide	$\begin{array}{c} \text{CH}_3 \\ \\ \text{H}_3\text{C}-\text{N}^+-\text{(CH}_2\text{)}_{15}\text{CH}_3 \\ \\ \text{CH}_3 \end{array}$	$\text{Cl}^- / \text{Br}^-$
OTAC	Octadecyltrimethylammonium chloride	$\begin{array}{c} \text{CH}_3 \\ \\ \text{H}_3\text{C}-\text{N}^+-\text{(CH}_2\text{)}_{17}\text{CH}_3 \\ \\ \text{CH}_3 \end{array}$	Cl^-
$\text{C}_n\text{TMACl/Br}$	Alkyltrimethylammonium chloride/bromide	$\begin{array}{c} \text{CH}_3 \\ \\ \text{H}_3\text{C}-\text{N}^+-\text{(CH}_2\text{)}_{n-1}\text{CH}_3 \\ \\ \text{CH}_3 \end{array}$	$\text{Cl}^- / \text{Br}^-$ $(n = 8, 10, 12, 14, 16, 18)$
CPCI	Cetylpyridinium chloride		Cl^-
FC4	Fluorocarbon surfactant	$\text{C}_3\text{F}_7\text{O}(\text{CF}_2\text{CF}_2\text{O})_2\text{CF}_2\text{CONH}(\text{CH}_2)_3-\text{N}^+(\text{C}_2\text{H}_5)_3$	I^-
Brij-30	Polyoxyethylene (4) lauryl ether	$\text{HO} \left[\text{CH}_2\text{CH}_2\text{O} \right]_4 \text{CH}_2(\text{CH}_2)_{10}\text{CH}_3$	
Brij-56	Polyoxyethylene (10) cetyl ether	$\text{HO} \left[\text{CH}_2\text{CH}_2\text{O} \right]_{10} \text{CH}_2(\text{CH}_2)_{14}\text{CH}_3$	
Brij-76	Polyoxyethylene (10) stearyl ether	$\text{HO} \left[\text{CH}_2\text{CH}_2\text{O} \right]_{10} \text{CH}_2(\text{CH}_2)_{16}\text{CH}_3$	
Triton-X100	Polyoxyethylene (10) octylphenyl ether		
P123	Pluronic P123 poly(ethylene glycol)–poly(propylene glycol)–poly(ethylene glycol)	$\text{HO} \left[\text{CH}_2\text{CH}_2\text{O} \right]_{20} \left[\text{CH}_2\text{CH}(\text{CH}_3)\text{O} \right]_{70} \left[\text{CH}_2\text{CH}_2\text{O} \right]_{20} \text{H}$	
F127	Pluronic F127 poly(ethylene glycol)–poly(propylene glycol)–poly(ethylene glycol)	$\text{HO} \left[\text{CH}_2\text{CH}_2\text{O} \right]_{100} \left[\text{CH}_2\text{CH}(\text{CH}_3)\text{O} \right]_{65} \left[\text{CH}_2\text{CH}_2\text{O} \right]_{100} \text{H}$	
B50-6600	Poly(ethylene oxide)–poly(butylene oxide)–poly(ethylene oxide)	$\text{HO} \left[\text{CH}_2\text{CH}_2\text{O} \right]_{39} \left[\text{CH}_2\text{CH}_2\text{CH}_2\text{CH}_2\text{O} \right]_{47} \left[\text{CH}_2\text{CH}_2\text{O} \right]_{39} \text{H}$	
PEO–PLGA–PEO	Poly(ethylene oxide)–poly(lactic acid-co-glycolic acid)–poly(ethylene oxide)	$\text{HO} \left[\text{CH}_2\text{CH}_2\text{O} \right]_x \left[\text{O} \left(\text{C}(=\text{O})\text{CH}(\text{CH}_3) \right)_y \left(\text{C}(=\text{O})\text{CH}_2 \right)_z \right]_x \text{H}$	



Organosilica Framework: A key advantage of PMOs lies in their extensive library of potential organic moieties (R), allowing for precise structural control and functionalization.^{35, 36} Since their initial discovery, the range of organic bridging groups applicable to PMO synthesis has expanded significantly. Early research primarily focused on simple organic bridges like ethylene, ethenylene, phenylene, and thiophene.^{29-31, 37} However, recent advancements in the synthesis of organosilane precursors have opened doors to incorporating various organic groups into PMO frameworks, including hydrocarbons, heteroaromatics, and even metal complexes.^{35, 36} Furthermore, the hydrolysis and condensation of allylorganosilane compounds ($\text{R}[\text{Si}(\text{CH}_2\text{CH}=\text{CH}_2)_m(\text{OR}')_{3-m}]_n$; $m=2, 3$) represents an alternative route for PMO synthesis.³⁸ The superior stability of allylsilanes compared to alkoxysilanes under conventional organic synthesis conditions allows for the development of novel molecular building blocks with reactive groups, paving the way for the creation of even more intricate PMO structures.³⁹

1.4.2 Synthesis of PMO hybrids

PMO synthesis from 100% organic-bridged precursors Surfactant-directed

The initial exploration of periodic mesoporous organosilica (PMO) materials involved surfactant-directed polycondensation of single-component organosilane precursors. This approach yielded PMOs with homogeneously distributed organic bridges, primarily consisting of small aliphatic and aromatic groups within the pore walls.^{29-31, 37, 40} Research efforts subsequently shifted towards introducing more functional bridge units like biphenyl, divinylbenzene, and acridone.⁴¹⁻⁴⁴ Concurrently, researchers achieved precise control over the meso-scale symmetry of these

channels, ranging from lamellar and 2D hexagonal to 3D cage-like structures, by manipulating the synthesis conditions and utilizing different structure-directing agents.^{29, 35, 36, 45-48} The development of multi-component and multi-functional PMOs was achieved through co-condensation of two or more bridged organosilane precursors, as comprehensively detailed in previous reviews.^{35, 36} Utilizing a mixture of functionalized bridged organosilanes offers advantages in tailoring the meso-scale periodicity and framework properties. This includes controlling the density of functional moieties and adjusting the hydrophilic/hydrophobic balance. Later, researchers have successfully designed multi-functional PMOs incorporating heteroatom-containing organic bridges, leading to tailored surface and framework properties of the pore walls.⁴⁹⁻⁵¹

PMO synthesis by co-condensation

Co-condensation of functionalized bridged organosilanes with scaffold silica sources like tetraethylorthosilicate (TEOS) or ethylene-bridged precursors has emerged as a powerful technique for synthesizing mesoporous materials with specific functionalities. Beyond co-condensation, post-synthesis grafting and direct co-condensation with monosilylated functional precursors offer additional avenues for chemical modification of periodic mesoporous organosilica (PMO) frameworks.

An advancement utilizes dynamic covalent chemistry to incorporate imine, amine, and aldehyde functionalities into PMOs. This approach involves in situ formation of imine-containing bridging groups during the self-assembly process, employing organosilane precursors with reactive amine or aldehyde moieties.⁵² These diverse synthetic strategies have yielded PMOs with a wide range of functionalities, paving the way for potential applications in various fields, as comprehensively reviewed elsewhere.^{35, 36}

Researchers have achieved the co-existence of contrasting functionalities within the same material. Through the strategic design of monosilylated and bridged organosilane compounds, simultaneous incorporation of acidic frameworks with basic pore surfaces has been realized.⁵³ This approach involves co-condensation of N-protected aminopropyltrimethoxysilane and trimethoxysilyl-terminated 4,5-dithiooctane, followed by a series of post-synthesis modifications. Such materials, containing both acidic and basic functionalities, hold promise as novel catalysts for multistep reactions, as demonstrated by a report on the two-step conversion of benzaldehyde dimethyl acetal to 2-nitrovinyl benzene.⁵⁴

Moreover, covalently bonded organic anions and cations have been successfully incorporated into PMO frameworks using trisilylated guanidinium sulfonimide ionic liquids.⁵⁵ The presence and accessibility of these ion-pairs on the pore surface were confirmed through solvatochromic experiments with Reichardt's dye. The potential of immobilizing ionic liquid analogues onto PMOs extends beyond catalysis, offering exciting possibilities for the development of novel and sustainable processes.

1.4.3 Luminescent PMOs

Incorporating functional groups, such as chromophores, into the periodic mesoporous organosilica (PMO) framework presents a significant advantage. Chromophores are specific groups of atoms within a molecule that can absorb light, leading to either the emission of light (luminescence) or the manifestation of color through selective absorption and reflection. This incorporation allows for the spatial separation of these groups between the framework and the mesochannels. This arrangement facilitates energy transfer from donor groups in the framework to acceptor groups in the mesochannels, potentially enhancing desired optical properties such as luminescence. Such a configuration is particularly beneficial for

optical sensors, where target molecules or ions can diffuse more efficiently through PMOs compared to chromophore-attached mesoporous silicas. This efficiency is attributed to the reduced steric hindrance in the mesochannels of PMOs, leading to a quicker sensing response. Furthermore, the dense packing of chromophores within the PMO framework augments light absorption, thereby increasing luminescence intensity. Therefore, synthesizing PMOs with integrated chromophores and understanding their optical properties are of considerable interest.⁵⁶

This section highlights recent advancements in two key approaches for the synthesis of luminescent PMO materials (Figure 1.11). The first approach involves co-condensation of chromophores equipped with alkoxysilyl groups alongside a significant amount of a framework precursor (chromophores in framework). However, a key challenge lies in identifying chromophores with suitable alkoxysilyl groups that can efficiently integrate into the PMO framework without compromising luminescence properties. Current research focuses on developing new chromophores with compatible functionalities.

The second method relies on luminescent PMOs prepared by Lanthanides Grafting or Incorporation (chromophores in mesopores). Additionally, it explores innovative material design strategies for achieving highly efficient visible-light luminescent PMOs. However, controlling the distribution and accessibility of these grafted species within the pores remains a challenge. Optimizing grafting techniques and understanding the interaction between lanthanides and the pore surface are ongoing areas of research.

Beyond the structural differences, it's important to consider the relative merits and challenges of each approach for different applications. PMOs synthesized via co-condensation are often favored for applications where uniform distribution and

precise control over the luminescent centers are crucial. On the other hand, PMOs prepared by lanthanide grafting/incorporation offer exciting possibilities for applications requiring tunable emission properties or high luminescence intensity. This approach might be advantageous for upconversion materials or luminescent bioimaging probes.

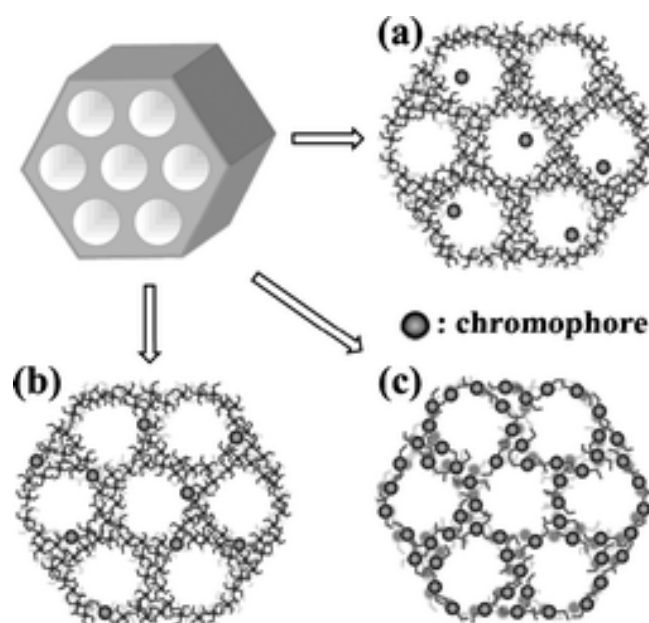


Figure 1.11 Types of luminescent periodic mesoporous silicas and organosilicas. (a) Chromophore-doped silica (chromophores in mesopores). (b) PMO prepared by co-condensation (chromophores in framework). (c) PMO synthesized from 100% chromophore precursors (chromophores in framework).⁵⁶

Luminescent PMOs synthesized from chromophore precursors

A significant challenge in synthesizing luminescent periodic mesoporous organosilica (PMO) materials lies in overcoming the phenomenon of solid-state quenching. This effect describes the decrease in luminescence intensity (quantum yield) observed in organic molecules upon transitioning from a liquid to a solid state. This quenching is attributed to strong intermolecular interactions in the excited state of the molecules when packed closely together in a solid matrix. Due to the potential impact of solid-state quenching, research focusing on synthesizing PMOs exclusively from chromophore-based precursors has been relatively limited. In contrast, the co-condensation method, which utilizes a combination of

chromophore and framework precursors, has been more extensively explored due to its ability to mitigate quenching effects. This section delves into strategies to address solid-state quenching and recent advancements in synthesizing highly luminescent PMOs solely from chromophore precursors.⁵⁶

Recent years have witnessed significant progress in the development of luminescent periodic mesoporous organosilica (PMO) materials, driven by advancements in both material design and synthesis techniques. This progress builds upon the initial groundwork laid by Inagaki et al. in 2002, who reported the synthesis of potentially fluorescent PMOs, including a benzene-silica PMO with hexagonal mesopores and a biphenylene-bridged PMO.^{40, 41} These early examples were characterized by well-defined mesostructures and high surface areas, demonstrating successful synthesis protocols and the promise of ordered structures.

Subsequent research by Ozin et al. and others expanded the variety of chromophore groups in PMO pore walls, exploring materials like phenylene-bridged silsesquioxane and biphenyl PMOs.^{42, 43, 57, 58} These studies not only enhanced the understanding of PMO structures but also opened avenues for potential optical sensor applications. For instance, Bhaumik et al. reported a diimine-incorporated PMO, showcasing its utility as a tunable chemosensor and photoluminescent material.⁵⁹

By 2007-2009, the research focus shifted towards PMOs built from aromatic groups for light-harvesting and optoelectronic applications. Leyva et al. and Ha et al. reported on electroluminescent PMOs, contributing to the development of OLEDs.^{60, 61} Simultaneously, systematic studies by Fröba et al. extended the organic conjugated π -system of these materials, exploring new possibilities for colored mesoporous materials.⁶²

The subsequent years saw further innovations, such as the integration of photoluminescent perylene-bridged silsesquioxane in PMOs by He et al.,⁶³ and Inagaki et al.'s work on PMOs with various aromatic bridges, highlighting their fluorescence properties and potential in light-emitting applications.⁶⁴⁻⁶⁷

Recent advancements also include PMOs grafted with metal ions and the exploration of PMOs as fluorescent chemosensors, as evidenced by the work of Inagaki et al. and others.⁶⁸⁻⁷² These developments demonstrate the versatility of PMOs and their growing importance in nanomedicine and optoelectronics. The research trajectory underscores the potential of PMOs in diverse applications, from ion sensing to theranostics, driven by continuous innovation in material synthesis and functionalization (Figure 1.12).⁷³⁻⁷⁶

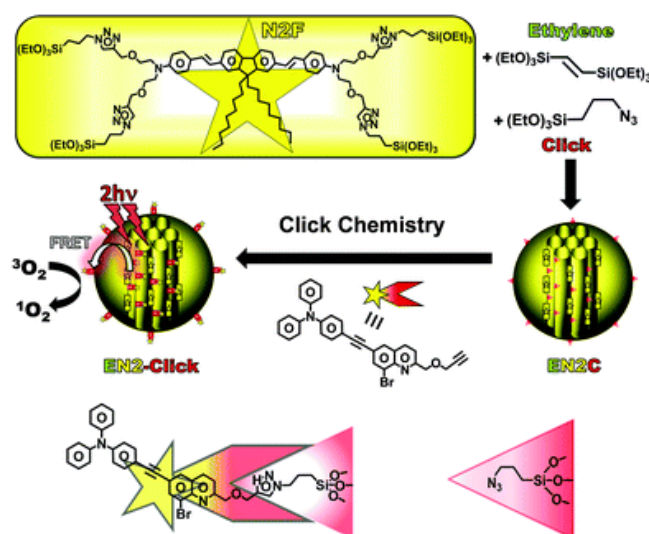


Figure 1.12 Representation of the design of luminescent PMOs synthesized from chromophore precursors.⁷³

Luminescent PMOs prepared by Lanthanides Grafting or Incorporation

The development of lanthanides grafted or incorporated into PMOs has been marked by significant advancements and diverse synthesis strategies. In 2008, Yang et al. introduced a new PMO material covalently grafted with 1,10-phenanthroline, showcasing a well-ordered hexagonal structure and enhanced luminescence upon

europium grafting.⁷⁷ This approach set a precedent for subsequent research focusing on enhancing luminescent properties through lanthanide grafting (Figure 1.13).

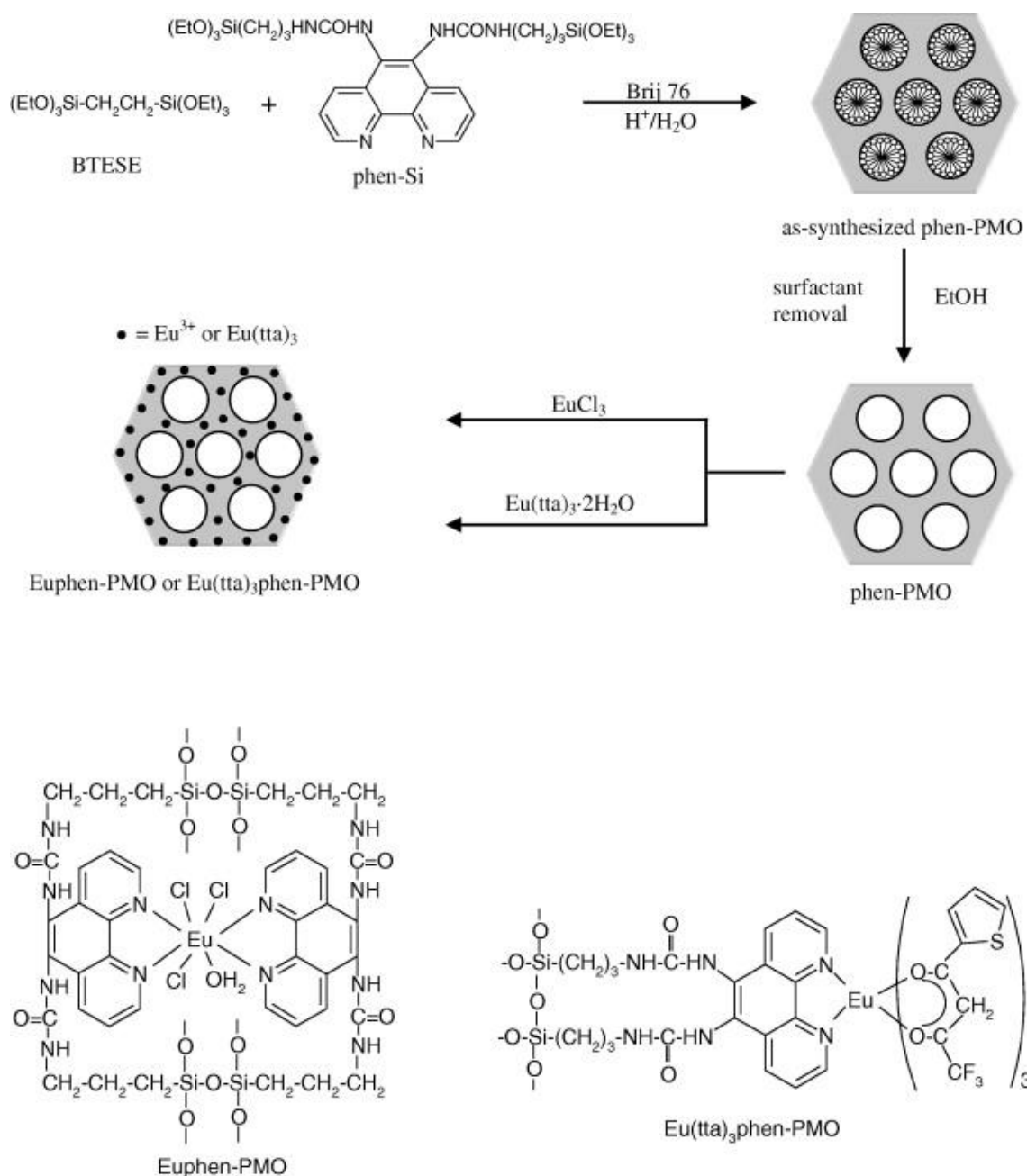


Figure 1.13 Schematic diagram of incorporation of europium complex into the framework of PMO via a co-condensation of 1,2-bis(triethoxysilyl)ethane (BTESE) and 5,6-bis(N-(3-(triethoxysilyl)propyl)-1,10-phenanthroline(phen-Si)) using covalent bond.⁷⁷

Further developments included Dang et al.'s synthesis of a PMO using benzoic acid-functionalized organosilane, post-functionalized with $TbCl_3$, retaining its

mesostructure and exhibiting characteristic Tb^{3+} emission peaks.⁷⁸ Similarly, Li et al. presented sulfide functionalized Eu/Tb PMO hybrids, maintaining their ordered mesoporous structure post-lanthanide grafting and showing visible emission.⁷⁹

A notable contribution by Yan et al. in 2010 involved covalently bonding luminescent lanthanide hybrids to a PMO using a calix[4]arene derivative, achieving efficient luminescence, especially in the Tb^{3+} grafted material.⁸⁰ This trend continued with the synthesis of near-infrared emitting lanthanide PMOs by Zhang et al. in 2012, indicating the versatility of these materials for various luminescent applications.⁸¹

The research further expanded into exploring the potential of these PMOs in ion sensing and solvent sensing, as demonstrated by Van Der Voort et al. and the group of Yu, showing selective luminescent sensing of ions like Cu^{2+} in aqueous solutions.⁸²⁻⁸⁷ In addition, a novel "ship-in-a-bottle" approach has been proposed for creating hollow periodic mesoporous organosilicas (PMOs) that encapsulate lanthanide nanoparticles within their structure. This innovative method represents a significant departure from traditional synthesis techniques, offering a unique way to integrate lanthanide nanoparticles directly into the hollow cavities of PMOs (Figure 1.14).⁸⁸

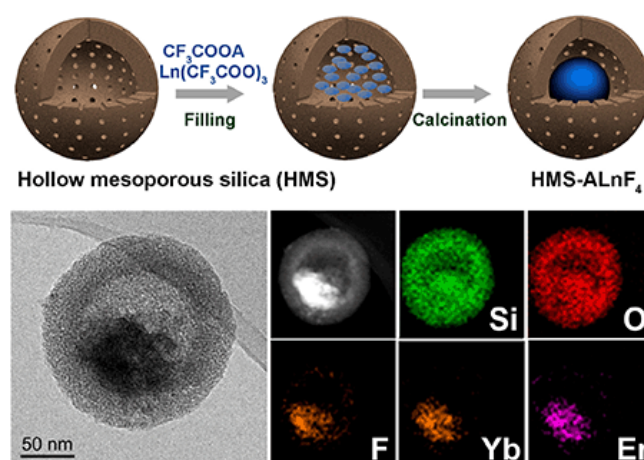


Figure 1.14 Schematic illustration of the "ship-in-a-bottle" approach for the synthesis of UC nanorattles based on lanthanide-doped fluorides.⁸⁸

Kaczmarek et al. developed an ePMO material functionalized with dipyridyl-pyridazine units and grafted with NIR-emitting lanthanide ions (Nd^{3+} , Er^{3+} , Yb^{3+}).⁸⁹ This ePMO, created via a hetero Diels-Alder reaction, was compared with a similar vinyl-silica material. Despite the ease of preparing the vinyl-silica variant, the ePMO demonstrated superior stability. These materials, particularly the Yb^{3+} variant, showed promise as ratiometric thermometers in the 110–310 K range. In a later study, a PMO composed of N,N-bis(trimethoxysilylpropyl)-2,6-pyridine dicarboxamide and TEOS was used to create Tb/Eu and Tb/Sm grafted materials, which exhibited strong visible luminescence and were tested as biological nanothermometers, showing effective temperature sensing in the 260–460 K range.⁹⁰ These findings highlight the potential of nano-PMOs in applications like optical thermometers and biological nanothermometers, due to their nano-size, strong luminescence, and biocompatibility.

This versatility in applications, coupled with the advancements in synthesis techniques, underscores the significant progress in the field of lanthanides grafted or incorporated into PMOs.

1.5 Luminescent PMOs in Sensing Applications

1.5.1 PMOs as sensors

Luminescent periodic mesoporous organosilicas (PMOs) have emerged as a groundbreaking class of materials in the field of sensing, owing to their unique combination of structural features and luminescent properties. This section delves into the application of luminescent PMOs in sensing, exploring how their specific characteristics contribute to advancements in this area.

Luminescence-Based Sensing Mechanism: The fundamental principle behind using luminescent PMOs in sensing revolves around the changes in their luminescent properties upon interaction with target analytes. These changes can be

in the form of altered luminescent intensity, wavelength shift, or decay time, providing a measurable response to the presence of specific substances.^{91, 92}

Selectivity and Sensitivity: The luminescent properties of PMOs can be finely tuned to respond to specific stimuli, such as changes in pH, temperature, or the presence of certain ions or molecules. This sensitivity, coupled with the ability to tailor the material's specificity through surface functionalization, makes luminescent PMOs highly effective for precise detection in complex environments (Figure 1.15).⁹³

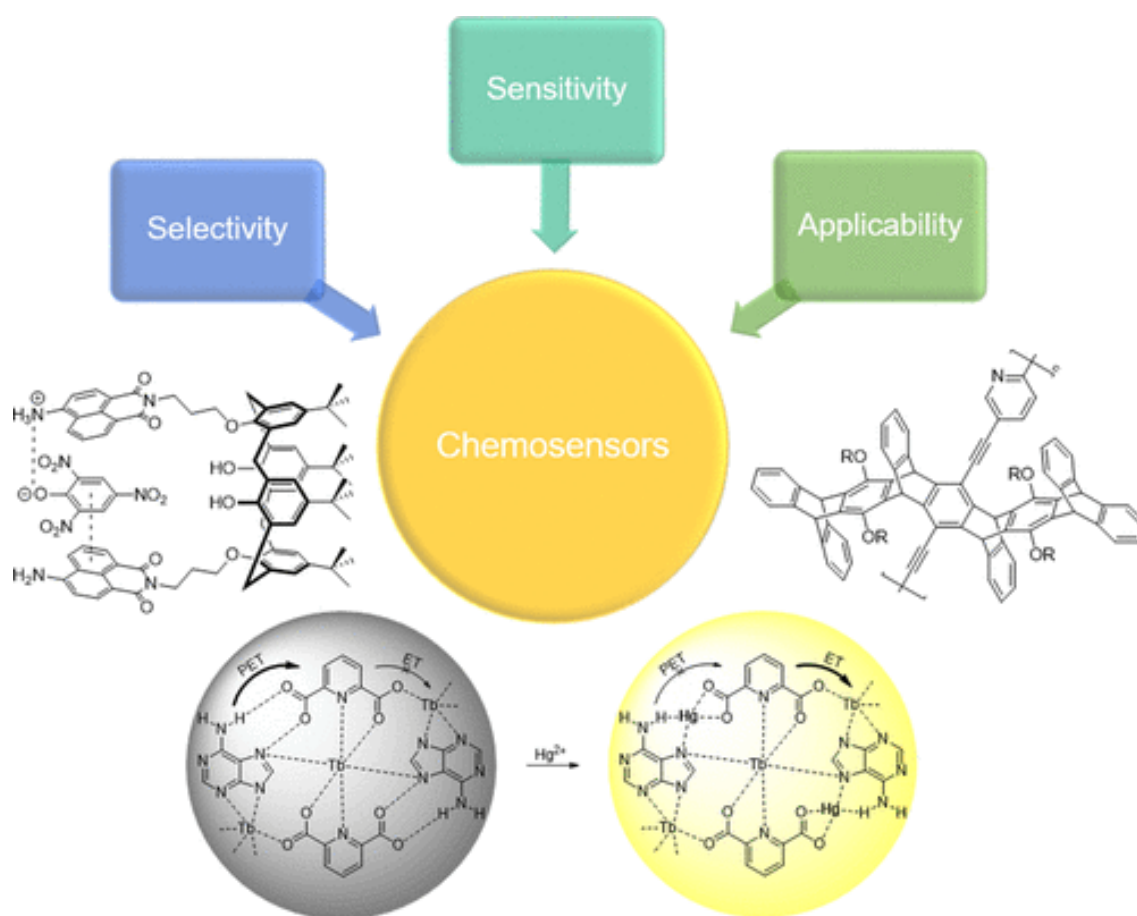


Figure 1.15 Examples of recently developed chemosensors that have all three aspects of an ideal chemosensor: selectivity, sensitivity, and applicability.⁹³

Tailoring Luminescent Properties: The design and synthesis of luminescent PMOs for sensing applications involve tailoring their luminescent properties to respond specifically to target analytes. This is achieved through the strategic selection and incorporation of luminescent centers and functional groups during the

synthesis or post-synthesis modification processes. The choice of luminescent centers incorporated into PMOs is crucial for thermometric applications. Materials such as rare-earth ions or specific organic fluorophores, known for their temperature-sensitive luminescent properties, are often selected.⁹⁰

Tailoring PMO Properties: The introduction of functional groups that can specifically bind or react with target analytes is a critical aspect of designing PMOs for sensing applications. These groups can significantly enhance the selectivity and sensitivity of the PMOs towards particular molecules or ions. The design of PMOs for thermometry involves tailoring their properties, such as pore size and framework composition, to optimize thermal responsiveness. This customization is key to achieving high accuracy and sensitivity in temperature measurement.

1.5.2 Metal ion sensors

Luminescent detection of metal ions has garnered significant attention due to its advantages, such as rapid detection, high sensitivity, selectivity, affordability, and operational simplicity. This technique utilizes changes in luminescence intensity to identify specific ions, offering high selectivity through carefully designed sensors. PMO materials hold immense promise for metal ion detection due to the tunability of their functional organic groups. These groups, often containing electron-rich donor atoms like nitrogen (N), oxygen (O), phosphorus (P), and sulfur (S), play a crucial role in achieving selective ion detection. The underlying mechanisms involve metal-ligand coordination, where the metal ions weakly bind to heteroatoms within the PMO framework, and intramolecular energy transfer from the organic groups to the metal ions. These mechanisms provide a versatile platform for developing highly selective and sensitive luminescent PMO sensors for various metal ion detection applications.

Early Examples:

Pioneering work by Inagaki et al. demonstrated the feasibility of PMOs for metal ion detection. Their covalent attachment of a fluorescent bipyridine receptor onto a biphenyl-bridged PMO exhibited selective quenching upon exposure to Cu^{2+} ions, paving the way for further exploration.⁹⁴

Ozin et al. successfully incorporated photoluminescent silica nanoparticles into a PMO framework, opening avenues for multifunctional optoelectronic and biomedical applications.⁹⁵

Yang et al. reported a 1,10-phenanthroline functionalized PMO exhibiting selective fluorescence quenching in response to Cu^{2+} ions, highlighting the potential of PMOs for sensitive detection.⁹⁶

Expanding the Scope:

Ha et al. utilized a PMO containing ethidium bromide moieties for selective detection of Hg^{2+} and Fe^{3+} ions in water and living cells.⁹⁷

Haw et al. synthesized a nano-sized bis-benzimidazole PMO material exhibiting ratiometric fluorescence response for Cu^{2+} ion detection.⁷⁵

Inagaki et al. reported a PMO with pyridine and benzene moieties, demonstrating selective adsorption of Cu^{2+} ions based on the pyridine content.⁷⁶

Yu et al. developed a luminescent hybrid material by linking Eu(III) complexes to a L-COOH-functionalized PMO, demonstrating the potential for lanthanide-based sensors with Cu^{2+} ion selectivity.⁸⁷

Kaczmarek et al. reported nano-sized PMOs grafted with Eu^{3+} , Tb^{3+} , or their mixture, further functionalized with co-ligands like 1,10-phenanthroline. These materials exhibited selective "turn on" fluorescence for Pb^{2+} , Cr^{3+} , and Hg^{2+} ions.⁸⁵

Lanthanide-based PMO nanomaterials obtained by post-grafting with Eu(III) complexes onto amine-functionalized PMOs hold promise for Hg^{2+} ion detection.⁸⁶

1.5.3 Temperature sensors

Non-invasive temperature measurement holds immense potential in the medical field, offering remote monitoring capabilities. Luminescent lanthanide-based periodic mesoporous organosilica (PMO) materials are particularly promising for this application due to their temperature-dependent luminescence properties. These changes manifest in various forms, including integrated emission intensity, lifetime, spectral shift, and bandwidth of specific transitions.

Ratiometric Temperature Sensing:

Among various techniques, this section focuses on ratiometric temperature sensing, which analyzes the relative intensity change between two closely spaced energy transitions. Using the ratio of the intensity two emission bands as a parameter has the distinct advantage of being independent of both the excitation light intensity and the detector sensitivity. These emissions can originate from either a single or distinct emitting centers within the lanthanide PMO. Additionally, these materials can be excited through various mechanisms, including the antenna effect, direct excitation, and upconversion, making them versatile for diverse excitation and emission sources.

Lanthanide PMOs offer several advantages:

Broad operational temperature range: They can be employed across cryogenic (up to 100 K), medium (100-300 K), physiological (298-323 K), and high temperature ranges (≥ 450 K).

Tunable sensitivity: The sensitivity can be adjusted by incorporating different lanthanide ions and varying their ratios within the PMO framework.

Biocompatibility: Studies suggest minimal to no toxicity towards human cells, making them suitable for potential biomedical applications.

Stability in aqueous environments: They form stable colloidal suspensions in water, maintaining their thermometric properties.

Examples:

Kaczmarek et al. synthesized PMO nanoparticles doped with different ratios of Tb^{3+}/Eu^{3+} and Tb^{3+}/Sm^{3+} ions, exhibiting temperature-dependent luminescence in the range of 260-460 K with varying sensitivities.⁹⁰

They further developed Dy-Dy and Tb-Sm based PMOs, demonstrating operation in different temperature ranges with good sensitivity (Figure 1.16).⁹⁸

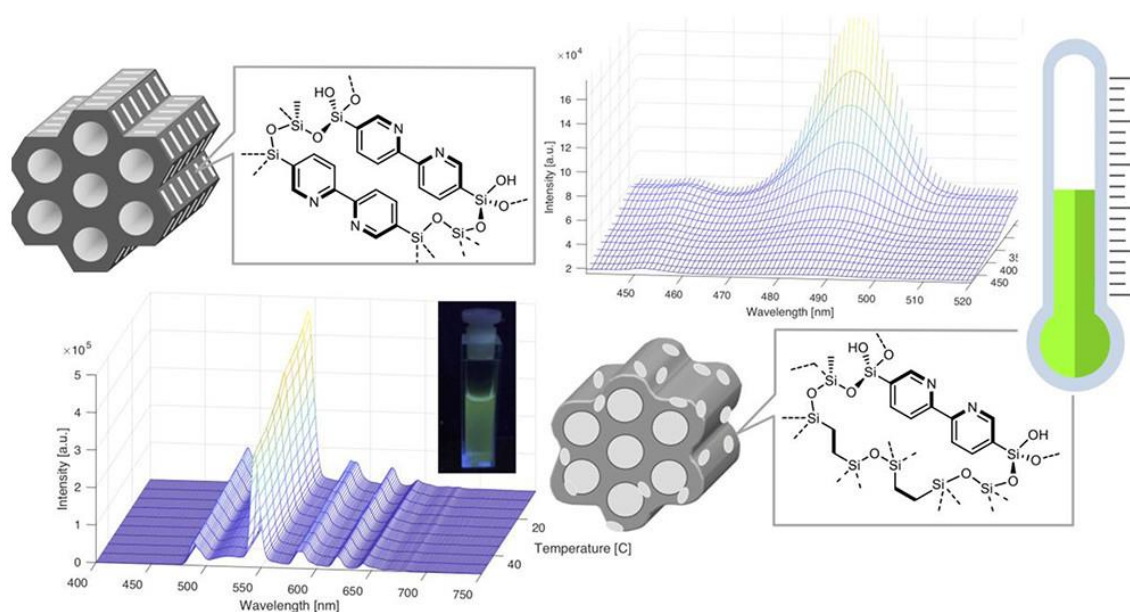


Figure 1.16 Schematic Illustration of Lanthanide-Grafted Bipyridine periodic mesoporous organosilicas (BPy-PMOs) for Physiological Range and Wide Temperature Range Luminescence Thermometry.⁹⁸

These studies highlight the potential of lanthanide PMOs as promising candidates for non-invasive temperature sensing in biomedical applications.

1.6 Aims of This Thesis

The primary goal of this thesis is to explore and advance the understanding of luminescent periodic mesoporous organosilicas (LPMOs) and their applications in the fields of sensing and thermometry. The specific aims are:

1. To investigate the luminescent properties of PMOs: This involves a comprehensive study of the luminescent characteristics of PMOs, focusing on their synthesis, functionalization, and the mechanisms underlying their luminescence.

2. To develop advanced PMO-based sensors: A key objective is to utilize the unique properties of LPMOs to create highly sensitive and selective sensors. This includes exploring various functionalization strategies to enhance the sensitivity and selectivity of PMOs for specific analytes.

3. To explore PMOs in thermometric applications: Although a secondary focus, this thesis aims to investigate the potential of LPMOs in temperature measurement and monitoring, assessing their efficacy and advantages over traditional thermometric materials.

4. To conduct comparative studies: This involves comparing the performance of LPMOs with other luminescent materials, such as MOFs, COFs, inorganic phosphors, and quantum dots, particularly in sensing applications.

5. To address current challenges and identify future directions: Identifying and tackling the existing challenges in the field of luminescent PMOs, such as stability and sensitivity, and forecasting future research directions, are also critical aims of this thesis.

This thesis aims to contribute to the field of material science, particularly in the study and application of luminescent PMOs, and to open new pathways for research and applications in environmental monitoring, healthcare, and technology.

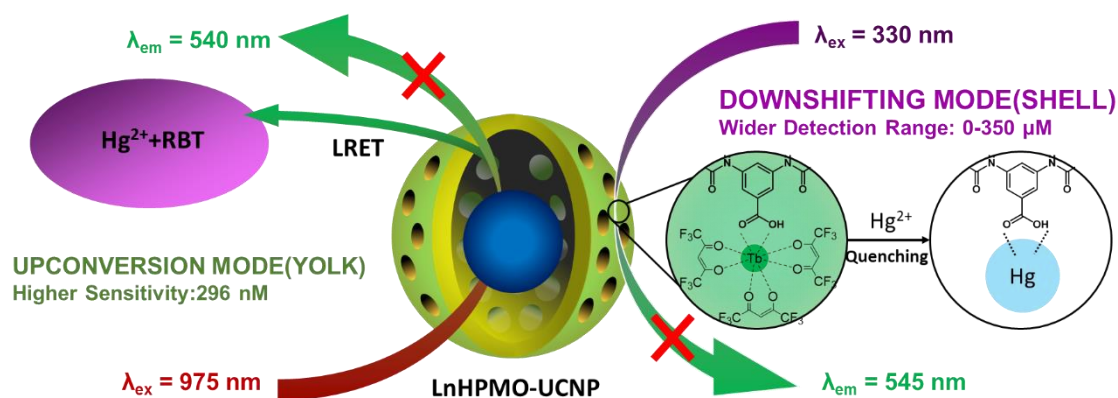
1.7 Reference

1. B. Valeur and M. N. Berberan-Santos, *J Chem Educ*, 2011, **88**, 731-738.
2. D. Vij, *Luminescence of solids*, Springer Science & Business Media, 2012.
3. V. Gribkovskii, in *Luminescence of Solids*, Springer, 1998, pp. 1-43.
4. S. W. McKeever, *Thermoluminescence of solids*, Cambridge University Press, 1985.
5. C. R. Ronda, *Luminescence: from theory to applications*, John Wiley & Sons, 2007.
6. N. T. Kalyani, H. C. Swart and S. J. Dhoble, *Principles and applications of organic light emitting diodes (OLEDs)*, Woodhead Publishing, 2017.
7. P. Goel, R. Mittal, N. Choudhury and S. Chaplot, *J. Phys. Condens. Matter*, 2010, **22**, 065401.
8. S. Cotton, *Lanthanide and actinide chemistry*, John Wiley & Sons, 2024.
9. H. Dong, L. D. Sun and C. H. Yan, *Chem Soc Rev*, 2015, **44**, 1608-1634.
10. R. E. Blankenship, *Molecular mechanisms of photosynthesis*, John Wiley & Sons, 2021.
11. B. Alpha, V. Balzani, J. M. Lehn, S. Perathoner and N. Sabbatini, *Angew. Chem. Int. Ed.*, 1987, **26**, 1266-1267.
12. R. Ziessel, N. Sabbatini, M. Guardigli, F. Bolletta and I. Manet, *New J Chem*, 1993, **17**, 323-324.
13. G. De Sa, O. Malta, C. de Mello Donegá, A. Simas, R. Longo, P. Santa-Cruz and E. da Silva Jr, *Coord Chem Rev*, 2000, **196**, 165-195.
14. S. Tobita, M. Arakawa and I. Tanaka, *J. Phys. Chem.*, 1984, **88**, 2697-2702.
15. J. Zimmermann, A. Zeug and B. Röder, *Phys. Chem. Chem. Phys.*, 2003, **5**, 2964-2969.
16. S. Weissman, *J. Chem. Phys.*, 1942, **10**, 214-217.
17. G. A. Crosby, R. E. Whan and R. Alire, *J. Chem. Phys.*, 1961, **34**, 743-748.
18. M. V. Werts, M. Duin, J. Hofstraat and J. Verhoeven, *ChemComm*, 1999, 799-800.
19. C. Yang, L. M. Fu, Y. Wang, J. P. Zhang, W. T. Wong, X. C. Ai, Y. F. Qiao, B. S. Zou and L. L. Gui, *Angew. Chem. Int. Ed.*, 2004, **43**, 5010-5013.
20. Z. H. Hu, P. L. Hernández-Martínez, X. Liu, M. R. Amara, W. J. Zhao, K. Watanabe, T. Taniguchi, H. V. Demir and Q. H. Xiong, *Acs Nano*, 2020, **14**, 13470-13477.
21. S. W. Tabernig, B. Daiber, T. Y. Wang and B. Ehrler, *J. Photonics Energy*, 2018, **8**, 022008-022008.
22. D. Gupta, M. Katiyar and Deepak, *Opt. Mater.*, 2006, **28**, 295-301.
23. X. Y. Huang, S. Y. Han, W. Huang and X. G. Liu, *Chem. Soc. Rev.*, 2013, **42**, 173-201.
24. R. Yadav, S. K. Singh, R. K. Verma and S. B. Rai, *Chem. Phys. Lett.*, 2014, **599**, 122-126.
25. F. Auzel, *Chem Rev*, 2004, **104**, 139-173.
26. S. H. Jeong, Y. K. Kshetri, S. H. Kim, S. H. Cho and S. W. Lee, *Prog. Nat. Sci.*, 2019, **29**, 549-555.
27. M. Vega, I. R. Martin and J. Llanos, *J Alloy Compd*, 2019, **806**, 1146-1152.
28. X. Xu, C. Clarke, C. Ma, G. Casillas, M. Das, M. Guan, D. Liu, L. Wang, A. Tadich, Y. Du, C. Ton-That and D. Jin, *Nanoscale*, 2017, **9**, 7719-7726.
29. S. Inagaki, S. Guan, Y. Fukushima, T. Ohsuna and O. Terasaki, *J. Am. Chem. Soc.*, 1999, **121**, 9611-9614.
30. B. J. Melde, B. T. Holland, C. F. Blanford and A. Stein, *Chem. Mater.*, 1999, **11**, 3302-3308.
31. T. Asefa, M. J. MacLachlan, N. Coombs and G. A. Ozin, *Nature*, 1999, **402**, 867-871.
32. W. Wang, J. E. Lofgreen and G. A. Ozin, *Small*, 2010, **6**, 2634-2642.
33. N. Mizoshita, T. Tani and S. Inagaki, *Chem Soc Rev*, 2011, **40**, 789-800.
34. P. Van der Voort, D. Esquivel, E. De Canck, F. Goethals, I. Van Driessche and F. J. Romero-Salguero, *Chem Soc Rev*, 2013, **42**, 3913-3955.
35. F. Hoffmann, M. Cornelius, J. Morell and M. Fröba, *Angew. Chem. Int. Ed.*, 2006, **45**, 3216-3251.
36. S. Fujita and S. Inagaki, *Chem. Mater.*, 2008, **20**, 891-908.

37. M. MacLachlan and G. Ozin, *ChemComm*, 1999, 2539-2540.
38. M. P. Kapoor, S. Inagaki, S. Ikeda, K. Kakiuchi, M. Suda and T. Shimada, *J Am Chem Soc*, 2005, **127**, 8174-8178.
39. Y. Maegawa, T. Nagano, T. Yabuno, H. Nakagawa and T. Shimada, *Tetrahedron*, 2007, **63**, 11467-11474.
40. S. Inagaki, S. Guan, T. Ohsuna and O. Terasaki, *Nature*, 2002, **416**, 304-307.
41. M. P. Kapoor, Q. Yang and S. Inagaki, *J Am Chem Soc*, 2002, **124**, 15176-15177.
42. A. Sayari and W. H. Wang, *J. Am. Chem. Soc.*, 2005, **127**, 12194-12195.
43. M. Cornelius, F. Hoffmann and M. Fröba, *Chem. Mater.*, 2005, **17**, 6674-6678.
44. M. Waki, N. Mizoshita, T. Ohsuna, T. Tani and S. Inagaki, *ChemComm*, 2010, **46**, 8163-8165.
45. Y. Goto and S. Inagaki, *ChemComm*, 2002, DOI: 10.1039/b207825b, 2410-2411.
46. E.-B. Cho, D. Kim, J. Górká and M. Jaroniec, *J. Mater. Chem.*, 2009, **19**, 2076-2081.
47. W. Guo, I. Kim and C.-S. Ha, *ChemComm*, 2003, 2692-2693.
48. W. P. Guo, J. Y. Park, M. O. Oh, H. W. Jeong, W. J. Cho, I. Kim and C. S. Ha, *Chem. Mater.*, 2003, **15**, 2295-+.
49. J. Morell, M. Güngerich, G. Wolter, J. Jiao, M. Hunger, P. J. Klar and M. Fröba, *J. Mater. Chem.*, 2006, **16**, 2809-2818.
50. E. B. Cho, D. Kim and M. Jaroniec, *Langmuir*, 2007, **23**, 11844-11849.
51. E. B. Cho, D. Kim and M. Jaroniec, *Langmuir*, 2009, **25**, 13258-13263.
52. E. B. Cho, O. H. Han, S. Kim, D. Kim and M. Jaroniec, *Chem Commun*, 2010, **46**, 4568-4570.
53. J. Alauzun, A. Mehdi, C. Reye and R. J. Corriu, *J Am Chem Soc*, 2006, **128**, 8718-8719.
54. S. Shylesh, A. Wagener, A. Seifert, S. Ernst and W. R. Thiel, *Angew. Chem. Int. Ed.*, 2010, **49**, 184-187.
55. A. El Kadib, P. Hesemann, K. Molvinger, J. Brandner, C. Biolley, P. Gaveau, J. J. Moreau and D. Brunel, *J Am Chem Soc*, 2009, **131**, 2882-2892.
56. T. Tani, N. Mizoshita and S. Inagaki, *J. Mater. Chem.*, 2009, **19**, 4451-4456.
57. W. J. Hunks and G. A. Ozin, *Chem. Mater.*, 2004, **16**, 5465-5472.
58. J. Morell, G. Wolter and M. Fröba, *Chem. Mater.*, 2005, **17**, 804-808.
59. D. Chandra, T. Yokoi, T. Tatsumi and A. Bhaumik, *Chem. Mater.*, 2007, **19**, 5347-5354.
60. M. Álvaro, M. Benítez, J. F. Cabeza, H. García and A. Leyva, *J. Phys. Chem. C*, 2007, **111**, 7532-7538.
61. J. W. Park, S. S. Park, I. Kim and C. S. Ha, *Mol Cryst Liq Cryst*, 2007, **463**, 439-446.
62. M. Cornelius, F. Hoffmann, B. Ufer, P. Behrens and M. Fröba, *J. Mater. Chem.*, 2008, **18**, 2587-2592.
63. M. A. Wahab, H. Hussain and C. He, *Langmuir*, 2009, **25**, 4743-4750.
64. N. Mizoshita, Y. Goto, M. P. Kapoor, T. Shimada, T. Tani and S. Inagaki, *Chem. - Eur. J.*, 2009, **15**, 219-226.
65. Y. Goto, K. Nakajima, N. Mizoshita, M. Suda, N. Tanaka, T. Hasegawa, T. Shimada, T. Tani and S. Inagaki, *Microporous Mesoporous Mater.*, 2009, **117**, 535-540.
66. S. Inagaki, O. Ohtani, Y. Goto, K. Okamoto, M. Ikai, K. Yamanaka, T. Tani and T. Okada, *Angew Chem Int Ed Engl*, 2009, **48**, 4042-4046.
67. H. Takeda, Y. Goto, Y. Maegawa, T. Ohsuna, T. Tani, K. Matsumoto, T. Shimada and S. Inagaki, *Chem Commun (Camb)*, 2009, DOI: 10.1039/b910528j, 6032-6034.
68. M. Waki, N. Mizoshita, T. Tani and S. Inagaki, *Angew. Chem. Int. Ed.*, 2011, **50**, 11667-11671.
69. Y. Yang, X. Zhang and Q. B. Kan, *J. Colloid Interface Sci.*, 2013, **411**, 138-144.
70. F. Auras, Y. Li, F. Lobermann, M. Doblinger, J. Schuster, L. M. Peter, D. Trauner and T. Bein, *Chem. - Eur. J.*, 2014, **20**, 14971-14975.
71. M. Waki, Y. Maegawa, K. Hara, Y. Goto, S. Shirai, Y. Yamada, N. Mizoshita, T. Tani, W.-J. Chun and S. Muratsugu, *J. Am. Chem. Soc.*, 2014, **136**, 4003-4011.
72. M. Yoshida, K. Saito, H. Matsukawa, S. Yanagida, M. Ebina, Y. Maegawa, S. Inagaki, A. Kobayashi and M. Kato, *J. Photochem. Photobiol., A*, 2018, **358**, 334-344.

73. J. G. Croissant, S. Picard, D. Aggad, M. Klausen, C. Mauriello Jimenez, M. Maynadier, O. Mongin, G. Clermont, E. Genin, X. Cattoen, M. Wong Chi Man, L. Raehm, M. Garcia, M. Gary-Bobo, M. Blanchard-Desce and J. O. Durand, *J Mater Chem B*, 2016, **4**, 5567-5574.
74. M. Abboud and A. Sayari, *Microporous Mesoporous Mater.*, 2017, **249**, 157-164.
75. X. Hao, S. Han, J. Zhu, Y. Hu, L. Y. Chang, C. W. Pao, J. L. Chen, J. M. Chen and S. C. Haw, *RSC Adv*, 2019, **9**, 13567-13575.
76. M. Waki and S. Inagaki, *Microporous Mesoporous Mater.*, 2019, **284**, 10-15.
77. X. M. Guo, X. M. Wang, H. J. Zhang, L. S. Fu, H. D. Guo, J. B. Yu, L. D. Carlos and K. Y. Yang, *Microporous Mesoporous Mater.*, 2008, **116**, 28-35.
78. X. M. Guo, H. D. Guo, L. S. Fu, H. J. Zhang, R. P. Deng, L. N. Sun, J. Feng and S. Dang, *Microporous Mesoporous Mater.*, 2009, **119**, 252-258.
79. Y. Li, B. Yan and Y. J. Li, *Microporous Mesoporous Mater.*, 2010, **132**, 87-93.
80. Y. J. Li, L. Wang and B. Yan, *J. Mater. Chem.*, 2011, **21**, 1130-1138.
81. L. N. Sun, W. P. Mai, S. Dang, Y. N. Qiu, W. Deng, L. Y. Shi, W. Yan and H. J. Zhang, *J. Mater. Chem.*, 2012, **22**, 5121-5127.
82. W. Liu, A. M. Kaczmarek, P. Van Der Voort and R. Van Deun, *Dalton Trans*, 2022, **51**, 11467-11475.
83. W. L. Liu, C. H. Liu, L. Pilia, H. L. Zhang, P. van der Voort, A. M. Kaczmarek and R. Van Deun, *Dalton Trans.*, 2023, **52**, 11949-11957.
84. W. L. Liu, A. M. Kaczmarek, H. Rijckaert, P. van der Voort and R. Van Deun, *Dalton Trans.*, 2021, **50**, 11061-11070.
85. A. M. Kaczmarek and P. Van der Voort, *J Mater Chem C*, 2019, **7**, 8109-8119.
86. A. M. Kaczmarek, S. Abednatanzi, D. Esquivel, C. Krishnaraj, H. S. Jena, G. B. Wang, K. Leus, R. Van Deun, F. J. Romero-Salguero and P. Van der Voort, *Microporous Mesoporous Mater.*, 2020, **291**, 109687.
87. H. Li, Y. J. Li, Z. Zhang, X. L. Pang and X. D. Yu, *Mater. Des.*, 2019, **172**, 107712.
88. S. Lu, D. Tu, X. Li, R. Li and X. Chen, *Nano Res.*, 2016, **9**, 187-197.
89. A. M. Kaczmarek, D. Esquivel, J. Ouwehand, P. Van Der Voort, F. J. Romero-Salguero and R. Van Deun, *Dalton Trans*, 2017, **46**, 7878-7887.
90. A. M. Kaczmarek, R. Van Deun and P. Van Der Voort, *J Mater Chem C*, 2019, **7**, 4222-4229.
91. Y. Zhang, S. Yuan, G. Day, X. Wang, X. Yang and H.-C. Zhou, *Coord Chem Rev*, 2018, **354**, 28-45.
92. A. M. Kaczmarek and P. Van Der Voort, *Materials*, 2020, **13**, 566.
93. T. L. Mako, J. M. Racicot and M. Levine, *Chem Rev*, 2019, **119**, 322-477.
94. M. Waki, N. Mizoshita, Y. Maegawa, T. Hasegawa, T. Tani, T. Shimada and S. Inagaki, *Chem. Eur. J.*, 2012, **18**, 1992-1998.
95. M. Guan, W. D. Wang, E. J. Henderson, Ö. Dag, C. Kübel, V. S. K. Chakravadhanula, J. Rinck, I. L. Moudrakovski, J. Thomson, J. McDowell, A. K. Powell, H. X. Zhang and G. A. Ozin, *J. Am. Chem. Soc.*, 2012, **134**, 8439-8446.
96. B. Xiao, J. Zhao, X. Liu, P. Y. Wang and Q. H. Yang, *Microporous Mesoporous Mater.*, 2014, **199**, 1-6.
97. M. S. Moorthy, H. B. Kim, A. R. Sung, J. H. Bae, S. H. Kim and C. S. Ha, *Microporous Mesoporous Mater.*, 2014, **194**, 219-228.
98. A. M. Kaczmarek, Y. Maegawa, A. Abalymov, A. G. Skirtach, S. Inagaki and P. Van Der Voort, *ACS Appl. Mater. Interfaces*, 2020, **12**, 13540-13550.

Chapter 2. Periodic Mesoporous Organosilica Based Sensor for Broad Range Mercury Detection by Simultaneous Downshifting / Upconversion Luminescence



The results of this chapter were published in: Periodic mesoporous organosilica based sensor for broad range mercury detection by simultaneous downshifting/upconversion luminescence. **Chunhui Liu**, Anna M. Kaczmarek, Himanshu Sekhar Jena, Zetian Yang, Dirk Poelman and Pascal Van Der Voort, 2023, Journal of Materials Chemistry C, 11(17), pp.5634-5645.

Abstract

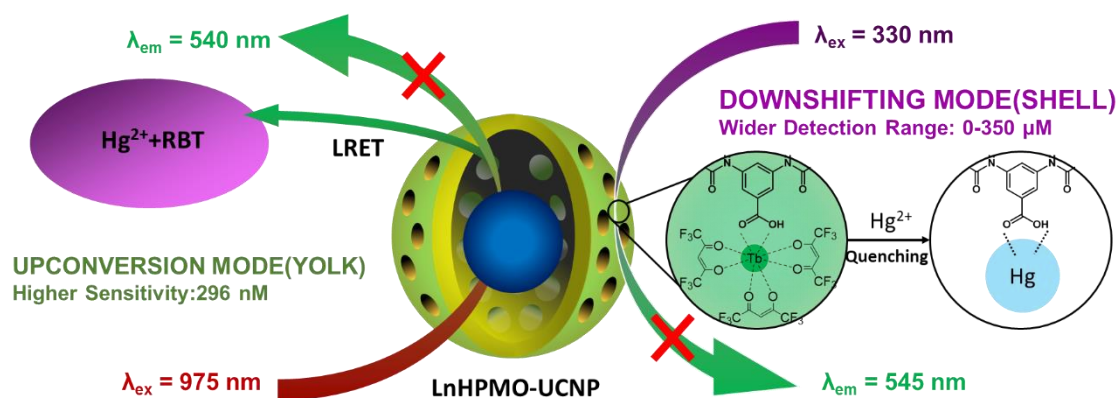
Recent research in lanthanide materials has strongly contributed to the development of high-performance chemical sensors. However, the current reported high-responsive chemical sensors still have a limited detection range, restraining their further application. We developed lanthanide-based periodic mesoporous organosilica (LnPMO) hollow spheres with interior lanthanide-doped fluorides for luminescence turn-off sensing of Hg^{2+} with a low detection limit and wide detection range. This yolk-shell structure was built of Tb^{3+} grafted diureido-benzoic acid PMO (shell) and lanthanide-doped fluoride $\text{NaYF}_4:\text{Yb,Er}$ (yolk), exhibiting both downshifting (DS) and upconversion (UC) luminescence. Visible photoluminescence properties of the developed hybrid material were studied using UV and near-infrared (NIR) excitation. In DS mode, benzoic acid-functionalized PMO acts as an organic co-sensitizer for Tb^{3+} β -diketonate complexes, which can significantly enhance the ion sensing and detection range. In UC mode, Hg^{2+} -responsive Rhodamine B thiolactone (RBT) was used as an antenna species for the lanthanide-doped fluorides to sense Hg^{2+} with high sensitivity

2.1 Introduction

Mercury is a highly hazardous element and an active pollutant in water and air as dissolved salts or volatile organomercury compounds.¹ It cumulates in the body, eventually affecting the immune system, kidneys, cardiovascular, gastrointestinal, and brain systems permanently.² Even at low concentrations, it poses a major risk to human health. A few sophisticated methods, such as field sample preparation-atomic absorption spectroscopy (FSP-AAS), ion mobility spectrometry (IMS), inductively coupled plasma mass spectrometry (ICP-MS), and electrochemical analysis are available for the detection and quantification of Hg^{2+} ions. However, all these methods are either time-consuming, expensive, or show poor repeatability.³⁻⁶ So, in the realm of environmental research and protection, it is crucial to use novel techniques for creating facile, effective, and affordable materials for the selective detection and removal of Hg^{2+} . Our group has published previously on Diffusive Gradient Thin films (DGT) and periodic mesoporous organosilicas to enrich low concentrated aqueous systems and adsorb Mercury compounds respectively.^{7, 8}

Fluorescence-based methods, especially lanthanide-based ion sensors, possess distinctive features like high sensitivity, easiness in operation, and cost-effectiveness.⁹ In addition, lanthanides have gained a lot of attention for a range of applications due to their exceptional photophysical features, such as narrow and easily recognized emission lines, large Stokes shift, and long luminescence lifetime.¹⁰ Due to the parity-forbidden nature of the f-f transitions, the absorption coefficients for these lanthanide ions are generally low.¹¹ The complexation of Ln^{3+} with sensitizing ligands, such as β -diketonates,¹² aromatic carboxylates,¹³ or heterocyclic ligands,¹⁴ is frequently used to efficiently transmit absorbed energy to lanthanide ions ("antenna effect") to tackle this issue.¹⁵ The energy transfer from the antenna to the lanthanide ion is altered as a result of the antenna's coordination with the

target metal ion, which also affects the probe's luminescence. It can be utilized to monitor the change of ion concentration by quantifying the change of the probe luminescence. Additionally, employing time-resolved luminescence measurements to detect metal ions in complex biological and environmental specimens, short-lived auto-fluorescence can fade out when it is comparing to long-emitting lanthanide complexes.¹⁶ A variety of Ln-based ion sensors have been developed to efficiently detect Hg^{2+} from water with high sensitivity, such as lanthanide coordination polymers,¹⁷ lanthanide hybridized carbon quantum dots (Ln-CQDs),¹⁸ and lanthanide metal-organic frameworks (LnMOFs).¹⁹⁻²³ While numerous reports for Hg^{2+} sensing have been reported, there are still many unsolved problems, such as poor stability (thermostability, chemical stability), narrow detection ranges, high poisonousness, and difficulties in large-scale production.



Scheme 2.1 Schematic illustration of LnHPMO@UCNP dual mode ion sensor towards Hg^{2+} (LRET, luminescence resonance energy transfer).

Fluorescent probes have two important characteristics: detection range and sensitivity. The detection range of the probe dictates its applicability range, while the sensitivity provides the (lower) limit of detection.

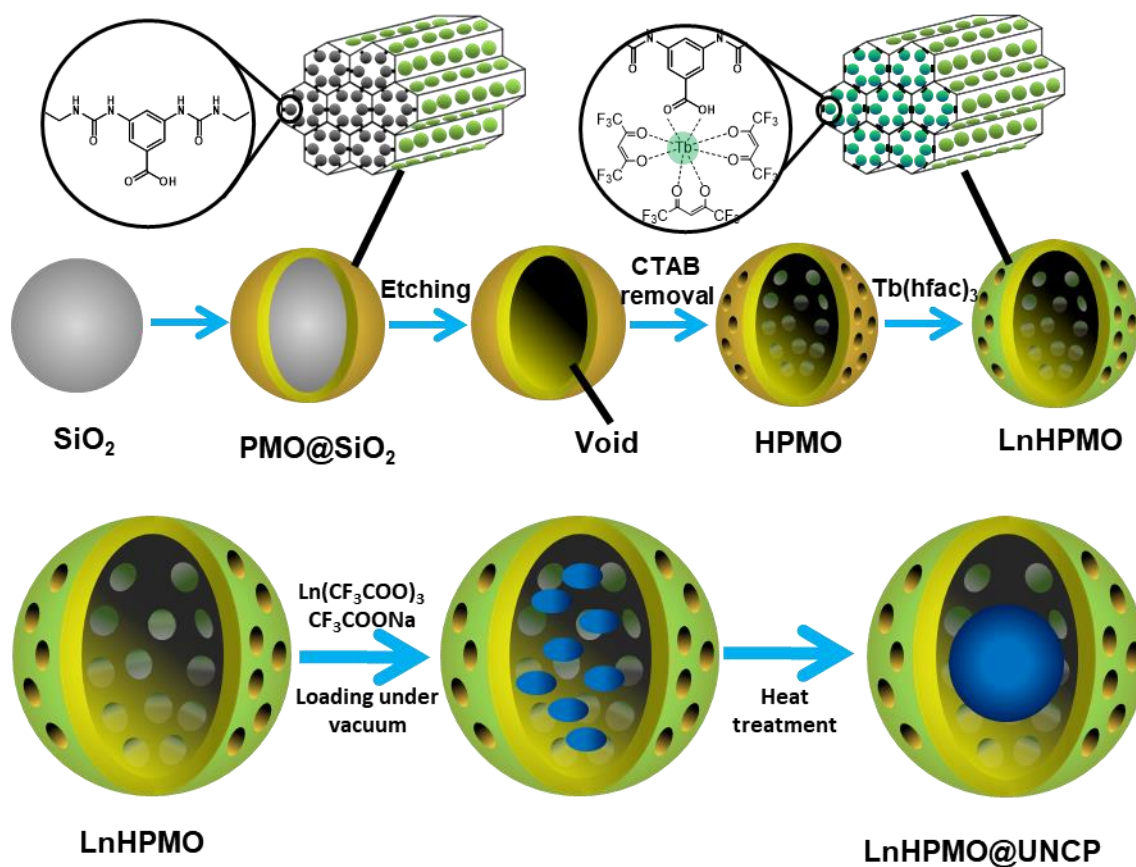
Periodic mesoporous organosilicas (**PMOs**) have become an attractive alternative sensor system due to their stable physicochemical properties, low toxicity, high biocompatibility and easy handling for large scale production.^{24, 25}

Several lanthanide PMO materials (**LnPMOs**) have already been investigated, showing excellent luminescence properties in the visible and near-infrared regions.²⁶⁻³⁰ Lanthanide complexes were immobilized into the silica framework or onto the surface of the pore walls using a one-pot synthesis involving Ln³⁺ complexes and organosilane molecules in the presence of a structure-directing agent. Alternatively to this *in situ* synthesis, post-synthesis impregnation can be utilized to coordinate lanthanide ions to the functional organic moiety of hybrid mesoporous materials, resulting in stable lanthanide-modified luminescent materials that preserve the host material's ordered mesostructure and shape.³¹ Surprisingly, the optical characteristics of **LnPMOs** have only been documented sporadically as chemical sensors over the past decades. It was not until the late 2010s that the field of chemical sensing emerged, coalescing around a small number of articles that sparked the research.³²⁻³⁶ These works, especially concerning Hg²⁺ sensing, constitute the only current knowledge, and as such, the field has received scant attention in the research literature. This is likely because the lanthanide hybrid materials with large detection range suffer from poor luminescent properties and low sensitivity towards cations. Consequently, the deliberate design and construction of **LnPMOs** as chemical sensors towards Hg²⁺ remains a considerable challenge.

In this work, we developed **lanthanide periodic mesoporous organosilica (LnPMO)** based yolk-shell structure for luminescence turn-off sensing of Hg²⁺. This structure consists of Tb³⁺ complex grafted diureido-benzoic acid **hollow PMO (HPMO, shell)** and lanthanide-doped fluorides NaYF₄: Yb, Er (**UCNP, yolk**), exhibiting both downshifting (DS) and upconversion (UC) luminescence. Since the benzoic acid triplet state slightly outstrips the β-diketone ligand, making it a good match for the Tb³⁺ ion, we utilized the diureido-benzoic acid-functionalized PMO for chelation of

the Tb^{3+} complex.³⁷ To circumvent the narrow detection range of high sensitivity ion sensors, this study was set out to combine the large detection range of LnPMOs with the high sensitivity of **Rhodamine B thiolactone dye coupled upconversion luminescence nanoparticles (UCNP+RBT)** (Scheme 2.1). On top of downshifting chemical sensors, upconversion luminescence (UCL) has emerged as a promising method for sensing (ion sensing, temperature sensing, solvent sensing)³⁸⁻⁴¹ and bioimaging.⁴² UCL of rare-earth nanophosphors is a multi-photon absorption or energy transfer process that converts low-energy light into higher-energy visible light.⁴³ As one of the most prominent upconversion luminescence nanoparticles (**UCNPs**), lanthanide-doped $\beta\text{-NaYF}_4$ nanoparticles possess low autofluorescence, strong chemical and optical stability. They have been widely used as the most efficient (highest quantum yield) systems for green UCL.⁴⁴ The Hg^{2+} -responsive Rhodamine B thiolactone (RBT) dye possesses an absorption band at around 450-600 nm, which can perfectly absorb the green emission from UCNPs causing luminescence quenching.^{45, 46} There is no photobleaching or autofluorescence interference when using **UCNPs** as a luminescent sensor for Hg^{2+} detection. Even for samples measured in actual water or in biological systems, it can still provide highly selective and sensitive data.⁴⁷ Lanthanide-doped fluorides are conceivable to be produced through heat treatment from the alkali metal and lanthanide trifluoroacetates. These fluorides have a good UCL but an uncontrolled morphology with micron-size particles.⁴⁸ These materials with irregular morphology and size are not useful for chemical sensing. Rather than bulk materials larger than 1 μm , nanometer-sized particles are required to provide a quick mass transfer, excellent adherence to surfaces, and good suspension in solution.⁴⁹ Based on such consideration, we employed the hard-core templating technique for the conformation of size-controlled, hollow-structured LnPMOs (**LnHPMO**), then

fabricate downshifting/upconverting luminescent submicron structure by incorporating lanthanide-doped fluorides into pre-synthesized **LnHPMO**.⁵⁰



Scheme 2.2 Schematic illustration of the preparation of the LnHPMO@UCNPs yolk-shell structure.

The paper is organized as follows (Scheme 2.2). In section 2.3.1, we present the characterizations of whole yolk-shell structure (LnHPMO@UCNP). In section 2.3.2, we show the chemical sensing performance (DS mode) of HPMSs grafted Tb³⁺ complex with the ancillary ligand (hexafluoroacetylacetonate) before the introduction of UCNPs. In section 2.3.3, we prove the sensing ability of UCNPs coupled with RBT towards Hg²⁺ (UC mode) when integrated inside the LnHPMSs. In section 2.3.4, we show that the DS mode still functions after the introduction of UCNPs. We demonstrate that this LnHPMS based yolk-shell structure is amenable to a range of chemical sensing applications. In both downshifting and upconversion modes, linear

relationships between the relative fluorescence intensity ratio of the sensor and ion concentrations were explored and compared in wide detection range.

2.2 Experimental

2.2.1 Materials and Instrumentation

$\text{Ln}(\text{CF}_3\text{COO})_3$ (Ln = Er, Yb) precursors were prepared according to a reported procedure.⁵¹ All other chemicals including $\text{Y}(\text{CF}_3\text{COO})_3$ and CF_3COONa were purchased from Sigma Aldrich, Fluorochem, Alfa Aesar, or TCI Europe and used without further purification.

Powder X-ray diffraction (PXRD) patterns were obtained using a Bruker D8 Advance diffractometer with a $\text{Cu K}\alpha$ ($\lambda = 1.5405 \text{ \AA}$) source in Bragg–Brentano configuration. Diffuse reflectance infrared Fourier transform spectroscopy (DRIFTS) was recorded with a Graseby Specac diffuse reflectance cell on a Thermo Scientific Nicolet 6700 hybrid IR-Raman spectrophotometer equipped with a nitrogen cooled mercury cadmium telluride (MCT-A) detector. Using a DRIFT chamber and KBr/sample mixtures, data was collected in the range of $650\text{--}4000 \text{ cm}^{-1}$. Nitrogen adsorption–desorption isotherms were measured on a Micromeritics TriStar 3000 analyzer at 77 K. Prior to measurement, all samples were degassed for 24 hours at 120°C . The surface areas and pore size distributions of the samples were calculated using the Brunauer–Emmett–Teller (BET) and non-local density functional theory (NLDFT, N_2 at 77K, using the kernel of silica cylindrical pore, adsorption branch) methods, respectively. For ^1H NMR, the spectra were acquired on a Bruker 300 MHz AVANCE spectrometer by dissolving the materials in deuterated chloroform (CDCl_3) or Dimethyl sulfoxide- d_6 ($\text{DMSO-}d_6$). Using V_2O_5 as a catalyst, elemental analysis (CHNS) was finished using the Thermo Flash 2000 elemental analyzer. Transmission Electron Microscopy (TEM) images were captured using a Cs-corrected JEOL JEM2200FS transmission electron microscope with a 200 kV operating voltage. The

presence of lanthanide ions inside the PMO materials was demonstrated using high-angle annular dark-field imaging-scanning transmission electron microscope (HAADF-STEM) and energy dispersive X-ray (EDX) mapping analyses. The photoluminescence of PMO colloidal suspensions were monitored in quartz cuvettes with a 10 mm path length at a concentration of 1 mg of the sample dispersed in 1 ml water. The excitation and emission spectra were captured using an Edinburgh Instruments FLSP920 UV-vis-NIR spectrometer with a 450 W xenon lamp and a continuous wave 975 nm laser with an output power of 400 mW as the steady state excitation source for downshifting and upconversion luminescence measurements, respectively. Luminescence decay profiles were measured using a 60 W pulsed xenon lamp. All emission spectra in the manuscript were corrected for the detector response. X-ray fluorescence (XRF) was measured by XRF Supermini 200 Rigaku to analyze the relative metal contents.

2.2.2 Synthesis

Synthesis of 3,5-bis(3-(3-(triethoxysilyl)propyl)ureido)benzoic acid (BA-Si): The 3,5-bis(3-(3-(triethoxysilyl)propyl)ureido)benzoic acid (BA-Si) was synthesized according to a previously reported procedure.³⁷ (3-Isocyanatopropyl)triethoxysilane (ICPTES) (7.5 mL, 30 mmol) was added to a stirred solution of 3,5-diaminobenzoic acid (1.52 g, 10 mmol) in 15 mL of dry Dimethylformamide (DMF), and the combined solution was continuously stirred overnight at 70 °C. Under reduced pressure, the solvent DMF was pumped off. The solution was filtered after a specified amount of ethanol was added. The grey precipitate was produced after 200 mL of petroleum ether was added to the solution. Filtration was used to collect the precipitate, then washed with a large amount of petroleum ether and vacuum-dried at 50 °C. ¹H NMR (300 MHz, DMSO-d₆) δ 12.68 (s, 1H), 8.55 (s, 2H), 7.58 (d, J = 2.0 Hz, 3H), 6.11 (t, J =

5.7 Hz, 2H), 3.82 – 3.68 (m, 12H), 3.05 (q, J = 6.7 Hz, 4H), 1.54 – 1.39 (m, 4H), 1.14 (td, J = 7.0, 2.7 Hz, 18H).

Synthesis of SiO₂ nanoparticles: Hollow diureidobenzoic acid-PMOs (hereinafter referred to as PMO) with a size of 419 ± 14 nm were prepared using homemade silica sub-micron particles as the template and a simple etching approach.⁵² In a flask placed in a water bath at 30 °C, 135 mL ethanol, 2 mL distilled water, and 15 mL 25% ammonia solution were combined and magnetically stirred. Then, under continuous stirring, 6 mL tetraethyl orthosilicate (TEOS) was swiftly added, and the reaction was stopped after 24 hours. Without further filtration, the particles were left in a suspension. The particle size distribution has shown in Figure S2.4. The silica nanoparticles have a size of 217 ± 18 nm.

Synthesis of PMO@SiO₂: To prepare core-shell PMO@SiO₂ particles. 1.3 g cetyltrimethylammonium bromide (CTAB) and 230 mL distilled water were mixed in a 500 mL flask.⁵³ This was heated to 30 °C, the liquid was stirred until CTAB was completely dissolved. After that, 100 mL of the as-prepared suspension of SiO₂ core particles was added and stirred for 30 minutes. Following that, a mixture of 0.35 g (20 mol%) BA-Si and 0.8 mL 1,2-Bis(triethoxysilyl)ethane (BTESE) was added dropwise, and the reaction was left to stir overnight. The product was collected using centrifugation (8000 RPM) and washed 3 times with water and ethanol before being dried in air at 80 °C.

Synthesis of HPMO (etching process): HPMO particles were created by etching the SiO₂ core away. 1 g of dried core-shell SiO₂@PMO particles were mixed with 6.36 g of Na₂CO₃ in 200 mL distilled water in a flask. The mixture was brought to 80 °C and stirred for one hour. The particles were then centrifuged and washed 3 times with distilled water before being dried in air at 80 °C. In a final step, CTAB was removed from the pores to ensure the materials were porous. The samples were

extracted by three consecutive treatments. 100 mL ethanol and 1 mL concentrated HCl were combined in each extraction. Each extraction took 6 hours at 80 °C. After that, the product was centrifuged and rinsed multiple times with distilled water and ethanol. It was dried overnight in a vacuum oven at 120°C. CHNS elemental analysis: C, 41.129; N, 10.568; H, 6.361.

Synthesis of $Tb(hfac)_3 \cdot n(H_2O)$: Tb(III) tris-hexafluoroacetylacetonate hydrates were prepared through a slightly modified procedure from Richardson et al.⁵⁴ Firstly, 0.83 mL of 1.2 M $TbCl_3$ was put in a separation funnel. 0.62 g (3 mmol) of $HHfac \cdot 2H_2O$ was dissolved in 8.33 ml of ethyl ether and 0.22 ml NH_4OH (25%) was added to make an ethereal solution of NH_4hfac (~3 mmol). The aqueous $TbCl_3$ solution was then extracted twice with 4.17 ml of ethereal NH_4hfac . The organic phase was rinsed with 0.83 mL H_2O and dried with Na_2SO_4 . The resulting products were separated by filtration. A stream of dry air was used to evaporate the ether. XRD pattern is shown in Figure S2.2.⁵⁵

Synthesis of LnHPMO: The materials were synthesized in Pyrex test tubes using a heating block. A 10 times molar amount of the pre-synthesized $Tb(hfac)_3 \cdot n(H_2O)$ complex was added to 20 mg of the HPMOs. The suspension was then treated with ultrasound for 15 minutes after adding 10 mL of methanol. Then, the Pyrex tubes were carefully sealed and placed on a heating block for 24 hours at 80 °C. Following that, the product was allowed to cool to ambient temperature before being centrifuged and washed twice with ethanol. It was then dried overnight in an oven at 80 °C. CHNS elemental analysis: C, 16.731; N, 3.72; H, 2.929.

Synthesis of yolk-shell structure LnHPMO: The synthesis procedure was adapted from the previously reported procedure.⁵⁰ The ratio of dopants was determined according to the previous paper to tune the UC emission color to green.⁵⁶ HPMO (30 mg) was introduced to a flask and degassed for 2 hours at room

temperature. The flask was then injected with a solution of 1.03 g $Y(CF_3COO)_3$, 0.23 g $Yb(CF_3COO)_3$, 0.08 g $Er(CF_3COO)_3$, and 1.02 g CF_3COONa dissolved in 5 mL distilled water. The suspension was then stirred at room temperature for 5 hours under vacuum before stirring for 24 hours in ambient air. It was then centrifuged at 3500 RPM for 4 minutes. After drying at 80 °C overnight to eliminate any residual moisture, the sample was heat treated in air at 300 °C at a rate of 1 °C/min for 6 hours to allow for crystallization of the inorganic material. Metal contents are tested by X-ray fluorescence (XRF) in Table S3.1.

Synthesis of Rhodamine B thiolactone (RBT): The Rhodamine derivative was prepared following the procedure of Ma et al.⁵⁷ Phosphorus oxychloride (0.3 mL) was added dropwise to a stirred solution of rhodamine B (239 mg, 0.5 mmol) in 1,2-dichloroethane (5 mL), and then refluxed for 4 hours. After cooling, the solution was evaporated to yield the crude product (Rhodamine B acid chloride). The crude acid chloride was dissolved in tetrahydrofuran (THF, 6 mL) and dropped into a mixed solution of thiourea (152 mg, 2 mmol) and triethylamine (1.2 mL) in THF (5 mL)/water (1 mL) at room temperature. After a night of stirring, the solvent was removed by rotary evaporator to yield a violet-red oil. Subsequently, 5 mL of water was added to the oil, and the precipitate was filtered. The precipitate was rinsed with water many times before drying in air, yielding a violet-red powder. ¹H NMR (300 MHz, Chloroform-d) δ 7.78 (d, J = 7.5 Hz, 1H), 7.49 – 7.35 (m, 2H), 7.16 – 7.12 (m, 1H), 6.64 (d, J = 8.7 Hz, 2H), 6.29 – 6.19 (m, 4H), 3.26 (q, J = 7.1 Hz, 8H), 1.09 (t, J = 7.1 Hz, 12H).

2.3 Results and Discussion

2.3.1 Characterization of LnHPMO@UCNP

An overview of the developed PMO-inorganic hybrid materials is illustrated in Scheme 2.2. Using 1,2-bis(triethoxysilyl)ethane (BTESE) and 3,5-bis(3-(triethoxysilyl)

propyl) ureido) benzoic acid (BA-Si) (20 mol%) as co-precursors, mesostructured organosilica sub-micron particles with ethane- and benzoic acid-functionalized groups were produced through a CTAB-directed sol-gel process.

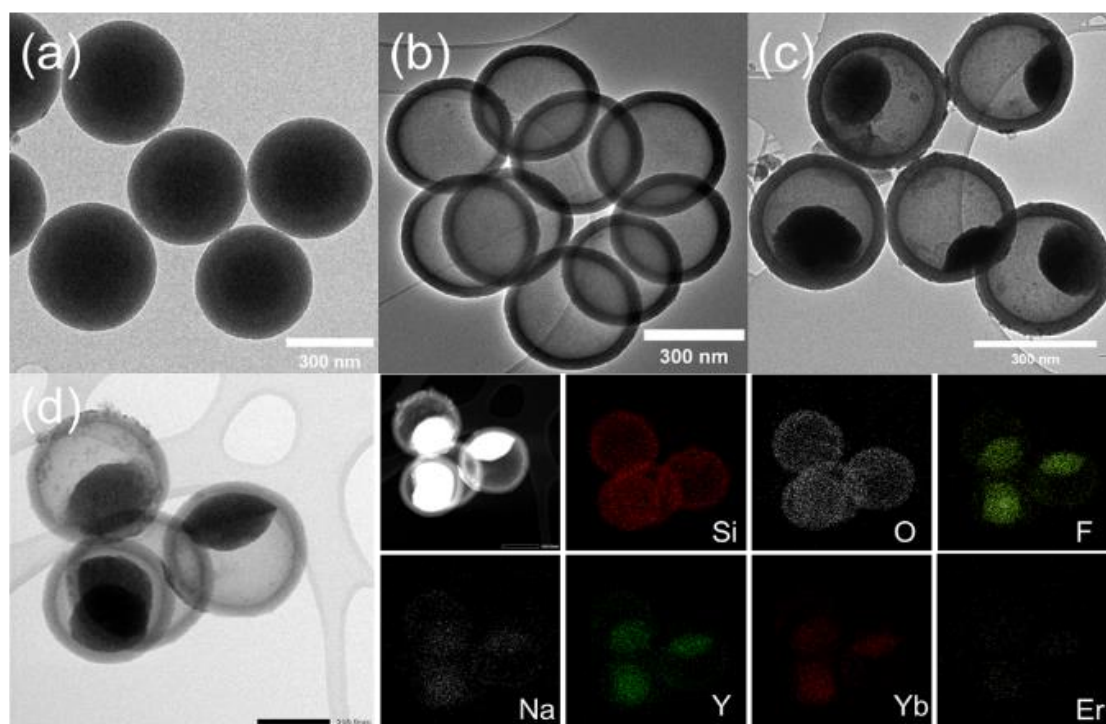


Figure 2.1 TEM images of (a) PMO@SiO₂; (b) hollow PMO (HPMO); (c) HPMO@UCNP; (d) TEM, STEM, and corresponding elemental (Si, O, F, Na, Y, Yb, Er) mappings of HPMO@-UCNP particles.

The prepared HPMO was characterized using transmission electron microscopy (TEM), powder XRD, nitrogen sorption and FT-IR spectroscopy. The as made organosilica sub-micron particles (PMO@SiO₂) consistently have a spherical shape and a diameter of 419 ± 14 nm, based on the TEM images (Figure 2.1a). By etching out the SiO₂ core in PMO@SiO₂, voids are created for the following loading with lanthanide-doped upconversion nanoparticles (UCNPs). Figures 2.1b and 2.1c show typical TEM images of HPMO with a size of roughly 382 ± 21 nm before and after integration of lanthanide-doped fluoride UCNPs, respectively. The fluoride UCNP occupies about half of the cavity of HPMO, which is 203 ± 9 nm in size. By using high-resolution TEM (HRTEM), the fluoride UCNP in HPMO was shown to be well-

crystallized (Figure 2.1c). Figure 2.1d shows TEM, STEM, and associated elemental (Si, O, F, Na, Y, Yb, Er) mappings of the single HPMO@UCNP particle, revealing the yolk-shell structure, where the inorganic fluoride nanoparticle is integrated inside the void of the HPMO. The peak at 2 degrees in the small angle XRD pattern (Figure 2.2a) indicates uniformity in the pores but no further ordering of the HPMO particles. This XRD pattern in combination with the TEM observations are sometimes referred to as wormhole materials.⁴⁹ The creation of such ordered mesoporous structure is possibly caused by the diureido-benzoicacid-bridged silane's low solubility in aqueous environment due to the benzene moiety's high hydrophobicity.⁴⁹ In addition, it shows the mixture of cubic α - and hexagonal β -phase of NaYF₄:Yb,Er in Figure 2.2b (JCPDS 77-2042, JCPDS 28-1192). The low content of α -NaYF₄:Yb,Er is mainly because of the incomplete transition to β -phase of NaYF₄:Yb,Er during relatively low temperature (300°C) heat treatment, but due to risk of HPMO decomposition, higher temperature was not used.⁵⁸ Although it is known that the UCL intensity of the hexagonal phase is much higher than that of the cubic phase, the low content of cubic-phase NaYF₄:Yb,Er does not have a severe influence on the performance of the chemical sensor.

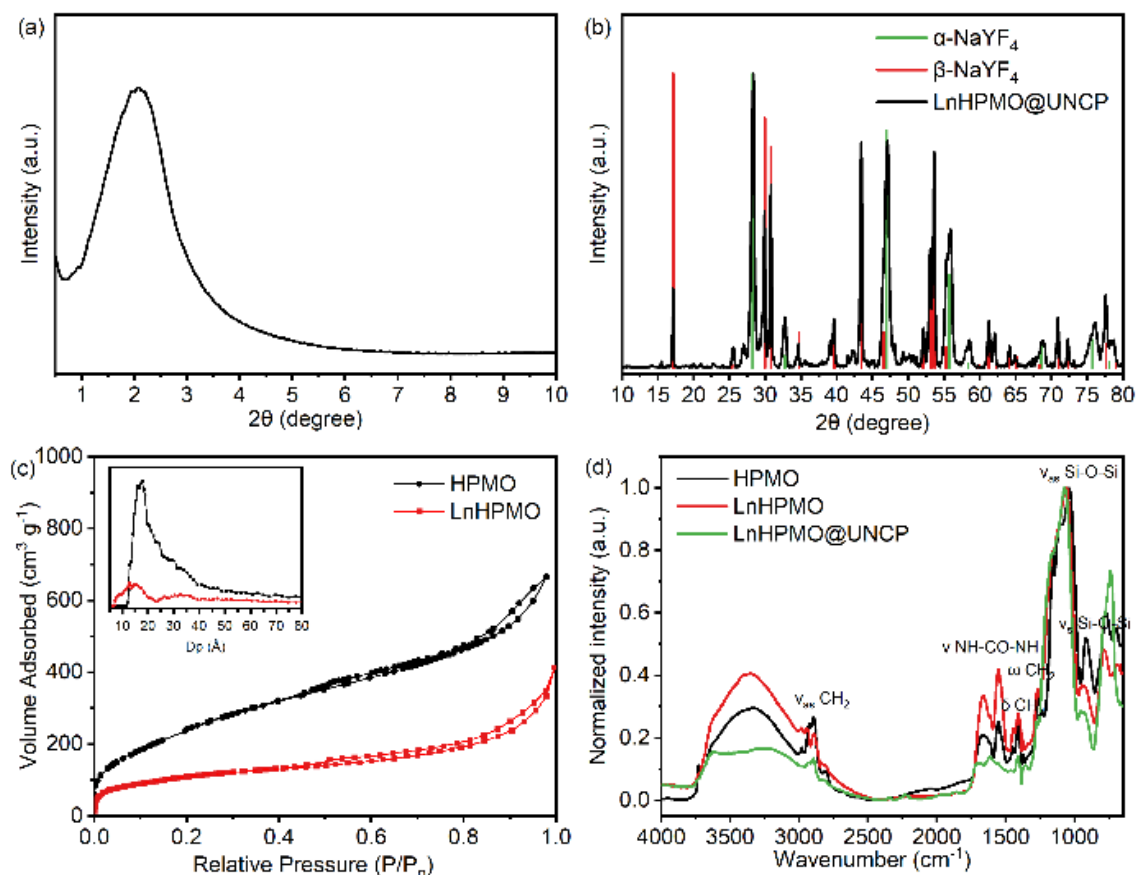


Figure 2.2 (a); (b) XRD patterns of HPMO and LnHPMO with α - and β - NaYF₄: Yb, Er mixed UCNP; (c) N₂ adsorption–desorption isotherms and pore size distributions of HPMO and LnHPMO; (d) FT-IR spectra of HPMO, LnHPMO, and LnHPMO@UNCP.

In order to evaluate the porosity and surface area, N₂ adsorption-desorption isotherms of HPMO and LnHPMO were recorded. In the P/P_0 range of 0.45-1.0, the N₂ adsorption-desorption isotherms show a type-IV curve with an H4 hysteresis loop, indicating a mesoporous structure with a hollow cavity (Figure 2.2c).^{59, 60} After introducing the ancillary ligand, the total pore volume of HPMO reduces from 0.98 to 0.59 cm³/g, and the BET area decreases from 917 to 390 m²/g. The pores in the walls of the HPMOs are around 2 nm radius (inset of Figure 2.2c) and get slightly reduced in size and volume upon functionalization (down to approximately 1.5 nm radius), which is largely sufficient for the purpose of metal sensing. The sizes of the hollow cavities themselves cannot be measured by gas sorption but are clearly visible in the TEM images.

The functional groups immobilized on the sub-micron particles are further shown by FT-IR spectroscopy in Figure 2.2d. The spectrum of LnHPMO@UCNP shows a series of peaks at 1638 cm^{-1} and 1562 cm^{-1} ascribed to the vibrations of NH–CO–NH.³⁷ This demonstrates the preservation of organic groups in the shell after filling with trifluoroacetates precursors and heat treatment at $300\text{ }^{\circ}\text{C}$.

2.3.2 Downshifting mode: sensing performance of the shell, LnHPMO

Firstly, we tested the performance of Tb^{3+} grafted HPMO as the chemical sensor before the incorporation with UCNPs. The material's detecting ability was tested by using a suspension with a 1 mg/mL concentration. Figure 2.3a shows the photoluminescence properties of the HPMO material measured at room temperature. The excitation spectrum has a wide band between 250 and 375 nm with a maximum of 328 nm .

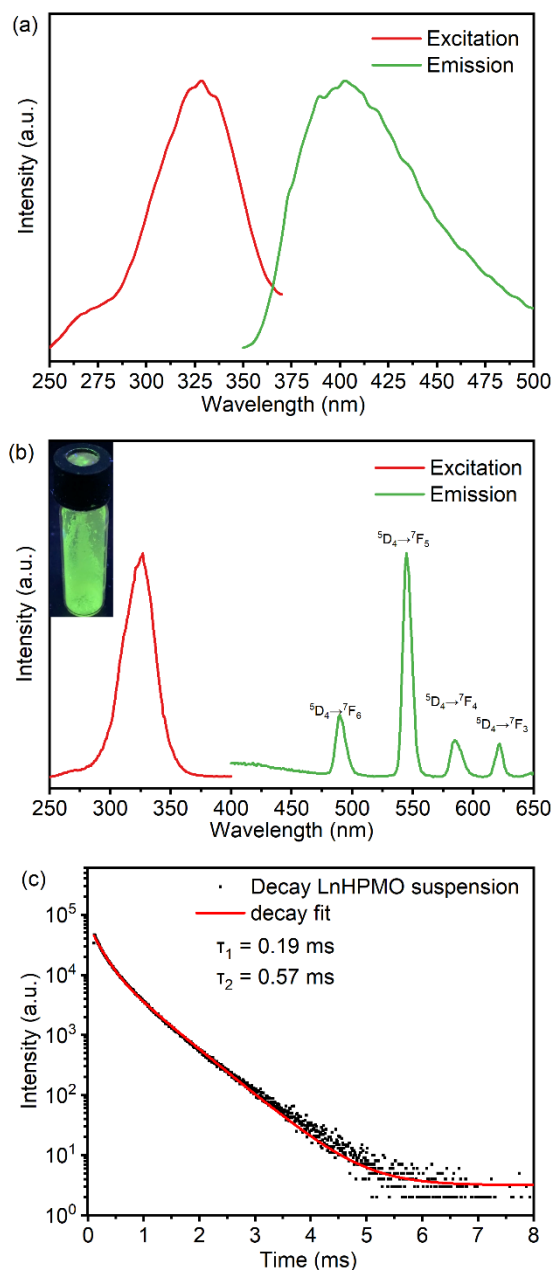
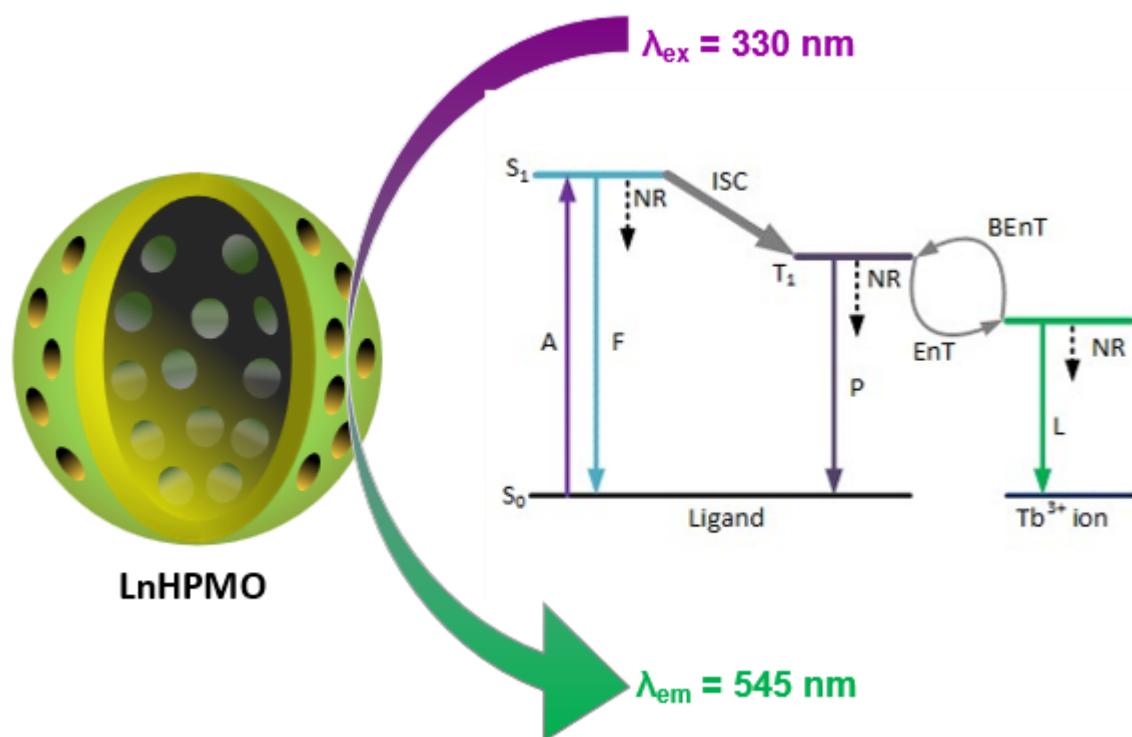


Figure 2.3 (a) Combined RT excitation-emission spectrum of the HPMO (excited at 366 nm observed at 439 nm); (b) Combined RT excitation-emission spectrum of the LnHPMO, ex = 317 nm, em = 545 nm; (c) Logarithmic luminescence decay profile of LnHPMO in water, ex = 317 nm, em = 545 nm.

The emission band is acquired upon excitation at the peak maximum of the excitation spectrum. The emission has a broad wavelength range of 350-500 nm, with a peak at 400 nm. The luminescence characteristics of this hybrid material was examined when the PMO material was grafted with Tb(hfac)₃ complexes. Instead of lanthanide salts, lanthanide complexes were used for grafting to give an ancillary

ligand that would serve as a secondary antenna ligand and shield the lanthanide ions from quenching by water molecules.⁶¹ The luminescence of Tb^{3+} is mainly sensitized by the organic ligands within the frameworks (Scheme 2.3).



Scheme 2.3 Schematic diagram of ligand-to-Tb energy transfer in LnHPMO. (A, absorption; F, fluorescence; P, phosphorescence; L, Tb-centered luminescence; S, singlet; T, triplet; EnT energy transfer; and BEnT back energy transfer)

The combined excitation-emission spectra of PMO@Tb_hfac are shown in Figure 2.3b. The excitation spectrum shows a wideband about 300-350 nm. In the excitation spectrum, there are no visible f-f transitions. The typical Tb^{3+} peaks for PMO@Tb_hfac are observed when the material is excited to the maximum of the broad band. In Figure 2.3b, the indicated peaks have been assigned to the proper transitions. When the sample is exposed to UV light (302 nm excitation), it emits a bright green color, as seen in Figure 2.3b inset. The sample's luminescence decay time was measured upon at 317 nm and probed at 545nm. A good fit could be obtained using a biexponential decay curve, which indicates that more than one coordination environment of the lanthanide ions is present in the hybrid materials

(Figure 2.3c). This is expected from the BA-Si structure, which also possesses the urea moiety offering coordination sites, next to the carboxylic acid sites. Based on this, the following rate law can adequately characterize the decay in the presence of varying coordination environment:

$$I(t) = A_1 \exp(-t/\tau_1) + A_2 \exp(-t/\tau_2) \quad (1)$$

where τ_1 and τ_2 are short- and long- lifetimes, with corresponding intensity coefficients A_1 and A_2 , respectively. These values varied from one measurement to another, but the average decay time was found to be constant within $\pm 0.5\%$ the whole time during measurement.⁶²

$$\bar{\tau} = (A_1\tau_1^2 + A_2\tau_2^2)/(A_1\tau_1 + A_2\tau_2) \quad (2)$$

so the average decay time $\bar{\tau}$ is calculated to be 0.390 ms ($\tau_1 = 0.19$ ms, $\tau_2 = 0.57$ ms).⁶³

The photophysical properties of lanthanide luminescent PMOs are attributed to the f-f transition of Ln^{3+} . The combination of luminescence and accessible porosity in PMOs impels them to respond to detectable changes in their detection environment. It demonstrates a promising future for turn-off chemical sensing applications by transforming alternate guest motifs via host-guest interactions.⁶⁴ To investigate the metal ion selectivity behavior of the LnHPMO materials, fluorescence experiments were conducted for several metal ions (Figure 2.4). As-synthesized samples were added to several standard solutions containing 10 ppm of metal nitrate. The target suspensions were successfully prepared by using ultrasound for around 10 minutes. In Figure 2.4a, the corresponding photoluminescence spectra are gathered and compared. The results show that most suspensions containing a variety of metal ions emit the characteristic green light due to Tb^{3+} transitions, but only Hg^{2+} leads to a significant attenuation of luminescence intensity (quenching effect). It manifests the high selectivity of PMO@Tb_hfac for the detection and

specific recognition of Hg^{2+} in an aqueous solution. With UV light excitation (302 nm), quintessential quenching effect can be captured by the naked eye (inset of Figure 2.4a). These differences can be explained in part by the Hg(II) static quenching mechanism caused by the formation of nonfluorescent ground-state complex.⁶⁵ In detail, Hg(II) can contain a wide range of coordination numbers and geometries due to its $5d^{10}6s^2$ electronic configuration and deficiency of ligand field stabilization energy. Because Hg(II) is a soft acid, the use of well-suited donor atoms (e.g. N,O atoms) in a chelating unit will impetus its affinity for Hg(II) .⁶⁶ In summary, the free carboxylate oxygen atoms can act as the electron donors donating electrons to the Hg^{2+} ions to form a weak $\text{O}\cdots\text{Hg}$ bond. It is no longer possible to sensitize Tb^{3+} emission by transferring energy from PMO, resulting in energy migration and luminescence quenching. As shown in

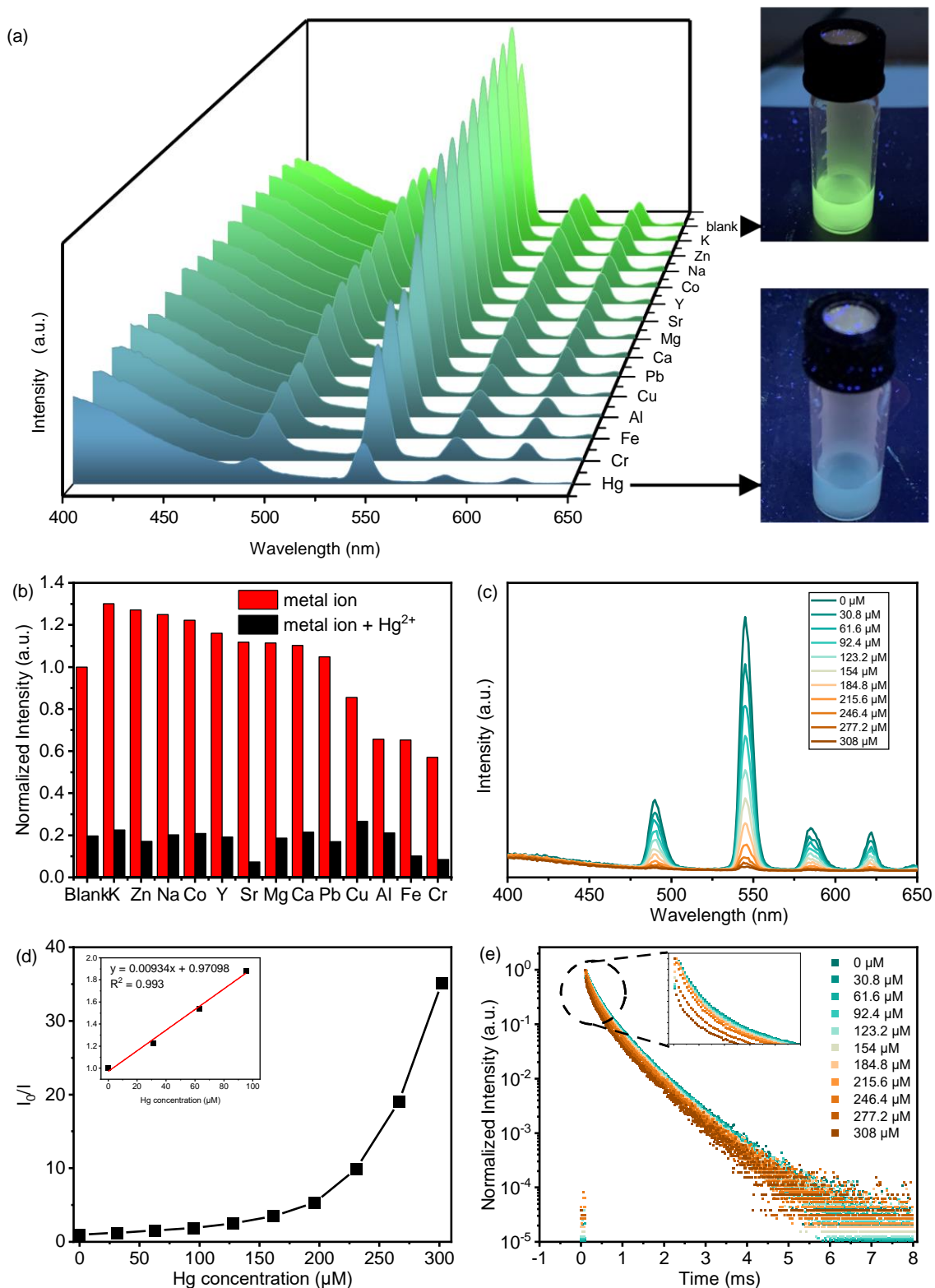


Figure 2.4 (a) Emission spectra of the colloidal suspensions of LnHPMO in the presence of different metal ions when excited at 317 nm; (b) Comparison of the luminescence intensities (545 nm) of LnHPMO with varied ions before and after treated by Hg²⁺; (c) Luminescence spectra of LnHPMO under different concentrations of Hg²⁺ aqueous solutions; (d) Plot of the Stern-Volmer curve between the luminescence intensity and Hg²⁺ concentration in an aqueous solution; (e) Luminescence decay profile of colloidal suspensions of LnHPMO in the presence of different metal ions.

Selectivity is a critical indicator for evaluating the efficacy of sensing material in detecting specific analytes without being impacted by other components of the environment in practical applications.⁶⁷ So, the LnHPMO (1 mg) was ultrasonically dispersed in 1 mL of deionized water, and the luminescence intensity did not change distinctly when other ions were added. The fluorescence intensity at 545 nm was promptly quenched when equal concentration Hg^{2+} solutions were introduced, as shown in Figure 2.4b. The observed selectivity for Hg^{2+} over Cu^{2+} and Pb^{2+} , which are primary competitors in real-life field samples is noteworthy. It implies that these metal cations had no impact on PMO@Tb_hfac for Hg^{2+} detection, further validating the selectivity of PMO@Tb_hfac for Hg^{2+} detection and its potential for practical application.

Luminescence titration tests were also carried out to quantitatively explore the luminescence response behavior of PMO@Tb_hfac towards Hg^{2+} ions. The emission intensity of PMO@Tb_hfac decreases significantly as the Hg^{2+} concentration increases (Figure 2.4c). The fluorescence emission of the Tb^{3+} hybrid solution was totally quenched when the Hg^{2+} concentration reached 308 μM . The luminescence quenching efficiency (K_{sv}) was calculated using the Stern-Volmer (S-V) equation:

$$\frac{I_0}{I} = K_{sv}c + 1 \quad (3)$$

where I_0 and I are the luminescence intensities of PMO@Tb_hfac suspension before and after the addition of the Hg^{2+} ion, respectively, and c is the molar concentration of Hg^{2+} .^{33, 68} An excellent linear relation ($R^2 = 0.993$) was achieved in the concentration range of 0 to 100 μM (Figure 2.4d). The calculated K_{sv} value is 9345 M^{-1} . The curve becomes nonlinear when the Hg^{2+} concentration is larger than 100 μM . In general, if the S-V curve has an upward curvature, it illustrates that Hg^{2+} -induced fluorescence quenching is accompanied by both static and dynamic quenching.⁶⁹ However, a comprehensive proof through decay time experiment is

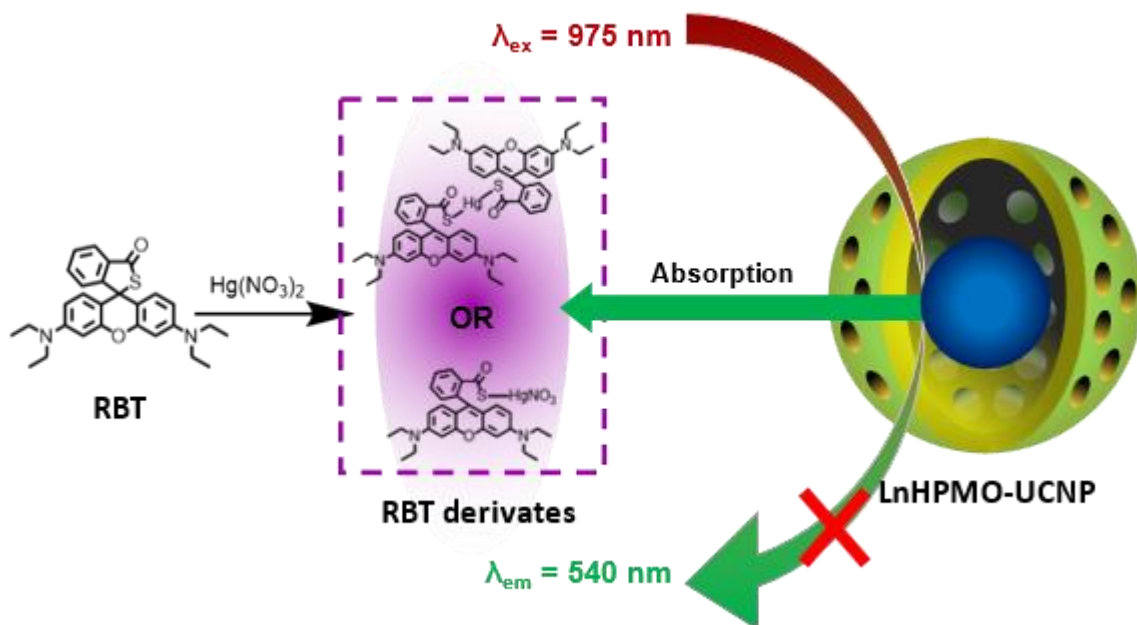
needed.³³ As shown in Figure 2.4e, the decrease in luminescence lifetime after the addition of the quencher further validates the presence of a dynamic process in the luminescence quenching processes. This type of quenching, called dynamic quenching or collisional quenching, occurs when an excited luminescent molecule (*L) collides with a quencher molecule (Q). This collision disrupts the excited state of *L, preventing it from emitting light (photons). Instead, the excitation energy is transferred to the quencher molecule (Q). As a result, the excited state of *L doesn't last as long, leading to a decrease in the brightness and overall intensity of the luminescence. It implies that energy transfer from the ligands (benzoic acid, and hfac) to the Tb³⁺ centers has been limited to some extent.⁷⁰ The limit of detection (LOD) was calculated to be 10.1 μM according to the method used by Armbruster et al., assuming that

$$LOD = 3\sigma/K_{SV} \quad (4)$$

where σ is the standard deviation of the response which can be determined based on the standard deviation of blank sample measurement.^{71, 72} Although the LOD is so low enough that it can be comparable to previously reported fluorescence sensors for Hg²⁺ ions, especially lanthanide metal organic frameworks (LnMOFs) which have extremely low limit of detection (e.g. 10 nM),⁷³⁻⁷⁵ it transpires that our turn off fluorescence chemical sensor could be employed firstly as a LnPMOs sensitive probe for Hg²⁺ ion quantification in aqueous conditions at a wide detection range. Furthermore, up to date, only few mercury sensors based on LnPMOs have been reported as the turn-on fluorescence chemical sensor,^{34, 36} so it is hard to compare these materials with the LnPMOs from our work (Table 2.1).

2.3.3 Upconversion mode: sensing performance of the yolk: UCNP+RBT

Rare earth fluorides offer the benefits of low phonon energy, high luminous efficiency, and robust stability among the numerous up-converting luminescent hosts. As a result, the best matrix materials for up-conversion luminescence have been identified as sodium yttrium fluoride (NaYF_4) crystals.⁷⁶ Figure 2.5(a) provides a schematic representation of the $\text{NaYF}_4:\text{Yb,Er}$ UC populating and emission processes, with the green and red emissions both resulting from two-photon processes. However, contrary to the relatively weak coordination bond of Tb^{3+} grafted materials, $\text{NaYF}_4:\text{Yb,Er}$ is rarely used independently for ion sensing by standard quenching mechanism. Instead, it was utilized as energy donor in luminescence resonance energy transfer (LRET) investigations. In the work of Wang et al.,⁴⁴ an upconversion LRET (UC-LRET) sensor was built employing $\text{NaYF}_4:\text{Yb,Er}$ and RBT derivatives as the energy donor and acceptor, respectively. This chemical sensor was based on the UC luminescence quenching by Hg^{2+} . As shown in Scheme 2.4, the high thiophilicity of Hg^{2+} can form two kinds of RBT derivatives. These kinds of dyes possess an absorption band of around 450-600 nm, which can perfectly absorb the emission from UCNPs. Consequently, it will quench the luminescent intensity of UCNPs under NIR excitation.⁵⁷ According to this protocol, we examined the LRET mechanism of UCNPs and RBT in the first set of spectra (Figure 2.5b). What stands out in the figure is the significant difference in the absorption band after adding Hg^{2+} . This can be interpreted by an efficient ring-opening reaction and the formation of pink RBT derivatives.^{44, 57} Further analysis showed their (UCNPs and RBT derivatives) excellent overlapping of absorption and emission bands, which makes the emission of the energy donor will be quenched by the energy acceptor. As a result, a UC-LRET system based on UCNPs+RBT for Hg^{2+} detection appears reasonable and practicable for our UC mode sensor.



Scheme 2.4 Schematic illustration for the reaction mechanism of RBT with $\text{Hg}(\text{NO}_3)_2$ and the mechanism of the UCNP+RBT sensor.

Table 2.1 Comparison of lanthanide-based sensors developed for detection of Hg^{2+}

Fluorescence probe	Linear range	K_{sv} (M^{-1})	LOD (nM)	Ref
Tb-CIP/AMP (LCP)	1.5 - 70 nM	NA	0.16 nM	20
Eu/IPA CPNPs (LCP)	2 nM - 2 μM	NA	2 nM	21
CQDs@Ad-Eu-DPA (Ln-CQDs)	0.001-0.02 μM	NA	0.2 nM	24
2D $\text{Tb}_{0.6}\text{Eu}_{0.4}$ -bop (Ln-MOFs)	0.1-40 μM	NA	4.83 nM	26
BA-Eu-MOF (Ln-MOFs)	1-60 μM	NA	220 nM	29
Eu-Ca-MOF (Ln-MOFs)	0.02–200 μM	NA	2.6 nM	30
AM-PMO2_nano@o-van@Eu(tfac) ₃ (Ln-PMO)	NA	NA	NA	47
PMO@NaYF ₄ :Yb ³⁺ ,Er ³⁺ (PMO@UCNP)	0-214.6 μM	900	24.4 μM	49
PMO: Tb_hfac@NaYF ₄ : Yb,Er (LnHPMO@UCNP)	0-350 μM	78180	296 nM	This work

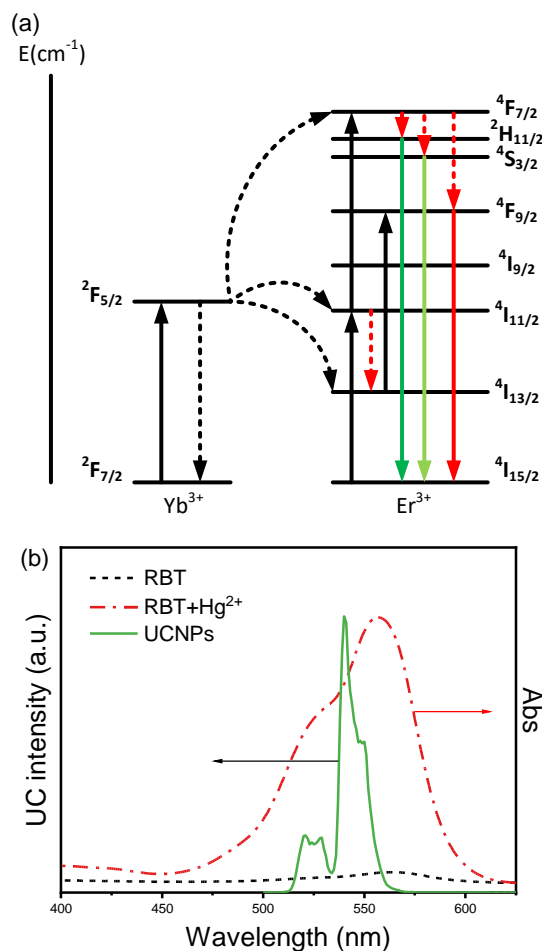


Figure 2.5 Schematic of UC populating mechanism for NaYF₄:Yb,Er under 975 nm excitation. (b) Absorption spectrum of RBT, RBT derivatives ($\lambda_{\text{max}} = 558 \text{ nm}$), and UC luminescence spectrum of UCNPs ($\lambda_{\text{em}}/\lambda_{\text{ex}} = 540 \text{ nm}/975 \text{ nm}$) in water.

After the fabrication of downshifting/upconverting luminescent sub-micron yolk-shell structure by incorporating lanthanide-doped fluorides into hollow LnPMOs, the fluorescence UC spectra were measured in the UC mode. A continuous wave (CW) 975 nm laser was used as the excitation source for the UC measurements. Figure 2.6 presents the emission spectrum of the PMO@UCNP water suspension and PMO@UCNP+RBT suspension when 20 μL RBT (0.01 M) methanol solution was added. Three emission peaks can be observed at 522, 540, and 653 nm, which are ascribed to the $^4\text{H}_{11/2} \rightarrow ^4\text{I}_{15/2}$, $^4\text{S}_{3/2} \rightarrow ^4\text{I}_{15/2}$, and $^4\text{F}_{9/2} \rightarrow ^4\text{I}_{15/2}$ transitions of Er^{3+} , respectively.⁷⁷ Besides, it also shows a reduced intensity of the peak around 540 nm. Although in Figure 2.5. RBT has a minor absorption around 540 nm, it is still capable

of quenching the green emission. Then, the selectivity of UCNPs+RBT to the various ions in the UC mode was examined. 14 different cation solutions (10 ppm) were injected into the cuvette containing LnHPMO@UCNP+RBT suspension under identical conditions, and the UC fluorescence emission spectra (green emission) and intensities are presented in Figure 2.7. UCNPs+RBT in the UC mode showed a strong quenching fluorescence response to Hg^{2+} , similarly to the DS mode, which is a "turn off" effect for emission (Figure 2.7a). In addition, UC fluorescence spectra of UCNPs+RBT with varied ions before and after treatment by Hg^{2+} are presented in Figure 2.7b. The column chart shows the luminescence intensity of the $^4\text{S}_{3/2}\text{-}^4\text{I}_{15/2}$ transition (at 540 nm). Overall, these results indicate the selectivity of UCNP+RBT probe in UC mode to Hg^{2+} out of other different metal ions.

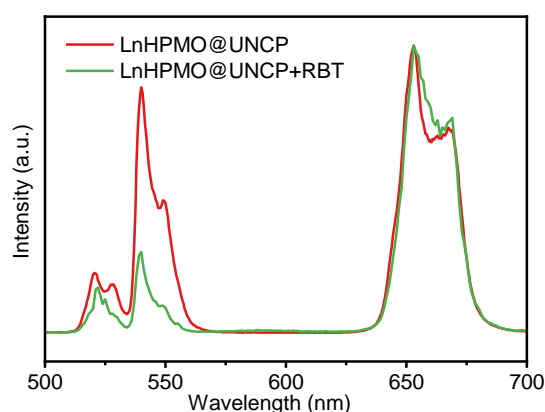


Figure 2.6 UC luminescence spectrum of LnHPMO@UCNP and LnHPMO@UCNP+RBT in water when excited at 975 nm.

The fluorescence titration method was used to investigate the sensitivity and detection range of the UCNPs+RBT probe to Hg^{2+} , and the emission fluorescence intensity of the UCNPs+RBT probe was sensitive to Hg^{2+} concentrations in the range 0-10 μM in the UC mode (Figure 2.7c). Following the addition of Hg^{2+} ions, highly efficient luminescent quenching of UCNPs+RBT was recorded (Figure 2.7c). The relative luminescence intensity of a colloidal suspension demonstrates strong linearity ($R^2= 0.999$), with a detection limit of 296 nM (Figure 2.7d).

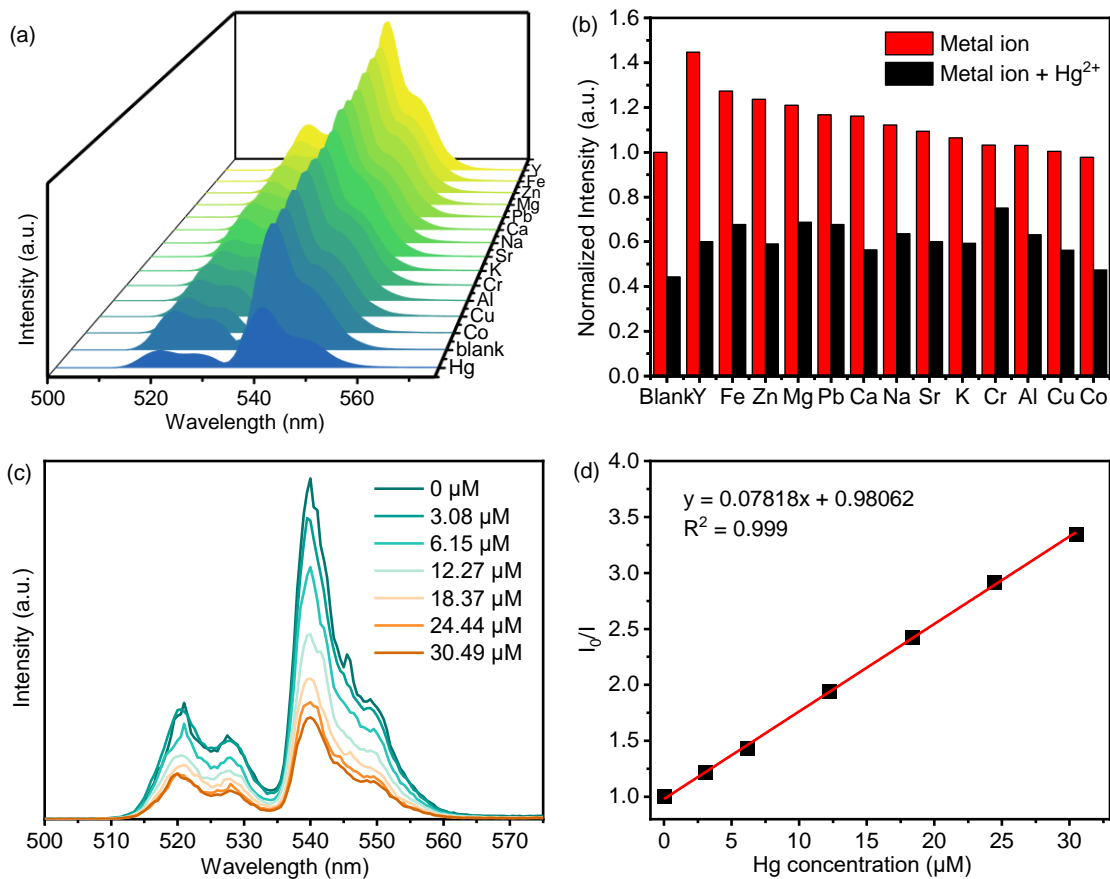


Figure 2.7 (a) Green emission spectra of the colloidal suspensions of LnPMPMO@UCNP+RBT in the presence of different metal ions when excited at 975 nm; (b) Comparison of the luminescence intensities (540 nm) of LnPMPMO@UCNP+RBT with varied ions before and after treatment by Hg^{2+} ; (c) Luminescence spectra of LnPMPMO@UCNP+RBT under different concentrations of Hg^{2+} aqueous solutions; (d) Plot of the Stern-Volmer curve between the luminescence intensity and Hg^{2+} concentration in an aqueous solution.

2.3.4 Revalidation of the DS mode: sensing performance of LnPMPMO@UCNP

To validate the DS mode still functions after the introduction of UCNP, we performed the PL measurements for LnPMPMO@UCNP as the whole system with UV light excitation. As shown in the Figure 2.8, the sensor still has the sensibility of Hg^{2+} as well as the limit of detection has retained (13 μM) with higher detection range (350 μM), despite its attenuation of luminescence intensity.

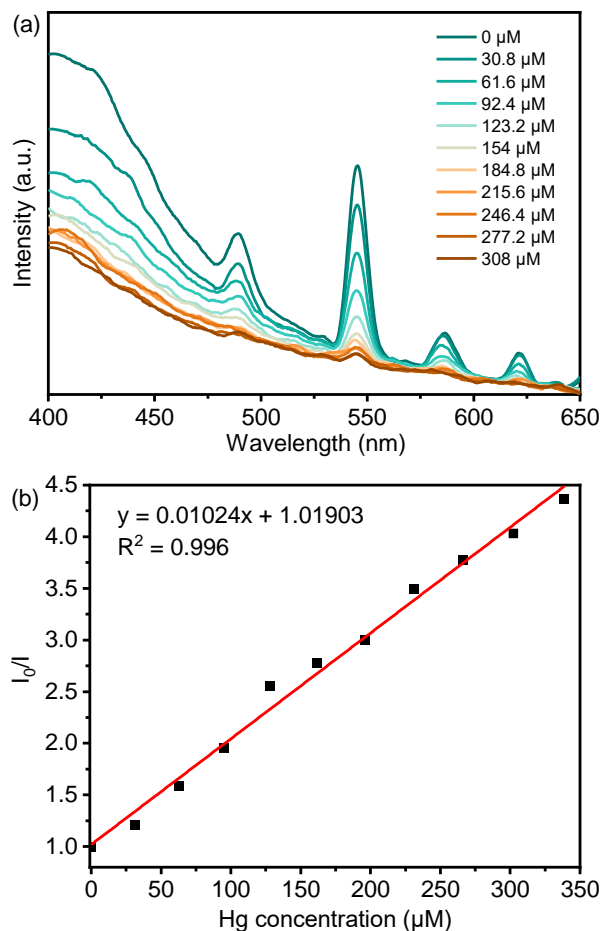


Figure 2.8 (a) Luminescence spectra of LnHPMO@UCNP under different concentrations of Hg^{2+} aqueous solutions; (b) Plot of the Stern-Volmer curve between the luminescence intensity and Hg^{2+} concentration in an aqueous solution.

Together these results provide important insights that the LnHPMO@UCNP probe exhibits superior DS and UC fluorescence responses to Hg^{2+} among cations (Scheme 2.1). When comparing the advantages of the DS and UC modes, the DS mode probe has a ten times higher ion detection range than the UC mode probe, while the UC mode probe has higher sensitivity than the DS mode, which is due to their dissimilar quenching mechanism. Apart from the advantages of our mercury sensor, further studies need to be carried out in order to validate the relationship between quantum yield and sensor performance. For instance, referring to the paper, we chose the precursor ratio of upconversion nanophosphor $\text{NaYF}_4:\text{Yb,Er}$ as 15 mol% of Yb, 5 mol% of Er, but more recent research reported that 18% Yb and

2%Er or 20%Yb and 2%Er are tested to show the more effective UCNP for green emission.⁷⁸

2.4 Conclusions

The presented research examined the sensing performance of diureidobenzoic acid-functionalized hollow PMOs grafted with a Tb³⁺ complex. The hollow PMO acts simultaneously as an organic/inorganic hybrid host and a co-sensitizer for Tb³⁺ ions for the use as a chemical sensor. In addition, we designed a novel dual-mode ion probe to Hg²⁺ with a wide detection range. We can switch upconversion/downshifting fluorescence by introducing lanthanide-doped fluorides into hollow LnPMOs. The UC and DS measurement modes possess different detection ranges and sensitivities through two luminescent modes. Hence, this dual-mode chemical sensor can integrate the advantages of wide detection range and high sensitivity for multiple application scenarios. These results demonstrate that LnPMOs have the potential to act as materials for “turn-off” fluorescence chemical sensors. Additionally, this yolk-shell structure allows multifunctional sensing without compromising the sensitivity or the detection range.

2.5 Supporting information

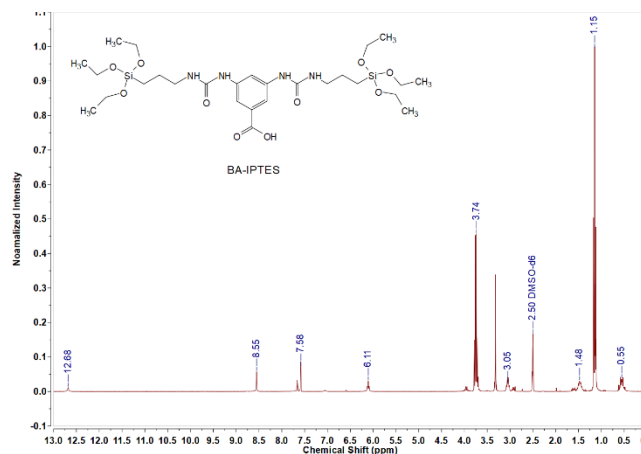


Figure S2.1. ^1H NMR of 3,5-bis(3-(triethoxysilyl)propyl)ureido)benzoic acid (BA-Si)

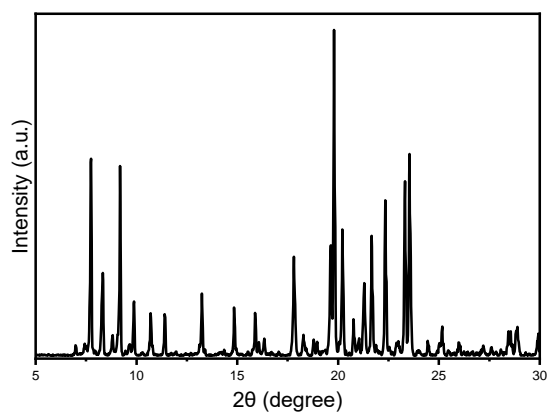


Figure S2.2 XRD pattern of $\text{Tb}(\text{hfac})_3 \cdot n(\text{H}_2\text{O})$

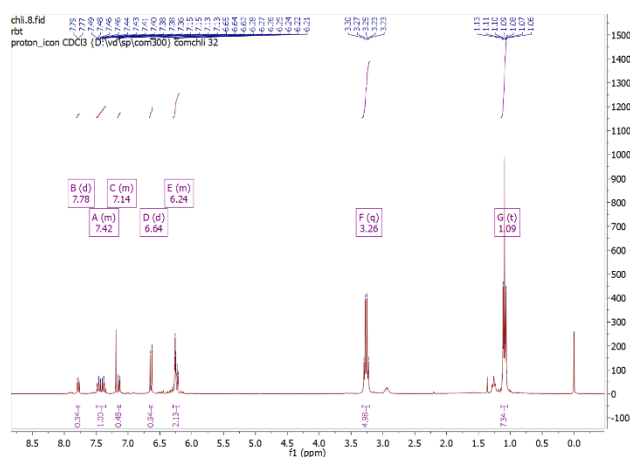


Figure S2.3 ^1H NMR of rhodamine B thiolactone (RBT)

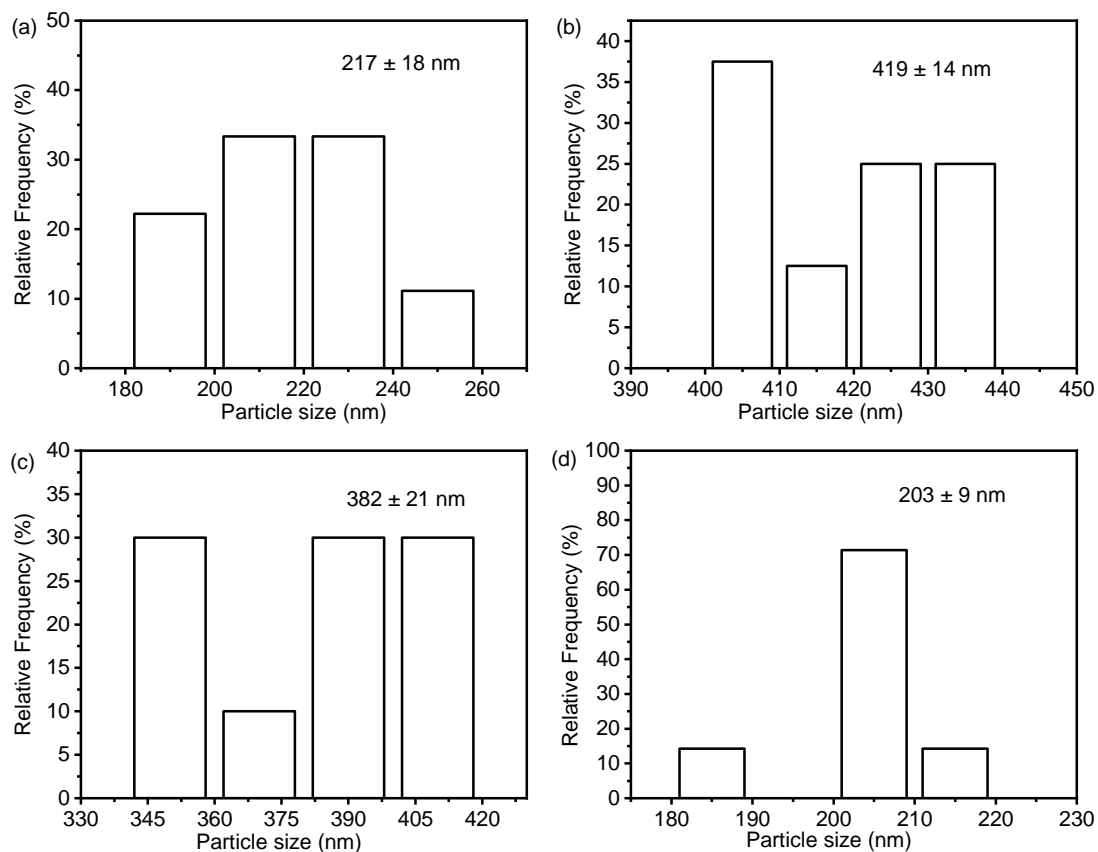


Figure S2.4 Histograms showing the particle size distribution of : (a) SiO_2 nanoparticles; (b) PMO@SiO_2 ; (c) HPMPMO; (d) UCNP.

Table S3.1. Relative metal contents for the samples during synthesis (calcd.) and as determined by XRF.*

Sample	Y^{3+} ion (mol%)		Yb^{3+} ion (mol %)		Er^{3+} ion (mol %)		Si (mol %)		Tb^{3+} ion (mol %)	
	Calcd.	XRF	Calcd.	XRF	Calcd.	XRF	Calcd.	XRF	Calcd.	XRF
LnHPMO@UCNP	80	74	15	24	5	2				
LnHPMO							91	75	9	25

We assume that the concentration ratios are in accordance to the amounts of reagents used. The XRF results are not fully consistent with that, meaning one of the reasons why LnHPMO@UCNP has both the alpha and beta phases of $\text{NaYF}_4:\text{Yb,Er}$ in the XRD pattern is indeed due to the varying percentage of lanthanide ion.

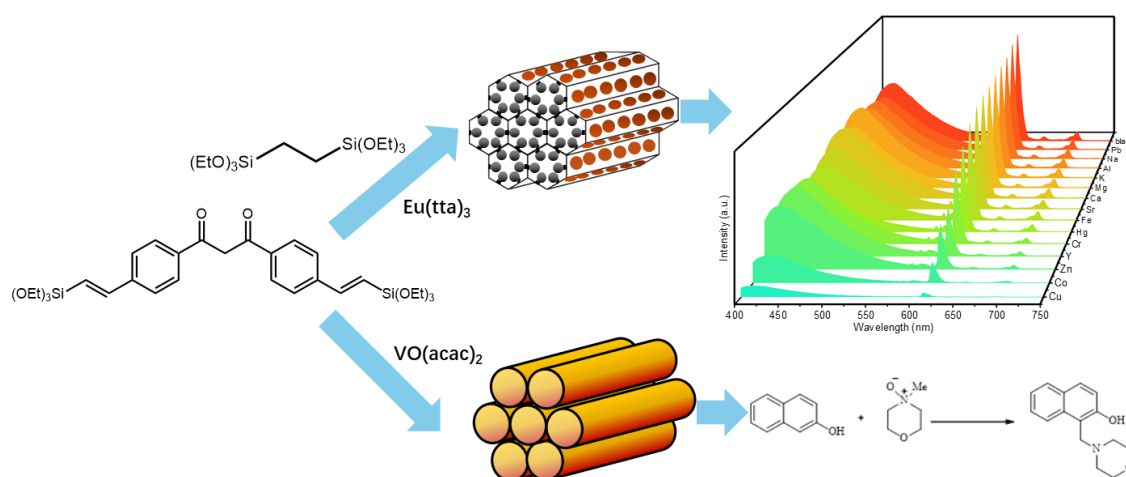
2.6 Reference

1. R. Von Burg, *J Appl Toxicol*, 1995, **15**, 483-493.
2. F. Zahir, S. J. Rizwi, S. K. Haq and R. H. Khan, *Environ. Toxicol. Pharmacol.*, 2005, **20**, 351-360.
3. H. Erxleben and J. Ruzicka, *Anal Chem*, 2005, **77**, 5124-5128.
4. F. X. X. Han, W. D. Patterson, Y. J. Xia, B. B. Sridhar and Y. Su, *Water Air Soil Pollut.*, 2006, **170**, 161-171.
5. Y. Valadbeigi, V. Ilbeigi, M. Vahidi, B. Michalczuk, S. Matejczik and M. Tabrizchi, *J Chromatogr A*, 2020, **1634**, 461676.
6. D. Martín-Yerga, M. B. González-García and A. Costa-García, *Talanta*, 2013, **116**, 1091-1104.
7. E. De Canck, L. Lapeire, J. De Clercq, F. Verpoort and P. Van der Voort, *Langmuir*, 2010, **26**, 10076-10083.
8. Y. Gao, E. De Canck, M. Leermakers, W. Baeyens and P. Van Der Voort, *Talanta*, 2011, **87**, 262-267.
9. A. Pankajakshan, D. Kuznetsov and S. Mandal, *Inorg. Chem.*, 2019, **58**, 1377-1381.
10. S. Cotton, *Lanthanides and actinides*, Red Globe Press London, 1991.
11. J.-C. G. Bünzli and C. Piguet, *Chem. Soc. Rev.*, 2005, **34**, 1048-1077.
12. K. Binnemans, *Chem. Rev.*, 2009, **109**, 4283-4374.
13. M. L. Reddy and S. Sivakumar, *Dalton Trans*, 2013, **42**, 2663-2678.
14. M. Latva, H. Takalo, V.-M. Mikkala, C. Matachescu, J. C. Rodríguez-Ubis and J. Kankare, *J. Lumin.*, 1997, **75**, 149-169.
15. B. Alpha, R. Ballardini, V. Balzani, J. M. Lehn, S. Perathoner and N. Sabbatini, *Photochem. Photobiol.*, 1990, **52**, 299-306.
16. X. Wang, H. Chang, J. Xie, B. Zhao, B. Liu, S. Xu, W. Pei, N. Ren, L. Huang and W. Huang, *Coord Chem Rev*, 2014, **273**, 201-212.
17. H. Tan, Q. Li, C. Ma, Y. Song, F. Xu, S. Chen and L. Wang, *Biosens Bioelectron*, 2015, **63**, 566-571.
18. Z. Y. Gan, X. T. Hu, X. W. Huang, Z. H. Li, X. B. Zou, J. Y. Shi, W. Zhang, Y. X. Li and Y. W. Xu, *Sens. Actuators B Chem.*, 2021, **328**, 128997.
19. X. Wang, Z. Jiang, C. Yang, S. Zhen, C. Huang and Y. Li, *J Hazard Mater*, 2022, **423**, 126978.
20. Y. Shu, Q. Y. Ye, T. Dai, J. Guan, Z. P. Ji, Q. Xu and X. Y. Hu, *J. Hazard. Mater.*, 2022, **430**, 128360.
21. Z. Xiaoxiong, Z. Wenjun, L. Cuiliu, Q. Xiaohong and Z. Chengyu, *Inorg. Chem.*, 2019, **58**, 3910-3915.
22. H. Wang, X. Wang, M. Liang, G. Chen, R.-M. Kong, L. Xia and F. Qu, *Anal. Chem.*, 2020, **92**, 3366-3372.
23. N. W. H. Guo, L. P. Peng, Y. Chen, Y. S. Liu, C. L. Li, H. Zhang and W. Yang, *Talanta*, 2022, **250**, 123710.
24. L. Yu, Y. Chen, H. Lin, W. Du, H. Chen and J. Shi, *Biomaterials*, 2018, **161**, 292-305.
25. Q. H. Yang, J. Liu, L. Zhang and C. Li, *J. Mater. Chem.*, 2009, **19**, 1945-1955.
26. L.-N. Sun, H.-J. Zhang, C.-Y. Peng, J.-B. Yu, Q.-G. Meng, L.-S. Fu, F.-Y. Liu and X.-M. Guo, *J. Phys. Chem. B*, 2006, **110**, 7249-7258.
27. A. M. Kaczmarek and P. Van Der Voort, *Materials*, 2020, **13**, 566.
28. A. M. Kaczmarek, R. Van Deun and P. Van Der Voort, *J Mater Chem C*, 2019, **7**, 4222-4229.
29. L. Sun, W. Mai, S. Dang, Y. Qiu, W. Deng, L. Shi, W. Yan and H. Zhang, *J. Mater. Chem.*, 2012, **22**, 5121-5127.
30. Y. Li, B. Yan and Y.-J. Li, *Microporous Mesoporous Mater*, 2010, **132**, 87-93.
31. N. Yuan, Y. Liang, E. S. Erichsen and R. Anwender, *RSC Advances*, 2015, **5**, 83368-83376.
32. H. Li, Y. Li, Z. Zhang, X. Pang and X. Yu, *Materials & Design*, 2019, **172**.
33. A. M. Kaczmarek and P. Van Der Voort, *J Mater Chem C*, 2019, **7**, 8109-8119.
34. A. M. Kaczmarek, S. Abednatanzi, D. Esquivel, C. Krishnaraj, H. S. Jena, G. Wang, K. Leus, R. Van Deun, F. J. Romero-Salguero and P. Van Der Voort, *Microporous Mesoporous Mater.*, 2020, **291**, 109687-109688.
35. W. Liu, A. M. Kaczmarek, H. Rijckaert, P. Van Der Voort and R. Van Deun, *Dalton Trans*, 2021, **50**, 11061-11070.
36. W. Liu, A. M. Kaczmarek, P. Van Der Voort and R. Van Deun, *Dalton Trans.*, 2022, **51**, 11467-11475.

37. X. Guo, H. Guo, L. Fu, H. Zhang, R. Deng, L. Sun, J. Feng and S. Dang, *Microporous Mesoporous Mater*, 2009, **119**, 252-258.
38. J. Yao, C. Huang, C. Liu and M. Yang, *Talanta*, 2020, **208**, 120157.
39. J. Liu, A. M. Kaczmarek and R. Van Deun, *Sens. Actuators B Chem.*, 2018, **255**, 2163-2169.
40. A. M. Kaczmarek, M. Suta, H. Rijckaert, A. Abalymov, I. Van Driessche, A. G. Skirtach, A. Meijerink and P. Van Der Voort, *Adv. Funct. Mater.*, 2020, **30**, 2003101.
41. W. Liu, A. M. Kaczmarek, P. Van Der Voort and R. Van Deun, *J. Chem. Soc., Dalton trans.*, 2022, **51**, 11467-11475.
42. Q. Liu, W. Feng, T. Yang, T. Yi and F. Li, *Nat. Protoc.*, 2013, **8**, 2033-2044.
43. Y. Dai, H. Xiao, J. Liu, Q. Yuan, P. a. Ma, D. Yang, C. Li, Z. Cheng, Z. Hou and P. Yang, *J. Am. Chem. Soc.*, 2013, **135**, 18920-18929.
44. H. Li and L. Wang, *Analyst*, 2013, **138**, 1589-1595.
45. W. Shi and H. Ma, *Chem Commun (Camb)*, 2008, DOI: 10.1039/b717718f, 1856-1858.
46. H. Li and L. Wang, *Analyst*, 2013, **138**, 1589-1595.
47. Q. Liu, J. Peng, L. Sun and F. Li, *ACS nano*, 2011, **5**, 8040-8048.
48. J.-C. Boyer and F. C. Van Veggel, *Nanoscale*, 2010, **2**, 1417-1419.
49. B. Guan, Y. Cui, Z. Ren, Z.-a. Qiao, L. Wang, Y. Liu and Q. Huo, *Nanoscale*, 2012, **4**, 6588-6596.
50. S. Lu, D. Tu, X. Li, R. Li and X. Chen, *Nano Research*, 2016, **9**, 187-197.
51. J. Liu, H. Rijckaert, M. Zeng, K. Haustaete, B. Laforce, L. Vincze, I. Van Driessche, A. M. Kaczmarek and R. Van Deun, *Adv. Funct. Mater.*, 2018, **28**, 1707365.
52. J. Sun, H. Rijckaert, Y. Maegawa, S. Inagaki, P. Van Der Voort and A. M. Kaczmarek, *Chem. Mater.*, 2022, **34**, 3770-3780.
53. S. Haffer, M. Tiemann and M. Fröba, *Chem. Eur. J.*, 2010, **16**, 10447-10452.
54. M. F. Richardson, W. F. Wagner and D. E. Sands, *J. Inorg. Nucl. Chem.*, 1968, **30**, 1275-1289.
55. D. Y. Chappidi, M. N. Gordon, H. M. Ashberry, J. Huang, B. M. Labedis, R. E. Cooper, B. J. Cooper, V. Carta, S. E. Skrabalak and K. R. Dunbar, *Inorg. Chem.*, 2022, **61**, 12197-12206.
56. M. Deng, Y. Ma, S. Huang, G. Hu and L. Wang, *Nano Res.*, 2011, **4**, 685-694.
57. W. Shi and H. Ma, *Chem. Commun.*, 2008, 1856-1858.
58. H. Li, X. Shi, X. Li and L. Zong, *Opt. Mater.*, 2020, **108**, 110144.
59. D. Liu, L. T. Tufa and J. Lee, *Electrochim. Acta*, 2019, **313**, 389-396.
60. J. Chen, J. Wan, Y. Gong, K. Xu, H. Zhang, L. Chen, J. Liu and C. Liu, *Chemosphere*, 2021, **270**, 128661.
61. A. M. Kaczmarek, Y. Y. Liu, M. K. Kaczmarek, H. Liu, F. Artizzu, L. D. Carlos and P. Van Der Voort, *Angew. Chem.*, 2020, **132**, 1948-1956.
62. R. K. Bauer, R. Borenstein, P. De Mayo, K. Okada, M. Rafalska, W. R. Ware and K. C. Wu, *J. Am. Chem. Soc.*, 1982, **104**, 4635-4644.
63. T. Fujii, K. Kodaira, O. Kawauchi, N. Tanaka, H. Yamashita and M. Anpo, *J. Phys. Chem. B*, 1997, **101**, 10631-10637.
64. J. Lin, Q. Cheng, J. Zhou, X. Lin, R. C. K. Reddy, T. Yang and G. Zhang, *J. Solid State Chem.*, 2019, **270**, 339-345.
65. F. Zu, F. Yan, Z. Bai, J. Xu, Y. Wang, Y. Huang and X. Zhou, *Microchimica Acta*, 2017, **184**, 1899-1914.
66. E. M. Nolan and S. J. Lippard, *Chem. Rev.*, 2008, **108**, 3443-3480.
67. H. Li, Y. Li, Z. Zhang, X. Pang and X. Yu, *Materials & Design*, 2019, **172**, 107712.
68. G. Ji, J. Liu, X. Gao, W. Sun, J. Wang, S. Zhao and Z. Liu, *J. Mater. Chem. A*, 2017, **5**, 10200-10205.
69. J.-J. Huang, J.-H. Yu, F.-Q. Bai and J.-Q. Xu, *Cryst. Growth Des.*, 2018, **18**, 5353-5364.
70. Z. Sun, Y. Li, Y. Ma and L. Li, *Dyes Pigm.*, 2017, **146**, 263-271.
71. D. A. Armbruster and T. Pry, *Clin Biochem Rev*, 2008, **29**, S49.
72. M. E. Zorn, R. D. Gibbons and W. C. Sonzogni, *Anal. Chem.*, 1997, **69**, 3069-3075.

73. S. Yoon, E. W. Miller, Q. He, P. H. Do and C. J. Chang, *Angew. Chem.*, 2007, **119**, 6778-6781.
74. Y. M. Zhu, C. H. Zeng, T. S. Chu, H. M. Wang, Y. Y. Yang, Y. X. Tong, C. Y. Su and W. T. Wong, *J. Mater. Chem. A*, 2013, **1**, 11312-11319.
75. H. N. Kim, W. X. Ren, J. S. Kim and J. Yoon, *Chem. Soc. Rev.*, 2012, **41**, 3210-3244.
76. F. Wang and X. Liu, *Chem. Soc. Rev.*, 2009, **38**, 976-989.
77. A. M. Kaczmarek, M. Suta, H. Rijckaert, T. P. van Swieten, I. Van Driessche, M. K. Kaczmarek and A. Meijerink, *J Mater Chem C*, 2021, **9**, 3589-3600.
78. C. Homann, L. Krukewitt, F. Frenzel, B. Grauel, C. Würth, U. Resch-Genger and M. Haase, *Angew. Chem. Int. Ed.*, 2018, **57**, 8765-8769.

Chapter 3. Acetylacetonate Functionalized Periodic Mesoporous Organosilicas: from Sensing to Catalysis



The results of this chapter were published in: Acetylacetonate Functionalized Periodic Mesoporous Organosilicas: from Sensing to Catalysis. **Chunhui Liu**, Mahdiah Haghighat, Himanshu Sekhar Jena, Dirk Poelman, Nathalie De Geyter, Rino Morent, Anna M. Kaczmarek, and Pascal Van Der Voort, 2024, submitted to Journal of Materials Chemistry A.

Abstract

Periodic mesoporous organosilicas (PMOs) have emerged as versatile sensors due to their stability, low toxicity, and scalability. This study reports for the first time on the embedding the acetylacetonate (acac) group into the PMO backbone. This integration of acac into the PMO framework opens new applications in both sensing and catalysis. The Eu^{3+} grafted acac-PMOs demonstrate enhanced sensitivity, with a detection limit of 108 nM, and high selectivity in aqueous copper (Cu^{2+}) ion sensing. Additionally, these novel PMOs show high catalytic efficiency in Mannich reactions.

3.1 Introduction

Periodic mesoporous organosilicas (PMOs) have emerged as a promising and appealing sensor system due to their stable physicochemical properties, low toxicity, high biocompatibility, and facile scalability for large-scale production.¹ PMOs were initially reported in 1999 by Ozin,² Stein,³ and Inagaki.⁴ Unlike other porous materials such as MCM (Mobil Composition of Matter)⁵ and SBA (Santa Barbara Amorphous materials),⁶ PMOs offer the unique advantage of incorporating desired organic functionalities directly into the silsesquioxane framework. This is achieved by utilizing organically bridged silica precursors, where hydrolysable groups (OR) in the bis-silane $(RO)_3\text{-Si-R}_f\text{-Si-(RO)}_3$ are connected to the desired organic functionalities (R_f). The incorporation of these organic groups within the PMO structure enhances the material's hydrophobicity and hydrothermal stability, while also minimizing leaching issues commonly associated with externally grafted functionalities.^{7, 8} Additionally, PMOs possess ordered mesopores and high surface areas (up to 2370 m²/g),⁹ making them suitable for a wide range of applications such as catalysis, adsorption, chromatography, low-k materials, drug release, and sensors.¹⁰⁻¹³ The tailored organic functionalities within the PMO framework enable the design of materials with specific properties and functionalities, allowing for enhanced performance in various applications. The ability to finely tune the pore size, surface chemistry, and hydrophobicity of PMOs provides versatility and control over their performance in different environments.

Acetylacetonone (acac) based homogeneous transition metal complexes have demonstrated exceptional catalytic efficacy across a variety of organic transformations.¹⁴⁻¹⁶ Significantly, a limited number of acetylacetonone-functionalized heterogeneous systems, such as silicas and covalent triazine frameworks (CTFs), have demonstrated high reactivity and recyclability after

grafting transition metal (post-synthetic functionalization) in various chemical processes. These processes include cross-coupling reactions, hydroxylation, click chemistry, Glaser-type coupling, and the oxidation of alcohols.¹⁷⁻²² The immobilization of acac ligands within the framework not only enhances catalytic activity but also provides a stable and recyclable catalytic system, thereby addressing the challenges associated with traditional acac complexes.¹⁷ So far, a PMO with acac functionalities embedded in the backbone has not been reported. Zhao et al. grafted the VO(acac)₂ onto PMOs to create a catalyst for selective hydroxylation of benzene to phenol.²⁰ The organic precursor was synthesized through the Schiff base condensation between the amino group of 3-aminopropyl-triethoxysilane (APTES) and the carbonyl unit of VO(acac)₂. We aimed to functionalize acac group into a PMO backbone in order to design a robust acac-PMO supported transition metal catalyst for sustainable catalysis.

Next to catalysis where the acac groups are typically tethering transition metal ions, also lanthanides anchor firmly to the acac ligands, creating possibly luminescent sensors. Embedded organic groups within the PMO framework act as efficient energy transfer antennas, sensitizing trivalent lanthanide ions (Ln³⁺) and promoting luminescence.^{13,23, 24} The potential applications of such sensors span environmental monitoring, biological analysis, and other areas demanding accurate metal ion detection.²⁵ Despite this potential, research on lanthanide-based PMOs (LnPMOs) as chemical sensors remains limited, with only a few studies published in the late 2010s.^{24, 26-30} Among these, Eu-based materials have attracted significant attention for their potential in detecting copper ions (Cu²⁺). Eu-based materials exhibit strong initial fluorescence that undergoes significant quenching upon interaction with Cu ions, offering a highly sensitive and selective detection method for Cu in aqueous solutions.^{31, 32}

This work presents a novel approach to luminescence ion sensing and catalysis using acac-functionalized PMOs. We developed a new acac-bridged bisilane precursor (acac-Si) and successfully synthesized acac-PMOs capable of grafting metal complexes. The Eu^{3+} -grafted acac-PMO demonstrates potential for ion sensing applications, whereas the vanadyl (VO^{2+}) grafted acac-PMO exhibits catalytic activity in a Mannich-type reaction as a model reaction. These studies contribute to the ongoing development of PMOs for sensing and catalysis.

3.2 Experimental

3.2.1 Materials and Instrumentation

All chemicals were purchased from Sigma Aldrich, Fluorochem, Alfa Aesar, or TCI Europe and used without further purification.

Nitrogen adsorption experiments were conducted at $-196\text{ }^{\circ}\text{C}$ using a TriStar II gas analyzer. Prior to analysis, the samples underwent vacuum degassing at $120\text{ }^{\circ}\text{C}$ for 24 h. Powder X-ray diffraction (PXRD) patterns were obtained using a Bruker D8 Advance diffractometer equipped with an autochanger and LynxEye XE-T Silicon Strip Line detector, operating at 40 kV and 30 mA with $\text{Cu-K}\alpha$ radiation ($\lambda = 1.5406\text{ \AA}$) in Bragg-Brentano geometry. Fourier transform infrared spectroscopy (FT-IR) measurements were performed using a Thermo Nicolet 6700 FT-IR spectrometer equipped with a nitrogen-cooled MCT-A (mercury–cadmium–tellurium) detector and a KBr beam splitter. X-ray fluorescence (XRF) was measured by XRF Supermini200 Rigaku to analyze the relative metal contents. Transmission electron microscopy (TEM) images were acquired using a JEOL JEM-2200FS transmission electron microscope with a post-sample Cs corrector and an accelerating voltage of 200 kV. Using V_2O_5 as a catalyst, elemental analysis (CHNS) was finished using the Thermo Flash 2000 elemental analyzer. X-ray photoelectron spectroscopy (XPS) measurements were carried out on a PHI 5000 VersaProbe II spectrometer equipped

with a monochromatic Al-K α X-ray source ($h\nu = 1486.6$ eV). Photoluminescence measurements were conducted using an Edinburgh Instruments FLSP920 UV-vis-NIR spectrometer setup. The emission signals were detected using a Hamamatsu R928P photomultiplier tube, and a monochromated 450 W xenon lamp was employed as the steady-state excitation source. Luminescence decay profiles were measured using a 60 W pulsed xenon lamp.

3.2.2 Synthesis

3.2.2.1 1,3-bis(4-bromophenyl)propane-1,3-dione (acac-Br)

Acac-Br was synthesized according to a previously reported procedure.¹⁷ A total of 1.66 g (41.51 mmol) of NaH (60% in mineral oil) was dispersed in 50 mL of anhydrous tetrahydrofuran (THF) under an argon atmosphere and stirred for 30 minutes. The resulting heterogeneous mixture was then transferred to an ice bath, and 2.73 g (13.7 mmol) of solid 4'-bromoacetophenone was added. Once the mixture turned dark red, a solution of methyl 4-bromobenzoate (3.23 g, 15.03 mmol) in anhydrous THF (10 mL) was added dropwise over 30 minutes under an argon atmosphere. The entire mixture was stirred for 1 hour in the ice bath and then for an additional 1 hour at room temperature. The mixture was refluxed for 24 hours under an argon atmosphere, and then quenched with ice. The pH of the reaction mixture was adjusted to neutral by slowly adding 1 N HCl, and the linker was recovered by filtration and washed with distilled H₂O. The resulting sticky dark brown solids were washed with hot ethanol multiple times to obtain the pure linker as a brown solid. Yield: 86%; ¹H NMR (400 MHz, DMSO-d₆) δ 8.14 – 8.09 (m, 4H), 7.81 – 7.76 (m, 4H), 7.38 (s, 1H). ¹³C NMR (126 MHz, DMSO-d₆) δ 179.27 , 132.10 , 126.91 , 124.62 , 122.13 , 89.13 . FT-IR spectrum is shown in Figure S3.1.

3.2.2.2 1,3-bis(4-((E)-2-(triethoxysilyl)vinyl)phenyl)propane-1,3-dione (acac-Si)

Acac-Si was synthesized via a coupling reaction between **Acac-Br** and vinyltriethoxysilane using Heck reaction conditions. In a two-necked flask under argon, **acac-Br** (1 g, 2.6 mmol), palladium acetate (5.61 mg, 0.025 mmol), and P(o-CH₃C₆H₄)₃ (45.7 mg, 0.15 mmol) were combined with freshly distilled DMF (50 mL), triethylamine (2.2 mL, 15.75 mmol), and triethoxyvinylsilane (1.3 mL, 6.25 mmol). The resulting mixture was heated to 100 °C and stirred for 18 hours. After cooling to room temperature and filtration, the solvents were removed, and the remaining heterogeneous residue was dissolved in diethyl ether. Filtration and solvent evaporation yielded the product as a highly viscous orange oil. Yield: 95%; ¹H NMR (400 MHz, DMSO-d₆) δ 8.23 – 8.17 (m, 4H), 7.79 – 7.74 (m, 4H), 7.22 (d, J = 19.3 Hz, 2H), 6.52 – 6.43 (m, 2H), 3.83 (q, J = 7.0 Hz, 12H), 3.79 (s, 1H), 1.25 – 1.12 (m, 18H). ¹³C NMR (126 MHz, DMSO-d₆) δ 166.55 , 136.77 , 131.64 , 131.24 , 129.67 , 126.82 , 93.43, 57.83 , 18.08. FT-IR spectrum is shown in Figure S3.1.

3.2.2.3 Synthesis of mesoporous Acetylacetonate-PMO (acac-PMO)

Following a modified literature procedure,³³ the synthesis of acac-Si involved a two-step sol-gel reaction. In a 20 ml round bottom flask, cetyl trimethyl-ammonium bromide (CTAB, 0.96 mmol, 350 mg) was dissolved in a solution containing 5.83 g of water. After adding 3.63 mL of NH₄OH solution (25%), the mixture was stirred at 80 °C for 30 minutes. In a separate vial, acac-Si was mixed with bis(triethoxysilyl)ethane (BTESE) in two 0%:100% and 20%:80% ratios, respectively, along with 1 mL of ethanol. The precursor solution was then injected promptly into the stirred aqueous surfactant solution, resulting in the formation of a yellow suspension. The mixture was stirred for an additional 24 h at 80 °C. After cooling down and filtration, the solid material was rinsed repeatedly with deionized water and ethanol, followed by drying at 120 °C. To remove the surfactant, a solvent-

extraction method was employed with the following procedure: Approximately 1 g of the synthesized material was stirred in a solution of 200 ml of ethanol and 3 ml of concentrated hydrochloric acid at 80 °C for 4 hours. This extraction process was repeated twice to ensure the complete removal of all surfactants from the material. Finally, the sample was dried overnight in an oven at 120 °C. The obtained products were denoted as acac(20)-PMO and acac(100)-PMO, for which the molar ratio of acac-Si to BTESE were 20 : 80 and 100: 0, respectively.

3.2.2.4 Synthesis of the Eu(III) complex [Eu(tta)₃(H₂O)₂]

Eu(tta)₃(H₂O)₂ was synthesized according to a previously reported procedure.³⁴ 2-Thenoyltrifluoroacetone (tta, 1.33 g, 6 mmol) was dissolved in 30 mL of ethanol. Sequentially, NaOH (1 N, 6 mL) and a solution of EuCl₃·6H₂O (0.73 g, 2 mmol) in 10 mL of water were added to the 2-thenoyltrifluoroacetone solution. Additional water (200 mL) was added, and the mixture was heated to 60 °C for a brief duration. Upon cooling to room temperature, the complex precipitated. The precipitate was separated by filtration, washed with water, and subsequently dried under vacuum. The yield was 85%, and the complex was found to be a dihydrate. Elemental analysis: calculated for Eu₁O₆C₂₄H₁₂F₉S₃: C, 35.35%; H, 1.48%; S, 11.80%. Found C, 34.24%; H, 1.31%; S, 11.57%. IR (KBr, cm⁻¹): 1608 (C=O stretch).

3.2.2.5 Synthesis of Eu grafted Acetylacetonate-PMO (acac-PMO@Eu_tta)

The materials were synthesized in Pyrex test tubes using a heating block. To 20 mg of the acac(20)-PMO, a 10 times molar amount of the pre-synthesized Eu(tta)₃ complex was added. The suspension was subjected to ultrasound for 15 minutes after adding 10 mL of methanol. The Pyrex tubes were then carefully sealed and placed on a heating block at 80 °C for 24 hours. Afterward, the product was allowed

to cool to ambient temperature, followed by centrifugation (6000 rpm, 4 min) and two washes with methanol. Finally, the material was dried overnight in an oven at 80 °C.

3.2.2.6 Synthesis of V grafted Acetylacetonate-PMO (acac-PMO@VO_acac)

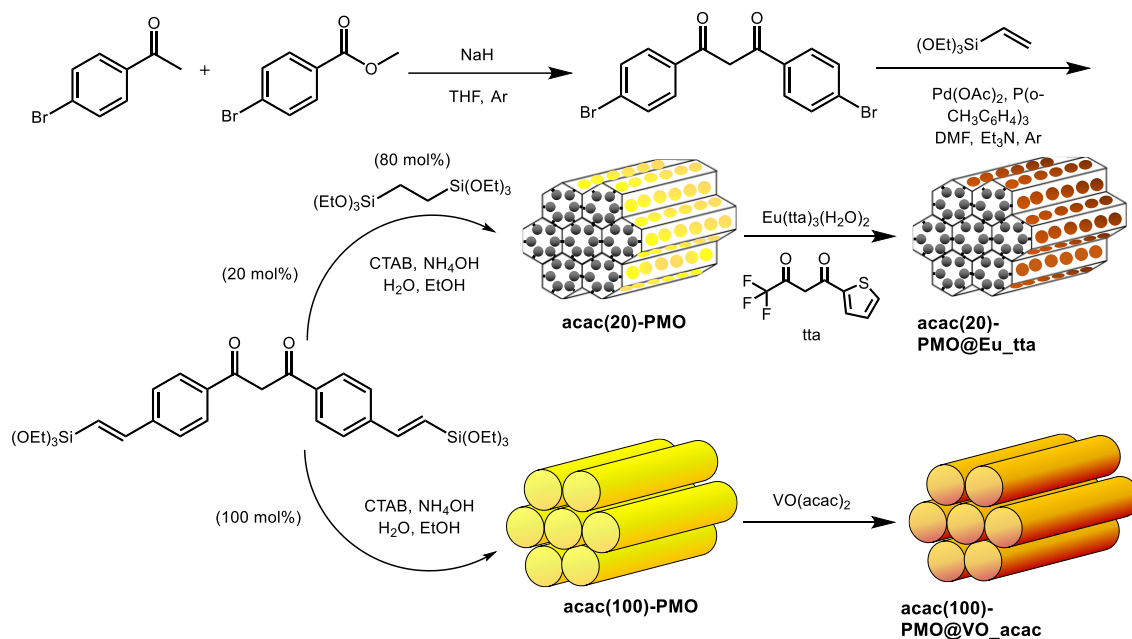
The acac-PMO@VO_acac catalyst was prepared using the postsynthetic metalation method, with VO(acac)₂ as the metal source and toluene as the solvent. In a typical procedure,¹⁷ 30 mg (0.11 mmol) of VO(acac)₂ was dissolved in 15 mL of anhydrous toluene, and 120 mg of acac(100)-PMO was added to the solution under argon atmosphere. The mixture was refluxed overnight with stirring, then filtered and dried. To remove weakly bound VO(acac)₂, the catalyst was thoroughly washed using Soxhlet extraction with toluene, followed by filtration and further drying under vacuum. Finally, the catalyst was subjected to vacuum drying at 120 °C for 12 hours to remove any remaining solvent before being used for subsequent experiments. The CHNS analysis of acac-PMO@VO_acac revealed a decrease in the carbon (C) content, providing confirmation of the successful incorporation of VO(acac)₂ into the framework. Elemental analysis: C, 43.18%; H, 4.33%. V loading (0.59 mmol g⁻¹) was studied by XRF on a Rigaku NEX CG with an Al source and the Al-K α peak energy was used as the internal standard.

3.3 Results and discussion

3.3.1 Synthesis and characterization of acac-PMOs

The designed approach for producing specific acac-PMO materials is shown in Scheme 3.1. This method encompasses an initial base-catalyzed condensation between 4'-bromoacetophenone and methyl 4-bromobenzoate.³⁵ Subsequently, a coupling reaction is performed, involving vinyl-triethoxysilane and using Heck reaction conditions. Through the silylation of acac-Br, the resultant structure of

acac-Si is achieved. To create a series of acac-functionalized PMO materials with varying precursor ratios, a combination of acac-Si and bis(triethoxysilyl)ethane (BTESE) is prepared in two distinct ratios: 20 % acac-Si to 80% BTESE, and 100 % acac-Si to 0 % BTESE.



Scheme 3.1 Schematic illustration of the preparation of the acac(20)-PMO@Eu_{tta}, acac(100)-PMO@VO_{acac}.

The generated products are designated as acac(20)-PMO and acac(100)-PMO, wherein the molar ratios of acac-Si to BTESE are 20 : 80 and 100 : 0, respectively. In the design of acac(20)-PMO@Eu_{tta} for copper ion sensing, a 20% acetylacetonate (acac) functionalization is strategically chosen to address aggregation-caused quenching (ACQ). This lower acac content ensures an optimal dispersion of Eu³⁺ complexes within the mesoporous framework, maintaining their luminescent efficiency vital for sensitive and accurate copper detection. The tailored PMO structure facilitates effective interaction with copper ions while preserving the unique luminescent properties of Eu, overcoming the common challenge of luminescence quenching in aggregated lanthanide materials.³⁶

The successful coupling was validated through FT-IR measurements. In Figure 3.1a and 3.1d, we present a spectral analysis comparing the spectrum of pure acac(100)-PMO with that of acac(20)-PMO, as well as their respective metal-grafted counterparts. In the spectra of acac(20)-PMO and acac(100)-PMO, in addition to observing the characteristic C-H and Si-O-Si stretching vibrations at 2950-2800 cm^{-1} , 1200-1000 cm^{-1} , and 800 cm^{-1} , a distinct and sharp band at 1700 cm^{-1} (-C=O) was detected in both acac(20)-PMO and acac(100)-PMO.^{17, 37} This observation provides clear evidence of the persistence of the acac functional group even after the synthesis of PMO.

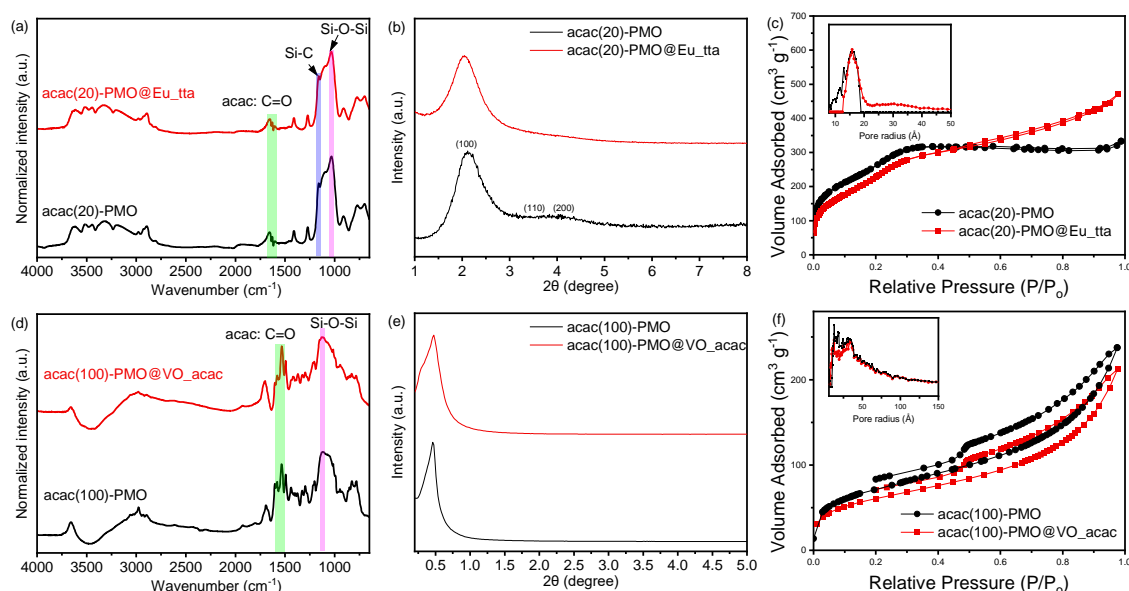


Figure 3.1 FT-IR spectra of (a) acac(20)-PMO and (d) acac(100)-PMO; XRD patterns of (b) acac(20)-PMO and (e) acac(100)-PMO; N₂ adsorption–desorption isotherms and pore size distributions of (c) acac(20)-PMO and (f) acac(100)-PMO.

To investigate the impact of material functionalization on structural characteristics, we conducted powder X-ray diffraction (PXRD) and N₂-sorption analyses. Figure 3.1b displays the X-ray diffraction (XRD) pattern of the acac(20)-PMO within the 2θ range of 1–8°. An intense peak at around 2° with a small shoulder was observed in Figure 3.1b, signifying the presence of hexagonally (or cubic) arranged mesoporous structures.^{38, 39} The XRD pattern of acac(100)-PMO reveals a

distorted structure. The intense XRD peak, assigned to the (100) plane, affirms a substantial reduction in long-range ordering when compared to the co-condensation sample.⁴⁰ The formation of a wormlike pore structure in acac(100)-PMO nanoparticles may be attributed to the reduced solubility of the acetylacetonate-bridged silane, primarily due to the highly hydrophobic benzene moiety, in comparison to the other organosilica source (BTESE) in aqueous media.⁴⁰ In Figures 3.1c and 3.1f, the N₂-sorption isotherms of acac-PMOs are presented. The acac(20)-PMO displays a Type IV isotherm with an H1 hysteresis loop, indicative of a uniform mesoporous structure.^{31, 41}

Conversely, the acac(100)-PMO shows a Type IV isotherm with an H2(b)-shaped hysteresis loop, suggestive of non-uniform mesopores that are blocked for the desorption (cavitation).^{42, 43} Table 3.1 summarizes the Brunauer–Emmett–Teller surface area (S_{BET}), total pore volume at $P/P^0 = 0.95$ (V), and non-local density functional theory most prominent pore diameter (d_{NLDFT}). It is clear from the XR diffractograms, the Table 3.1 and the isotherms that the acac(20)-PMO, formed from 80% BTESE and only 20% acac-precursor forms the typical (expected) hexagonal structure (P6mm) whereas the acac(100)-PMO forms a distorted structure with uniform but unordered worm-like pores. The bulky nature of the acac precursor in acac(100)-PMO might hinder the effectiveness of CTAB during synthesis. This could lead to a less-ordered pore structure or larger pores in acac(100)-PMO compared to acac(20)-PMO.

Table 3.1 Physicochemical Properties of samples

Sample	S_{BET} ($\text{m}^2 \text{g}^{-1}$)	V ($\text{cm}^3 \text{g}^{-1}$)	d_{NLDFT} (nm) ^a
acac(20)-PMO	1040	0.47	3.2
acac(20)- PMO@Eu_tta	984	0.46	3.2
acac(100)-PMO	264	0.36	2.6
acac(100)- PMO@VO_acac	220	0.32	2.6

^acalculated from NLDFT, N2 at 77K, using the kernel of silica cylindrical pore, adsorption branch.

3.3.2 Luminescence properties

In the context of luminescence applications, we departed from using Eu^{3+} salts and instead employed Eu^{3+} complexes for grafting into acac(20)-PMO. Therefore, we created a composite material denoted as acac(20)-PMO@Eu_tta. The tta (thenoyltrifluoroacetate) ligand acts as an ancillary ligand that can serve as a secondary antenna ligand. In addition, this ligand can act as a shielding agent, safeguarding the lanthanide ions from quenching by water molecules.⁴⁴

Figure 3.2a presents the excitation-emission spectra of the acac(20)-PMO under ambient conditions. The excitation spectrum displays a broad band spanning from 250 to 400 nm, with the maximum excitation wavelength at 360 nm. The emission spectrum extends from 390 to 600 nm, with the emission peak maximum at 420 nm. The luminescent properties of this hybrid material were further investigated through the grafting of $\text{Eu}(\text{tta})_3$ complexes onto the PMO material. The combined excitation-emission spectra for acac(20)-PMO@Eu_tta are illustrated in Figure 3.2b. The excitation spectrum displays a broad band spanning from 250 to 400 nm with a maximum at $\lambda_{\text{max}} = 352$ nm. This spectral feature can be attributed to

transitions from the ground state (π)S₀ to the excited state (π^*)S₁ of the organic ligands. Conversely, upon excitation at the maximum of the broad band, the emission spectrum exhibits characteristics indicative of intra-4f⁶ transitions of Eu³⁺ ions.⁴⁵ A comprehensive assignment of the emission peaks observed is provided in Table 3.2. When the sample is exposed to UV light (302 nm), it emits a purplish-red color, as seen in the Figure 3.2b inset and the CIE diagram of Figure S3.2a. It consists of contributions from both acac(20)-PMO and Eu³⁺. The luminescence decay time of the sample was assessed by excitation at 352 nm and detection at 611 nm. A satisfactory fit was achieved utilizing a mono-exponential decay curve (Figure 3.2c).

Table 3.2 Assignment of acac(20)-PMO@Eu₃₊ emission peaks.

Wavelength (nm)	Wavenumber (cm ⁻¹)	f-f transition
578	17301	⁵ D ₀ → ⁷ F ₀
591	16920	⁵ D ₀ → ⁷ F ₁
611	16367	⁵ D ₀ → ⁷ F ₂
650	15385	⁵ D ₀ → ⁷ F ₃
699	14306	⁵ D ₀ → ⁷ F ₄

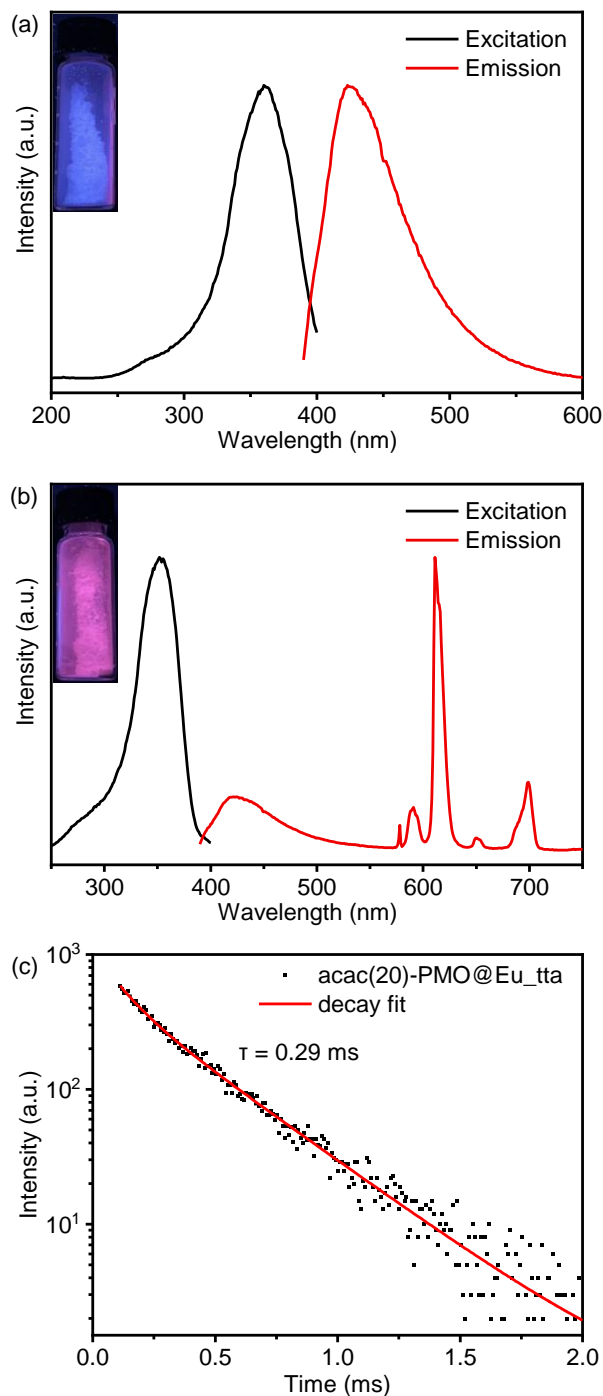


Figure 3.2 (a) Combined RT excitation-emission spectrum of the acac(20)-PMO (excited at 360 nm observed at 420 nm); (b) Combined RT excitation-emission spectrum of the acac(20)-PMO@Eu_tta, ex = 352 nm, em = 611 nm; (c) Luminescence decay profile of as prepared acac(20)-PMO@Eu_tta, ex = 352 nm, em = 611 nm. Measurements refer to the sample in solid form.

The photophysical characteristics of acac(20)-PMO@Eu_tta are primarily ascribed to the f-f transitions of Ln³⁺ ions. The luminescence properties and the porosity of PMOs give them the ability to discern variations in their surrounding

environment. This attribute allows applications in turn-off chemical sensing, achieved by modulating guest motifs through host-guest interactions.⁴⁶ To investigate the metal ion selectivity exhibited by acac(20)-PMO@Eu_tta materials, fluorescence experiments were systematically conducted, as depicted in Figure 3.3. The ion sensing performance of this material was assessed through the use of a suspension with a concentration of 1 mg/mL. In Figure 3.3a, we have compiled and compared the photoluminescence spectra of interest. Most suspensions containing various metal ions (Pb^{2+} , Na^+ , Al^{3+} , K^+ , Mg^{2+} , Ca^{2+} , Sr^{2+} , Fe^{3+} , Hg^{2+} , Cr^{3+} , Y^{3+} , Zn^{2+} , and Cu^{2+}) exhibit the characteristic purplish-red luminescence attributed to acac(20)-pmo and Eu^{3+} transitions. However, only the presence of Cu^{2+} results in a substantial reduction in luminescence intensity, indicating a pronounced quenching effect. This observation underscores the high selectivity of acac(20)-PMO@Eu_tta for the detection and specific identification of Cu^{2+} in aqueous solutions. Notably, under UV light excitation at 302 nm, this quenching effect is visible to the naked eye (Figure 3.3a inset), where the color transition from purplish-red to blue is observed. It shows the color primarily originates from acac(20)-PMO after the addition of Cu^{2+} (Figure S3.2b). It can be, in part, elucidated by the Cu(II) static quenching mechanism, which arises from the formation of non-fluorescent ground-state complexes.⁴⁷ In the PL decay time analysis shown in Figure 3.3b, we also observed a decrease in the PL lifetime upon the addition of Cu^{2+} . The initial PL lifetime, recorded in the absence of Cu^{2+} , is established at 201 μs . A titration of Cu^{2+} into the system results in a measurable decrease in the PL lifetime, reaching a minimum of 175 μs . This trend confirms the quenching effect, emphasizing the selective interaction between Cu^{2+} ions and the acac(20)-PMO@Eu_tta framework. The change in decay time suggests an underlying mechanism involving energy or electron transfer, likely indicative of the formation of a charge transfer complex with Cu^{2+} , which may be attributed to

both dynamic quenching and the paramagnetic nature of the Cu^{2+} ions.^{48, 49} Luminescence titration experiments were conducted to investigate the luminescent response of acac(20)-PMO@Eu_tta in the presence of Cu^{2+} ions. With an increasing concentration of Cu^{2+} ions, there was a marked reduction in the emission intensity of acac(20)-PMO@Eu_tta, as depicted in Figure 3.3c. This effect resulted in the complete quenching of fluorescence emission in the Eu^{3+} hybrid suspension when the Cu^{2+} concentration reached 30 μM (Figure S3.3).

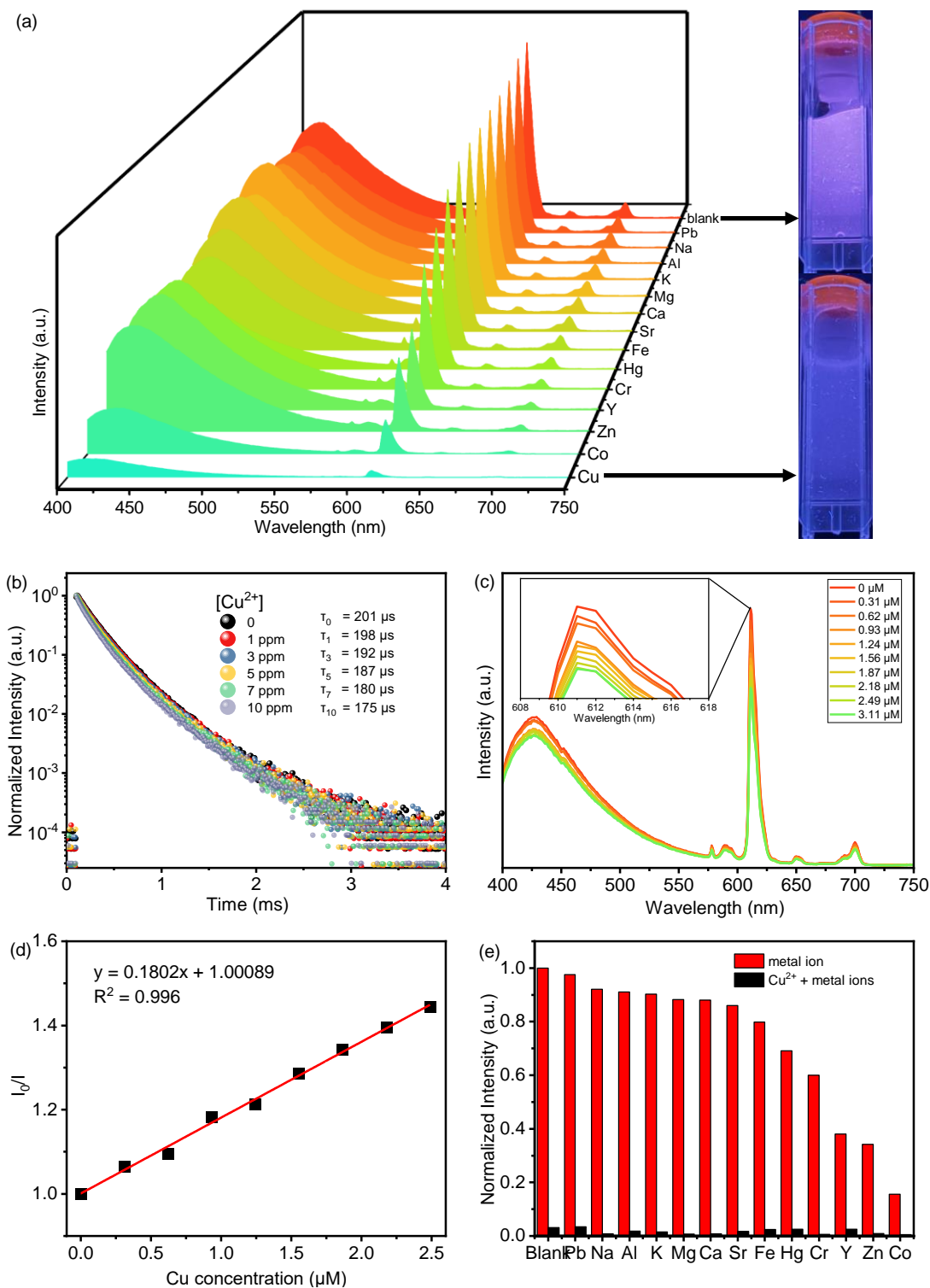


Figure 3.3 (a) Emission spectra of the colloidal suspensions of acac(20)-PMO@Eu_{tta} in the presence of different metal ions (Pb²⁺, Na⁺, Al³⁺, K⁺, Mg²⁺, Ca²⁺, Sr²⁺, Fe³⁺, Hg²⁺, Cr³⁺, Y³⁺, Zn²⁺, and Cu²⁺) when excited at 343 nm; (b) Luminescence decay profile of colloidal suspensions of acac(20)-PMO@Eu_{tta} before and after the addition of Cu²⁺ ions. (c) Luminescence spectra of acac(20)-PMO@Eu_{tta} under different concentrations of Cu²⁺ aqueous solutions; (d) Plot of the Stern-Volmer curve between the luminescence intensity and Cu²⁺ concentration in an aqueous solution; (e) Comparison of the luminescence intensities

(611 nm) of acac(20)-PMO@Eu_tta with varied ions (Pb²⁺, Na⁺, Al³⁺, K⁺, Mg²⁺, Ca²⁺, Sr²⁺, Fe³⁺, Hg²⁺, Cr³⁺, Y³⁺, and Zn²⁺) before and after treated by Cu²⁺.

To quantitatively assess this luminescence quenching effect, we employed the Stern-Volmer (S-V) equation. The Stern-Volmer quenching constant (K_{SV}) was calculated as a measure of the quenching efficiency and enabling a precise characterization of the interaction between acac(20)-PMO@Eu_tta and Cu²⁺ ions:

$$\frac{I_0}{I} = K_{SV}c + 1 \quad (1)$$

where I_0 and I are the luminescence intensities of acac(20)-PMO@Eu_tta suspension before and after the addition of the Cu²⁺ ion, respectively, and c is the molar concentration of Cu²⁺.^{27, 50} A linear relation ($R^2 = 0.996$) was achieved in the concentration range of 0 to 2.5 μ M (Figure 3.3d). The calculated K_{SV} value is 180198 M⁻¹. The limit of detection (LOD) was calculated to be 108 nM (26 ppb) according to the method used by Armbruster et al., assuming that

$$LOD = 3\sigma/K_{SV} \quad (2)$$

where σ represents the standard deviation of the response, which can be determined by assessing the standard deviation of measurements from the blank sample.⁵¹⁻⁵³ The calculated value was significantly lower than the permissible level of Cu²⁺ in drinking water, which is set at 1.3 ppm (6.9 μ M) by the Environmental Protection Agency (EPA).⁵⁴ Selectivity plays a pivotal role in assessing the effectiveness of a sensing material for the detection of specific analytes in real-world applications, as it determines the material's ability to distinguish the target analyte from other environmental components.⁵⁵ The relative PL intensity of the probe was assessed following the introduction of various common metal ions, each at the same concentration. These metal ions included Pb²⁺, Na⁺, Al³⁺, K⁺, Mg²⁺, Ca²⁺, Sr²⁺, Fe³⁺, Hg²⁺, Cr³⁺, Y³⁺, Zn²⁺, and Cu²⁺, as depicted in Figure 3.3e. Only upon the addition of Cu²⁺ ions to metal ion-enriched PMO dispersions, a significant quenching of the

photoluminescence (PL) intensity was observed. This effect underscores the acac(20)-PMO@Eu₃Tb's high selectivity for Cu²⁺, distinguishing it from a variety of other metal ions. Notably, the method's selectivity was evident in distinguishing Cu²⁺ ions from Hg²⁺ and Pb²⁺, which are common competitors often encountered in real-world field samples. Furthermore, in comparison to prior Cu²⁺ sensing methods based on nanoparticle fluorometric sensors in aqueous system, the proposed approach exhibits a comparable linear range and selectivity, and sensitivity, as summarized in Table S3.1.^{56, 57} To date, only a limited number of copper sensors based on LnPMOs have been reported as turn-on fluorescence chemical sensors.^{29, 31.}

3.3.3 Catalytic properties

The acac(100)-PMO was utilized as a heterogeneous catalysis by anchoring VO(acac)₂ onto the material, resulting in a catalyst containing 0.59 mmol V/g (cat). The surface elemental composition of acac(100)-PMO and acac(100)-PMO@VO₂acac was analyzed using XPS. Figure 3.4a and 3.4d illustrate the presence of elements such as V, C, O, and Si on the surfaces of these nanocomposites. In Figure 3.4b and 3.4e, the C 1s region reveals the presence of multiple chemical states of carbon. Four distinct peaks were discerned and attributed to C-Si(282.6 eV), C-C and C-H (284.8 eV), C-O (286.9 eV), and C=O species (289.8 eV).⁵⁸ The increasing peak of C=O can be attributed to the grafting of VO(acac)₂. In the XPS O 1s spectra, two distinct peaks were observed at 531.9 and 532.9 eV. These peaks can be attributed to the presence of C=O and -C-OH groups, likely arising from the tautomerization of the acac group in both its keto and enol forms, as illustrated in Figure 3.4c and 3.4f. The high-resolution XPS spectrum of V 2p can be deconvoluted into two primary doublet peaks, as depicted in Figure S3.5. In this detailed spectrum, The doublet peaks at 515.3 eV and 522.2 eV correspond to V 2p_{3/2} and V 2p_{1/2},

respectively.⁵⁹ This observation suggests the presence of V(IV) in the acac(100)-PMO@VO_acac.

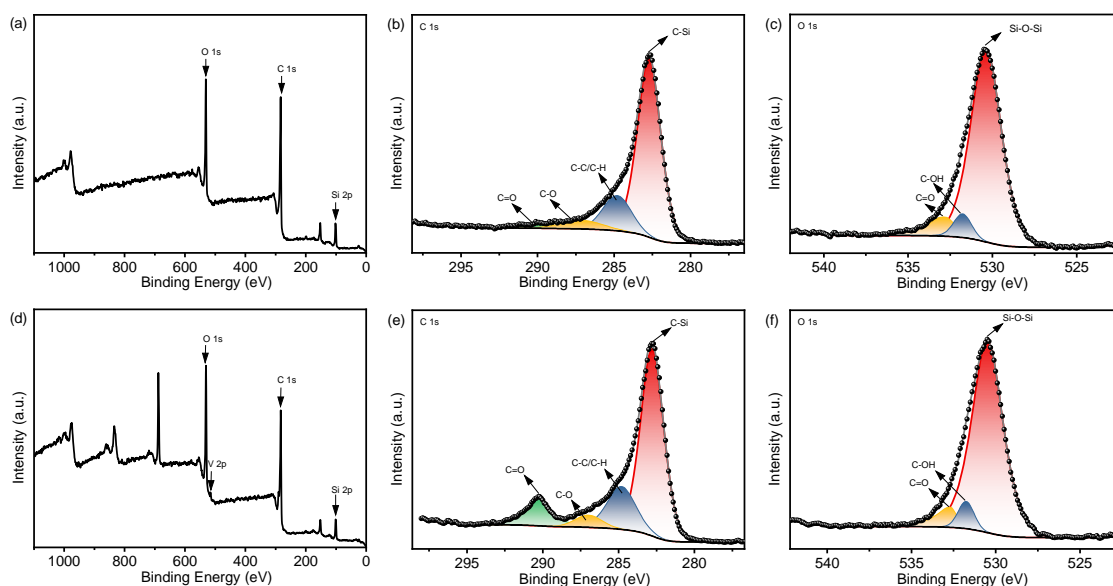
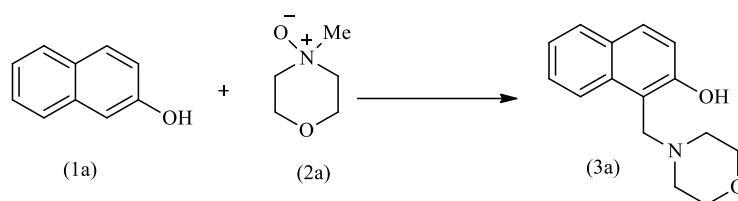


Figure 3.4 XPS spectra of acac(100)-PMO and acac(100)-PMO@VO_acac

Upon completing the material characterization, the catalytic performance of the acac(100)-PMO@VO_acac material was tested for the model Mannich-type reaction, as shown in Table 3.3. During a typical catalytic test, predetermined quantities of 2-naphthol and *N*-methylmorpholine *N*-oxide (NMO), along with the catalyst were combined. The mixture was then refluxed in anhydrous DCM within a 10 mL Schlenk tube under an inert atmosphere. At specific time intervals, the catalyst was separated, and the filtrate was evaporated until dryness, resulting in the formation of the pure Mannich base with a quantitative yield. The confirmation of product formation was achieved through ¹H NMR spectroscopy.

Table 3.2 Role of different reaction conditions for Preliminary Mannich-Type Reactiona.



Entry	catalyst	1a:2a	time (h)	yield (%) ^b
1	---	1:2	12	---
2	VO(acac) ₂ ^c	1:3	12	92
3	Acac(100)-PMO	1:3	12	---
4	Acac(100)-PMO@VO_acac	1:3	12	98
5	Acac(100)-PMO@VO_acac	1:2	12	98
6	Acac(100)-PMO@VO_acac	1:1.5	12	96
7	Acac(100)-PMO@VO_acac	1:1	12	70
8	Acac(100)-PMO@VO_acac	1:2	1	16
9	Acac(100)-PMO@VO_acac	1:2	6	40
10	Acac(100)-PMO@VO_acac	1:2	24	98

^aReaction conditions: 2-Naphthol (1 mmol), NMO, DCM (2 mL) and catalyst (15 mg). ^bYield was calculated from ¹H NMR analysis using mesitylene as internal standard. ^c10 mol %.

Initially, the Mannich type reaction between 2-naphthol (**1a**) and 4-methylmorpholine N-oxide (NMO) (**2a**) was conducted in the absence of a catalyst at 40 °C. After 12 hours of reaction, no substrate conversion occurred, highlighting the necessity of the presence of a catalyst (Table 3.3, entry 2). Subsequently, we investigated the catalytic activity of VO(acac)₂ for this model reaction. This complex exhibited a yield of 92% after 12 hours of reaction. However, it is hard to recycle this homogeneous catalyst.^{17, 18, 20} For the heterogeneous acac(100)-PMO@VO_acac catalyst, a 16% yield of the major product, 1-(morpholinomethyl)naphthalen-2-ol

(3a), was obtained within 60 minutes. An increase in the yield from 40% to 98% was obtained upon extending the reaction time from 6 to 12 hours. Moreover, we conducted the reaction multiple times with varying equivalents of NMO. When employing 1, 1.5, 2, or 3 equivalents of NMO under the optimized reaction conditions, we observed yields of 70%, 96% and 98% of 3a, respectively. The highest yield of 92% for 3a was achieved using 3 equivalents of NMO.

The recyclability and structural stability of acac(100)-PMO@VO₂ acac material were studied during the preparation of 1 (morpholinomethyl)naphthalen-2-ol under optimized reaction conditions. After completing the reaction, the recyclability test was conducted using the recovered catalyst. The catalyst was thoroughly washed with dichloromethane and dried under vacuum at 120 °C before being utilized in the subsequent catalytic reaction. The catalyst demonstrated consistent activity, with no significant decrease up to the four tested cycles (Figure 3.5).

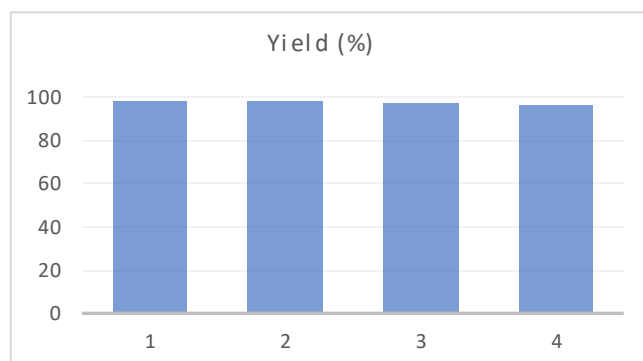


Figure 3.5 Recycling test of acac(100)-PMO@VO₂ acac catalyst for Mannich-type reaction.

Furthermore, a hot filtration test was performed to assess the potential leaching of vanadium ions from the support. The catalyst was removed from the reaction mixture after 6 hours, and the reaction was allowed to continue for an additional 18 hours (Figure 3.6). No further progress was observed in the reaction, indicating the absence of leaching.

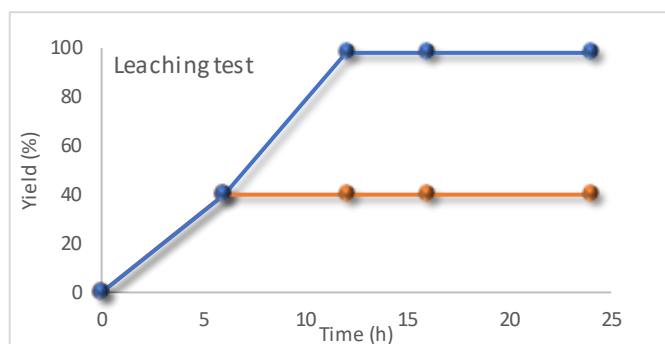


Figure 3.6 Reaction profile with or without the catalyst (after separating the catalyst from the reaction mixture via hot-filtration technique).

To examine the physio-chemical properties of the catalyst, FT-IR and XPS analyses were conducted, as depicted in Figure 3.7. The recovered catalyst exhibited all the characteristic peaks, similar to the fresh catalyst. Additionally, the XPS analysis of the recycled catalyst (Figure 3.7b-d) displayed the same specific peaks as the fresh catalyst. These results confirm that the chemical structure of the catalyst was preserved during the recycling process.

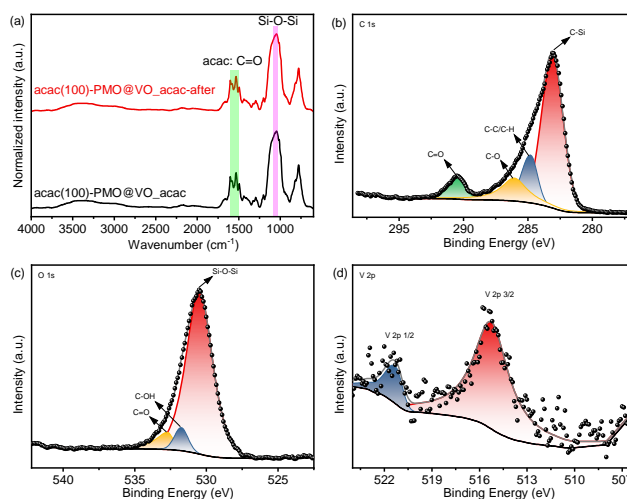
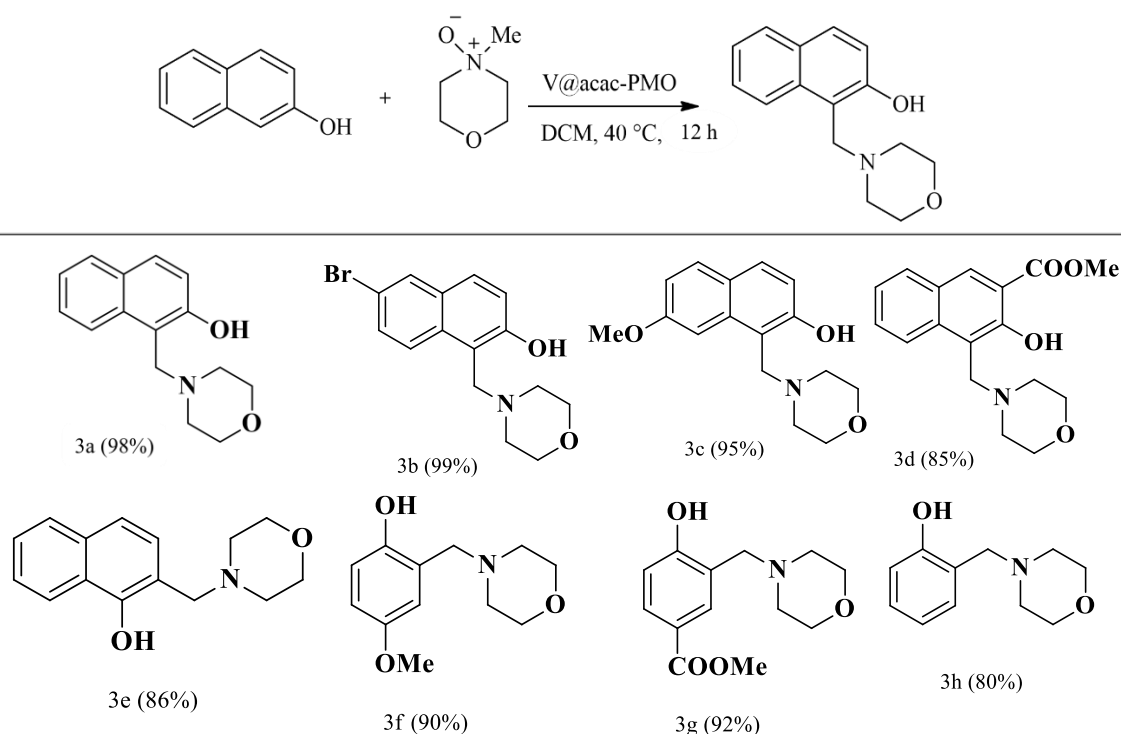


Figure 3.7 (a) DRIFT spectra of acac(100)-PMO@VO_acac before and after Mannich-type reaction; (b) Deconvoluted XPS C 1s spectra, (c) O 1s spectra and (d) vanadium in the V 2p region of the recycled acac(100)-PMO@VO_acac.

The catalytic reactivity of the acac(100)-PMO@VO_acac catalyst was evaluated using a diverse range of substrates, including 2-naphthol, 1-naphthol, and phenol derivatives, under the optimized reaction conditions (Table 3.4). Substantial

catalytic conversion was achieved for nearly all the substrates, regardless of whether they had electron-donating or electron-withdrawing substituents on the aromatic ring.

Table 3.3 Mannich-Type reaction with differently substituted substrates catalyzed by acac(100)-PMO@VO₂acac.



Yields are calculated from ¹H NMR using mesitylene as an internal standard.

In Scheme S3.1, a plausible pathway for the preparation of the Mannich base was proposed, following similar steps as previously reported by Uang et al.^{17, 60-62} Initially, the active V=O groups of the catalyst formed complexes with 4-methylmorpholine *N*-oxide, leading to the formation of a six-membered structure (A). An intramolecular elimination process via this transition structure resulted in the formation of an iminium ion B structure. Second, the [V(OH)(O⁻)] species played a crucial role in abstracting an acidic proton from 2-naphthol, generating a negatively charged oxygen species. This species further creates an acidic carbon center. A target Mannich base formed through a reaction of this acidic carbon center

with iminium ions. Finally, the elimination of water molecules from $V(OH)_2$ regenerated the catalyst, completing the catalytic cycle.

The catalytic performance of $acac(100)\text{-PMO@VO_acac}$ was compared to its homogeneous counterpart, $VO(acac)_2$, as well as $acac$ -based covalent triazine frameworks (CTFs) and covalent organic frameworks (COFs) in Table S3.2.^{17, 60, 61, 63} It is evident from Table S3.2 that the $acac(100)\text{-PMO@VO_acac}$ catalyst resulted in the targeted product with a high yield and conversion rate. When compared with $VO(acac)_2$, it exhibited a higher yield (98%) and turnover number (TON) of 111, which is 12 times greater than the TON achieved by the homogeneous catalyst. Moreover, we evaluated the catalytic activity of $acac(100)\text{-PMO@VO_acac}$ in comparison to $acac$ -based COFs, such as vanadium-docked COFs ($VO\text{-TAPT-2,3-DHTA}$ COF, $VO\text{-PyTTA-2,3-DHTA}$ COF). In these cases, the catalysts resulted in the targeted product with yield of 98% and 96%, along with TON values of 29 and 36, respectively. This combination of high conversion and TON suggests potential for $acac(100)\text{-PMO@VO_acac}$ as a heterogeneous catalyst. These findings substantiate the promising future of $acac\text{-PMO}$ materials as versatile supports for the development of advanced heterogeneous catalysts.

3.4 Conclusions

This study introduces a novel PMOs with embedded acetylacetonate ($acac$) groups, showcasing its dual utility in catalysis and sensing. The $acac(20)\text{-PMO}$ grafted with $Eu(tta)_3$ demonstrates effectiveness as a luminescent sensor towards aqueous Cu^{2+} ions, achieving a LOD of 108 nM. In addition, a heterogeneous catalyst ($acac(100)\text{-PMO@VO_acac}$) was prepared by anchoring $VO(acac)_2$ on pristine $acac\text{-PMO}$ that showed high reactivity in a modified Mannich reaction with a turnover number (TON) of 111 and a wide substrate scope. Furthermore, the embedded $acac$ functionality's capacity to tether "hard" metal ions suggests potential applications in sensing, catalysis, and water purification. These

findings underscore the versatility of acac-PMOs and open new avenues for their application in environmental and industrial contexts.

3.5 Supporting information.

Table S 3.1 The comparisons of the sensing performance for different MOFs and PMOs probes.

Fluorescence probe	Materials	Analytes detected	Linear range	$K_{sv}(M^{-1})$	LOD	Ref
NS-CQDs	carbon quantum dots (CQDs)	Cu^{2+}	0 – 1 μM	-	1.65 μM	64
SiO_2/CdS NCs	nanocrystals	Cu^{2+}	0 – 3 μM	-	$3.5 \times 10^{-2} \mu M$	65
ZCM microsphere	QD composite	Cu^{2+} , Cr^{2+} , Fe^{3+}	0 – 1 μM	3.85×10^5	$1.6 \times 10^{-5} \mu M$	66
CE/11-MUA-AuNCs	gold nanoclusters	Cu^{2+} , Cd^{2+} , Zn^{2+}	0.05–10 μM	-	0.026 μM	67
AlEgens fabricated on nanoscale ZIF-8	aggregation-induced emission luminogens with MOFs	Cu^{2+}	0 – 0.1 μM	-	$5.5 \times 10^{-4} \mu M$	68
$[Ce(1,5-NDS)_{1.5}(H_2O)_5]_n$	MOFs	Cu^{2+}	5 - 100 μM	7668	3 μM	69
AuNCs/PQD@ SiO_2	gold nanocomposites	Cu^{2+}	0 - 160 μM	4400	3 μM	70
QG-scaffolded COFs	COFs	Cu^{2+}	0.0032 - 32 μM	-	$5 \times 10^{-4} \mu M$	71
$[Eu(bpdc)_{1.5}(H_2O)_2]_n$	Eu-MOFs	Fe^{3+} , Cu^{2+} , PO_4^{3-}	0 – 400 μM	3240	33 μM	72
$\{[Eu(L)(DMF)(H_2O)] \cdot 0.5DMF\}_n$	Eu-MOFs	Cu^{2+}	0.01 - 1000 μM	4.3×10^4	$1.02 \times 10^3 \mu M$	73
$[Eu(L)(DEF)(H_2O)]_n$	Eu-MOFs	Cu^{2+}	0.01 - 1000 μM	5.7×10^4	$5 \times 10^4 \mu M$	74
Eu-MOFs (4, 40-AZ, DMF and H_3BTC)	Eu-MOFs	Cu^{2+}	2 - 1000 μM	2.9×10^4	1.395 μM	74
$\{[Tb(HL)] \cdot 3DMF \cdot 3H_2O\}_n$ (LZG-Tb)	Tb-MOFs	Cu^{2+}	0 - 0.25 μM	8.2×10^6	$1.65 \times 10^{-3} \mu M$	32
$\{[Eu(HL)] \cdot 3DMF \cdot 3H_2O\}_n$ (LZG-Eu)	Eu-MOFs	Cu^{2+}	0 - 0.25 μM	4.9×10^6	$1.35 \times 10^{-3} \mu M$	32
TH-PMO-100	PMOs	Cu^{2+}	0.1 - 1 μM	1.6×10^4	40 μM	75
RSPMOs	PMOs	Cu^{2+}	0.1 - 1 μM	-	0.1 μM	76
SCN-PMO	PMOs	Cu^{2+}	8.75 - 20 μM	-	0.67 μM	77
Ag-PMO-YS	nanocomposites	Cu^{2+}	0.1 - 9 μM	-	0.02 μM	78
Eu(NTA) $_3$ L-COOH-PMO	Eu-PMOs	Cu^{2+}	0 - 20 μM	2.5×10^6	0.046 μM	31
ePMO@Eu_PA	Eu-PMOs	Cu^{2+}	0 - 400 μM	2100	35.2 μM	29
acac(20)-PMO@Eu_tta	Eu-PMOs	Cu^{2+}	0 - 2.5 μM	1.8×10^5	0.108 μM	This work

Table S 3.2 Comparison of the acac-PMO catalyst with Other VO(acac) $_2$ based catalyst.

Entry	Catalyst	Reaction conditions	Yield (%)	TON ^a	Ref
1	VO(acac) $_2$	catalyst (10 mol %), CH_2Cl_2 , reflux, 8 h	92	9.2	60
2	VO-TAPT-2,3-DHTA COF	catalyst (35 mg, 0.97 mmol/g V), DCM, 40 $^{\circ}C$, 12 h	98	29	61
3	VO-PyTTA-2,3-DHTA COF	catalyst (35 mg, 0.77 mmol/g V), DCM, 40 $^{\circ}C$, 12 h	96	36	61
3	V@acac-CTF	catalyst (40 mg, 0.306 mmol/g V), DCM, 40 $^{\circ}C$, 8 h	95	213	17
4	acac(100)-PMO@VO_acac	catalyst (15 mg, 0.59 mmol/g V), DCM, 40 $^{\circ}C$, 12 h	98	111	This work

^a TON = turnover number

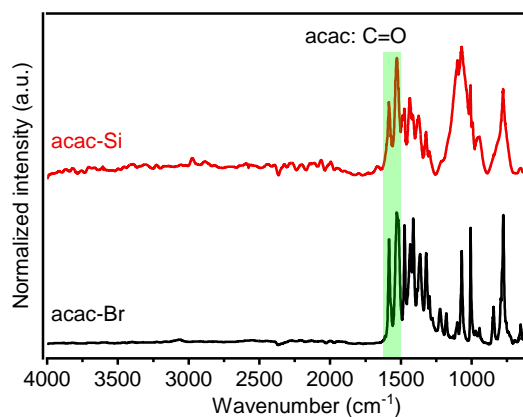


Figure S3.1 FT-IR spectra of acac-Br and acac-Si.

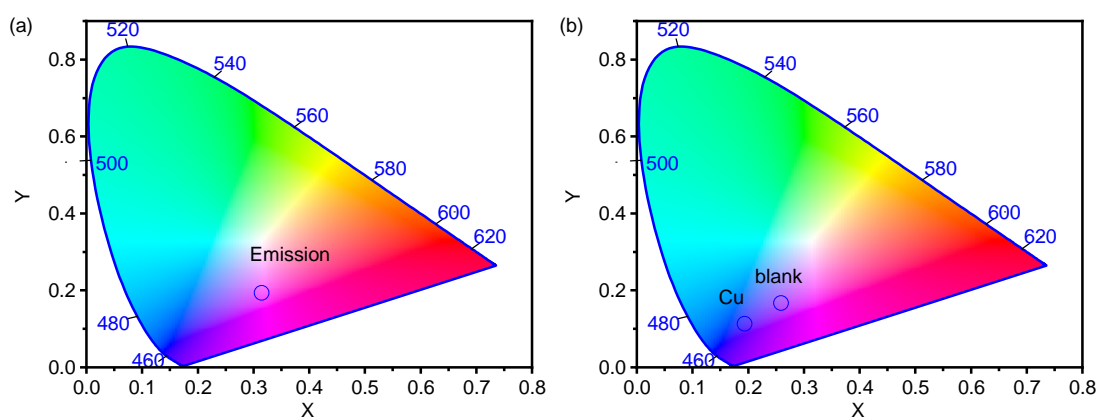


Figure S3.2. CIE chromaticity diagram of (a) solid acac(20)-PMO@Eu_tta; (b) colloidal suspensions of acac(20)-PMO@Eu_tta with and without Cu^{2+} .

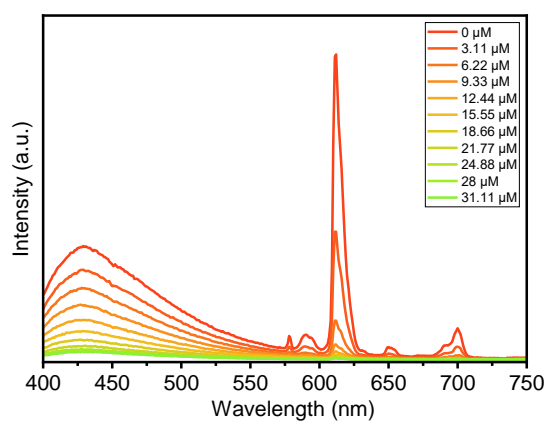


Figure S3.3 Luminescence spectra of LnPMO under different concentrations of Cu^{2+} aqueous solutions.

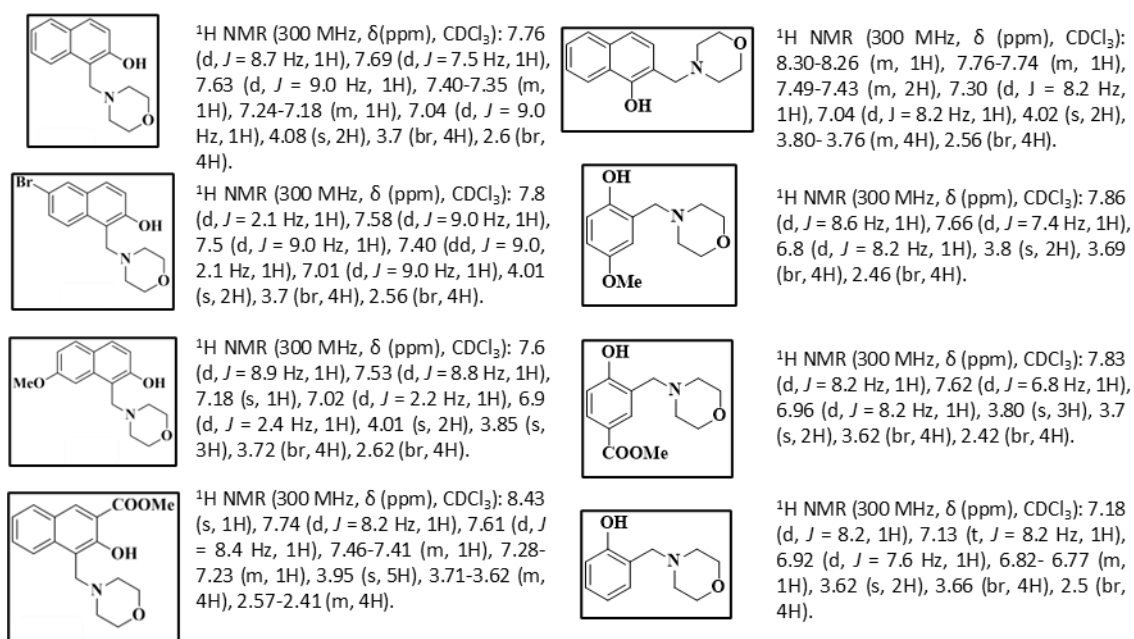


Figure S3.4. $^1\text{H-NMR}$ data of Mannich-reaction product in CDCl_3 .

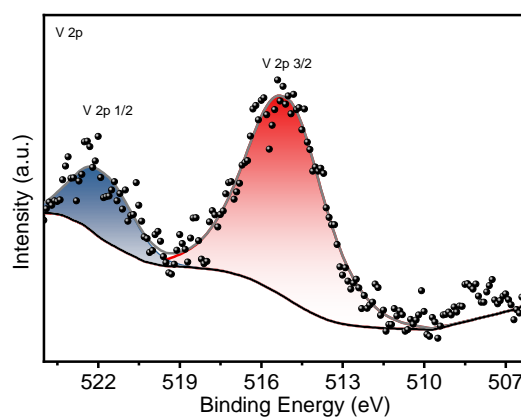
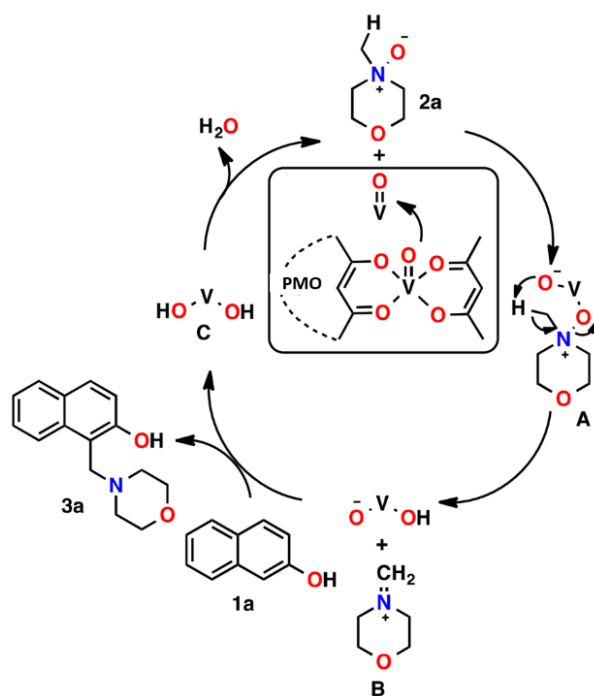


Figure S3.5. Deconvoluted XPS spectra of vanadium in the V 2p region for acac(100)-PMO@VO₂ acac catalyst.



Scheme S 3.1 Proposed mechanism of Mannich-type reaction catalyzed by acac(100)-PMO@VO₂acac.

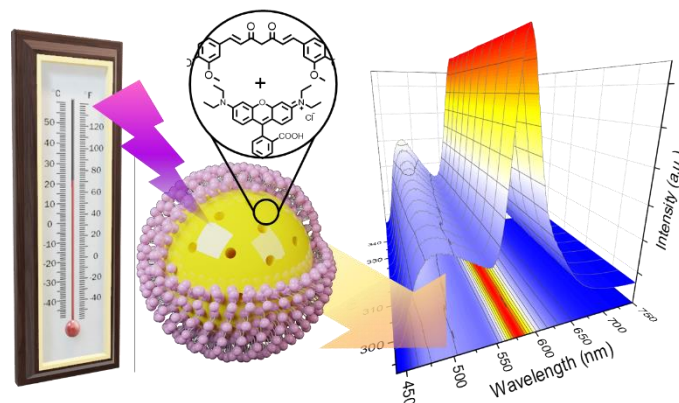
3.6 Reference

1. S. S. Park, M. S. Moorthy and C. S. Ha, *NPG Asia Mater.*, 2014, **6**, e96-e96.
2. T. Asefa, M. J. MacLachlan, N. Coombs and G. A. Ozin, *Nature*, 1999, **402**, 867-871.
3. B. J. Melde, B. T. Holland, C. F. Blanford and A. Stein, *Chem. Mater.*, 1999, **11**, 3302-3308.
4. S. Inagaki, S. Guan, Y. Fukushima, T. Ohsuna and O. Terasaki, *J. Am. Chem. Soc.*, 1999, **121**, 9611-9614.
5. C. T. Kresge, M. E. Leonowicz, W. J. Roth, J. C. Vartuli and J. S. Beck, *Nature*, 1992, **359**, 710-712.
6. D. Zhao, J. Feng, Q. Huo, N. Melosh, G. H. Fredrickson, B. F. Chmelka and G. D. Stucky, *Science*, 1998, **279**, 548-552.
7. M. Ferré, R. Pleixats, M. Wong Chi Man and X. Cattoën, *Green Chem.*, 2016, **18**, 881-922.
8. P. Van der Voort, D. Esquivel, E. De Canck, F. Goethals, I. Van Driessche and F. J. Romero-Salguero, *Chem. Soc. Rev.*, 2013, **42**, 3913-3955.
9. Y. Wei, X. Li, R. Zhang, Y. Liu, W. Wang, Y. Ling, A. M. El-Toni and D. Zhao, *Sci Rep*, 2016, **6**, 20769.
10. A. M. Kaczmarek, S. Abednatanzi, D. Esquivel, C. Krishnaraj, H. S. Jena, G. B. Wang, K. Leus, R. Van Deun, F. J. Romero-Salguero and P. Van der Voort, *Microporous Mesoporous Mater.*, 2020, **291**, 109687.
11. A. A. Gismatulin, V. A. Gritsenko, D. S. Seregin, K. A. Vorotilov and M. R. Baklanov, *Appl Phys Lett*, 2019, **115**, 082904.
12. X. Feng, F. Li, L. Zhang, W. Liu, X. Wang, R. Zhu, Z. A. Qiao, B. Yu and X. Yu, *Acta Biomater.*, 2022, **143**, 392-405.
13. A. M. Kaczmarek and P. Van der Voort, *J Mater Chem C*, 2019, **7**, 8109-8119.
14. M. A. Bennett, M. J. Byrnes and I. Kovacic, *J Organomet Chem*, 2004, **689**, 4463-4474.
15. P. Muraoka, D. Byun and J. I. Zink, *Coord Chem Rev*, 2000, **208**, 193-211.
16. W. H. Wang, T. L. Yung, S. S. Cheng, F. Chen, J. B. Liu, C. H. Leung and D. L. Ma, *Sens. Actuators B Chem.*, 2020, **321**, 128486.
17. H. S. Jena, C. Krishnaraj, G. B. Wang, K. Leus, J. Schmidt, N. Chaoui and P. Van der Voort, *Chem. Mater.*, 2018, **30**, 4102-4111.
18. A. R. Hajipour and G. Azizi, *Green Chem.*, 2013, **15**, 1030-1034.
19. A. Hajipour and G. Azizi, *Appl Organomet Chem*, 2015, **29**, 247-253.
20. P. Borah, X. Ma, K. T. Nguyen and Y. Zhao, *Angew. Chem. Int. Ed.*, 2012, **51**, 7756-7761.
21. B. B. Lai, Z. P. Huang, Z. F. Jia, R. X. Bai and Y. L. Gu, *Catal Sci Technol*, 2016, **6**, 1810-1820.
22. C. Pereira, A. R. Silva, A. P. Carvalho, J. Pires and C. Freire, *J Mol Catal A Chem*, 2008, **283**, 5-14.
23. S. V. Eliseeva and J. C. Bunzli, *Chem. Soc. Rev.*, 2010, **39**, 189-227.
24. C. H. Liu, A. M. Kaczmarek, H. S. Jena, Z. T. Yang, D. Poelman and P. van der Voort, *J Mater Chem C*, 2023, **11**, 5634-5645.
25. Y. Liu, Q.-L. Shi and J.-L. Yuan, *Chin Chem Lett*, 2015, **26**, 1485-1489.
26. H. Li, Y. Li, Z. Zhang, X. Pang and X. Yu, *Materials & Design*, 2019, **172**.
27. A. M. Kaczmarek and P. Van Der Voort, *J Mater Chem C*, 2019, **7**, 8109-8119.
28. A. M. Kaczmarek, S. Abednatanzi, D. Esquivel, C. Krishnaraj, H. S. Jena, G. Wang, K. Leus, R. Van Deun, F. J. Romero-Salguero and P. Van Der Voort, *Microporous Mesoporous Mater.*, 2020, **291**, 109687-109688.
29. W. Liu, A. M. Kaczmarek, H. Rijckaert, P. Van Der Voort and R. Van Deun, *Dalton Trans*, 2021, **50**, 11061-11070.
30. W. Liu, A. M. Kaczmarek, P. Van Der Voort and R. Van Deun, *Dalton Trans.*, 2022, **51**, 11467-11475.
31. H. Li, Y. J. Li, Z. Zhang, X. L. Pang and X. D. Yu, *Mater Design*, 2019, **172**, 107712.
32. Z. G. Lin, F. Q. Song, H. Wang, X. Q. Song, X. X. Yu and W. S. Liu, *Dalton Trans.*, 2021, **50**, 1874-1886.
33. N. Brun, B. Julian-Lopez, P. Hesemann, G. Laurent, H. Deleuze, C. Sanchez, M. F. Achard and R. Backov, *Chem. Mater.*, 2008, **20**, 7117-7129.
34. K. Binnemans, P. Lenaerts, K. Driesen and C. Görrler-Walrand, *J. Mater. Chem.*, 2004, **14**, 191-195.
35. L. Carlucci, G. Ciani, S. Maggini, D. M. Proserpio and M. Visconti, *Chem. Eur. J.*, 2010, **16**, 12328-12341.

36. Z. Zhang, H. Chang, Y. F. Kang, X. P. Li, H. Jiang, B. L. Xue, Y. Y. Wang, X. Q. Lü and X. J. Zhu, *Sens. Actuators B Chem.*, 2019, **282**, 999-1007.
37. L. Bourda, H. S. Jena, R. Van Deun, A. M. Kaczmarek and P. Van der Voort, *J. Mater. Chem. A*, 2019, **7**, 14060-14069.
38. A. M. Kaczmarek, Y. Maegawa, A. Abalymov, A. G. Skirtach, S. Inagaki and P. Van Der Voort, *ACS Appl. Mater. Interfaces*, 2020, **12**, 13540-13550.
39. G. Chandrasekar, K. S. You, J. W. Ahn and W. S. Ahn, *Microporous Mesoporous Mater.*, 2008, **111**, 455-462.
40. B. Guan, Y. Cui, Z. Ren, Z. A. Qiao, L. Wang, Y. Liu and Q. Huo, *Nanoscale*, 2012, **4**, 6588-6596.
41. E. Valiey and M. G. Dekamin, *Nanoscale Adv.*, 2022, **4**, 294-308.
42. P. Van Der Voort, K. Leus and E. De Canck, *Introduction to porous materials*, John Wiley & Sons, 2019.
43. M. Thommes, K. Kaneko, A. V. Neimark, J. P. Olivier, F. Rodriguez-Reinoso, J. Rouquerol and K. S. Sing, *Pure Appl. Chem.*, 2015, **87**, 1051-1069.
44. A. M. Kaczmarek, Y. Y. Liu, M. K. Kaczmarek, H. Liu, F. Artizzu, L. D. Carlos and P. Van Der Voort, *Angew. Chem.*, 2020, **132**, 1948-1956.
45. X. Guo, X. Wang, H. Zhang, L. Fu, H. Guo, J. Yu, L. D. Carlos and K. Yang, *Microporous Mesoporous Mater.*, 2008, **116**, 28-35.
46. J. Lin, Q. Cheng, J. Zhou, X. Lin, R. C. K. Reddy, T. Yang and G. Zhang, *J. Solid State Chem.*, 2019, **270**, 339-345.
47. N. Ding, D. L. Zhou, G. C. Pan, W. Xu, X. Chen, D. Y. Li, X. H. Zhang, J. Y. Zhu, Y. A. Ji and H. W. Song, *Acs Sustain Chem Eng*, 2019, **7**, 8397-8404.
48. T. Kohlmann and M. Goez, *Phys. Chem. Chem. Phys.*, 2019, **21**, 10075-10085.
49. L. Li, S. Shen, R. Lin, Y. Bai and H. Liu, *Chem. Comm.*, 2017, **53**, 9986-9989.
50. G. Ji, J. Liu, X. Gao, W. Sun, J. Wang, S. Zhao and Z. Liu, *J. Mater. Chem. A*, 2017, **5**, 10200-10205.
51. D. A. Armbruster and T. Pry, *Clin Biochem Rev*, 2008, **29**, S49.
52. M. E. Zorn, R. D. Gibbons and W. C. Sonzogni, *Anal. Chem.*, 1997, **69**, 3069-3075.
53. E. Mohamed Ali, Y. Zheng, H.-h. Yu and J. Y. Ying, *Anal. Chem.*, 2007, **79**, 9452-9458.
54. U. Latief, S. Ul Islam, Z. Khan and M. S. Khan, *J Alloy Compd*, 2022, **910**, 164889.
55. H. Li, Y. Li, Z. Zhang, X. Pang and X. Yu, *Materials & Design*, 2019, **172**, 107712.
56. T. Chopra, S. Sasan, L. Devi, R. Parkesh and K. K. Kapoor, *Coord Chem Rev*, 2022, **470**, 214704.
57. X. G. Liu, D. L. Huang, C. Lai, G. M. Zeng, L. Qin, H. Wang, H. Yi, B. S. Li, S. Y. Liu, M. M. Zhang, R. Deng, Y. K. Fu, L. Li, W. J. Xue and S. Chen, *Chem. Soc. Rev.*, 2019, **48**, 5266-5302.
58. Y. Peng, N. Pan, D. Wang, J. Yang, Z. Guo and W. Yuan, *J. Mater. Sci.*, 2018, **53**, 12432-12440.
59. P. Borah, X. Ma, K. T. Nguyen and Y. Zhao, *Angew Chem Int Ed Engl*, 2012, **51**, 7756-7761.
60. D. R. Hwang and B. J. Uang, *Org. Lett.*, 2002, **4**, 463-466.
61. H. Vardhan, L. X. Hou, E. Yee, A. Nafady, M. A. Al-Abdrabalnabi, A. M. Al-Enizi, Y. X. Pan, Z. Y. Yang and S. Q. Ma, *Acs Sustain Chem Eng*, 2019, **7**, 4878-4888.
62. X. Chen, N. Huang, J. Gao, H. Xu, F. Xu and D. Jiang, *ChemComm*, 2014, **50**, 6161-6163.
63. P. P. Reddy, C. Y. Chu, D. R. Hwang, S. K. Wang and B. J. Uang, *Coord Chem Rev*, 2003, **237**, 257-269.
64. N. Chaudhary, P. K. Gupta, S. Eremin and P. R. Solanki, *J. Environ. Chem. Eng.*, 2020, **8**, 103720.
65. T. Xie, X. Zhong, Z. Liu and C. Xie, *Mikrochim. Acta*, 2020, **187**, 323.
66. M. M. R. Khan, T. Mitra and D. Sahoo, *RSC Adv*, 2020, **10**, 9512-9524.
67. M. L. Desai, H. Basu, S. Saha, R. K. Singhal and S. K. Kailasa, *J. Mol. Liq.*, 2020, **304**, 112697.
68. S. Xie, Q. Liu, F. Zhu, M. Chen, L. Wang, Y. Xiong, Y. Zhu, Y. Zheng and X. Chen, *J Mater Chem C*, 2020, **8**, 10408-10415.
69. S. Geranmayeh, M. Mohammadnejad and S. Mohammadi, *Ultrason Sonochem*, 2018, **40**, 453-459.
70. W. Xue, J. Zhong, H. Wu, J. Zhang and Y. Chi, *Analyst*, 2021, **146**, 7545-7553.

71. Y. Y. Cai, Y. Jiang, L. P. Feng, Y. Hua, H. Liu, C. Fan, M. Y. Yin, S. Li, X. X. Lv and H. Wang, *Anal. Chim. Acta*, 2019, **1057**, 88-97.
72. Z. D. Li, Z. Y. Zhan, Y. J. Jia, Z. Li and M. Hu, *J Ind Eng Chem*, 2021, **97**, 180-187.
73. R. R. Ma, Z. W. Chen, S. N. Wang, Q. X. Yao, Y. W. Li, J. Lu, D. C. Li and J. M. Dou, *J Solid State Chem*, 2017, **252**, 142-151.
74. J. C. Zhou, Y. H. Chen, S. Xian, Y. C. Liang, G. J. Huang, L. Wang and X. Z. Yang, *J Solid State Chem*, 2021, **304**, 122542.
75. M. Gao, S. Han, Y. Hu and L. Zhang, *J. Phys. Chem. C*, 2016, **120**, 9299-9307.
76. X. Y. Qiu, S. H. Han and M. Gao, *J. Mater. Chem. A*, 2013, **1**, 1319-1325.
77. M. Gao, C. Xing, X. Jiang, L. Xu, P. Li and C. D. Hsiao, *J. Lumin.*, 2021, **36**, 951-957.
78. L. Yang, S. Shen, J. Zhu, Y. Zhang, Y. Lin, J. Wang, F. Tao, L. Wang and J. Zhang, *ACS Appl. Nano Mater.*, 2023, **6**, 1910-1918.

Chapter 4. Ratiometric Dual-Emitting Thermometers Based on Rhodamine B Dye-Incorporated (Nano) Curcumin Periodic Mesoporous Organosilicas for Bioapplications



The results of this chapter were published in: Ratiometric Dual-Emitting Thermometers Based on Rhodamine B Dye-Incorporated (Nano) Curcumin Periodic Mesoporous Organosilicas for Bioapplications. **Chunhui Liu**, Simona Premcheska , Andre Skirtach, Dirk Poelman, Anna M. Kaczmarek, and Pascal Van Der Voort, 2024, accepted by Journal of Materials Chemistry C.

Abstract

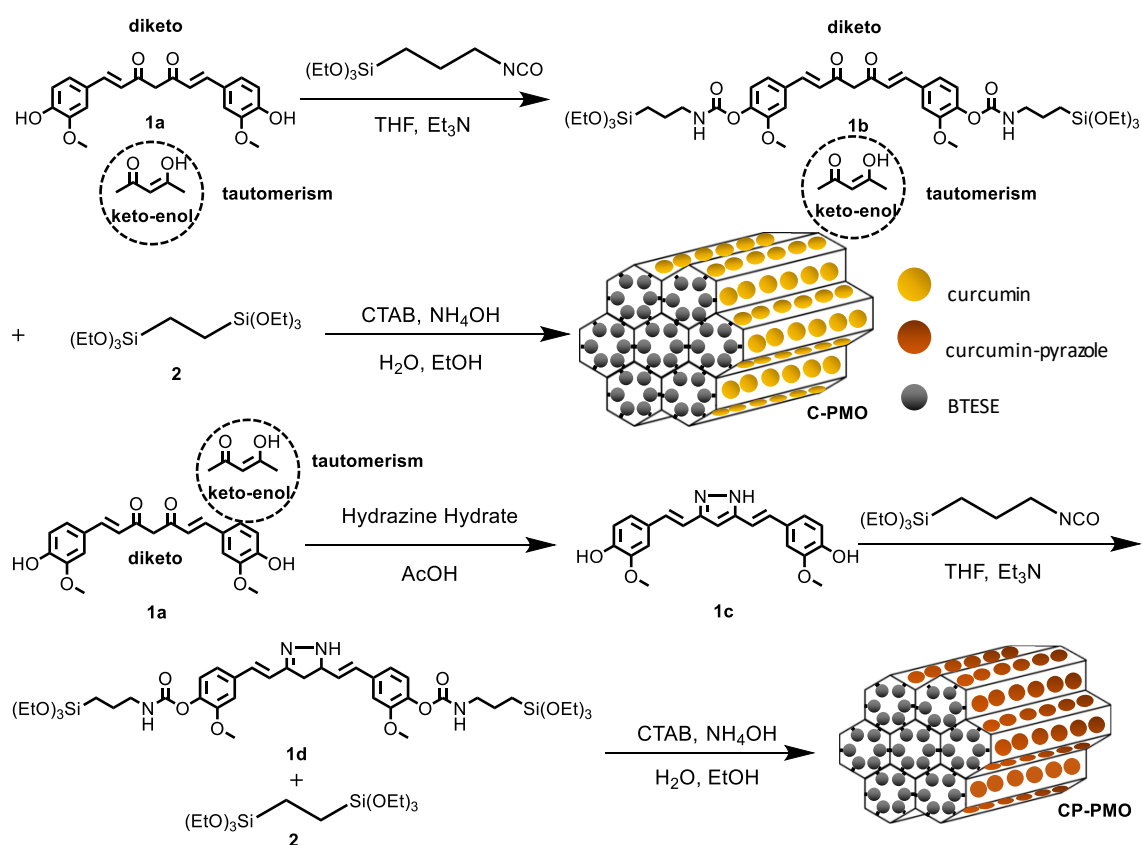
This study explores the potential of combining periodic mesoporous organosilicas (PMOs) with a fluorescent dye to develop a ratiometric thermometry system with enhanced stability, sensitivity, and biocompatibility. PMOs, ordered porous materials known for their stability and versatility, serve as an ideal platform. Curcumin, a natural polyphenol and fluorescent dye, is incorporated into PMOs to develop curcumin-functionalized PMOs (C-PMO) and curcumin-pyrazole-functionalized PMOs (CP-PMO) via hydrolysis and co-condensation. These PMOs exhibit temperature-dependent fluorescence properties. The next step involves encapsulating rhodamine B (RhB) dye within the PMO pores to create dual-emitting PMO@dye nanocomposites, followed by a lipid bilayer (LB) coating to enhance biocompatibility and dye retention. Remarkably, within the physiological temperature range, C-PMO@RhB@LB and CP-PMO@RhB@LB demonstrate noteworthy maximum relative sensitivity (S_r) values of up to 1.69 and 2.60 $\% \cdot K^{-1}$, respectively. This approach offers versatile means to create various ratiometric thermometers by incorporating different fluorescent dyes, holding promise for future temperature sensing applications.

4.1 Introduction

Accurate temperature measurement has become increasingly important in scientific research, technological development, and various applications dependent on sensor thermometers.¹ The rapid advancement of technology has created a demand for temperature sensing and measurement at the nanoscale, such as in nanoelectronics, chemical reactors, and biomedical applications.²⁻⁴ However, traditional contact thermometers, which use physical properties such as volume, electric potential, and electric conductance, are limited in their ability to measure temperature in specific environments, such as those with sub-micrometer scale, biological fluids, or fast-moving objects.⁵ Consequently, there has been a growing interest in noncontact and non-invasive or minimally invasive thermal sensing techniques, such as infrared light (IR) thermography, Raman spectroscopy, thermo reflectance, and luminescence thermometry.⁶ Of these, luminescence-based approaches have garnered significant attention due to their simplicity, high sensitivity, and exceptional spatial and temporal resolution. Recent studies have revealed that the ideal thermometer for optimal performance should possess two discriminable peaks to facilitate the development of ratiometric sensors. Such sensors capitalize on being independent of the concentration and inhomogeneity of the luminescent centers present in the material. Additionally, they help circumvent issues with alignment and optoelectronic drifts of the excitation source and detectors.⁷

Considerable research has been undertaken to develop and investigate innovative optical materials for their potential use as luminescence thermometers. These materials include quantum dots (QDs), polymeric and inorganic materials doped with lanthanide ions (Ln^{3+}), organic dyes, and hybrid materials.⁷⁻⁹ Organic dyes have emerged as a promising alternative for ratiometric thermometry due to

several advantages such as high sensitivity, low toxicity, and facile tunability of their emission properties via chemical modification. Dye-based ratiometric thermometry, an uncommon approach in the field of thermometry, relies on the ratio of intensities between specific emission bands. This innovative technique has found applications in bioimaging, food safety monitoring, and microscale temperature sensing.¹⁰⁻¹² It's important to note that, historically, dyes have predominantly functioned as single-band thermometers.¹³ Despite the challenges of issues like photobleaching and environmental interference that still need resolution, the emergence of ratiometric thermometry using dyes holds great promise for advancing temperature sensing across various fields.¹⁴



Scheme 4.2 Schematic illustration of the preparation of the C-PMO and CP-PMO and representation of the diketo/keto-enol tautomerism of curcumin.

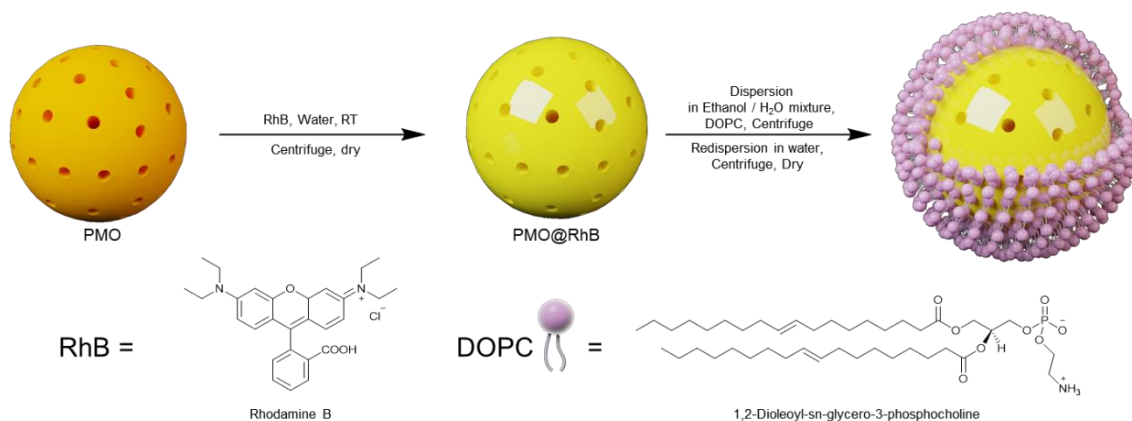
Among various materials investigated for ratiometric thermometry, the utilization of dual-emitting metal-organic frameworks (MOFs) doped with

fluorescent dyes has shown promising outcomes. The integration of dyes within host matrices such as MOFs present a pivotal enhancement, offering a shield against photobleaching and environmental perturbations. These ratiometric dual-emitting MOF@dye systems present an adaptable operational range and enhanced sensitivity, rendering them suitable for a spectrum of temperature sensing applications.^{5, 15-17} It's noteworthy to clarify that within this approach, the MOFs can serve as a host material contributing to one of the emission peaks,¹⁸ or alternatively, two distinct dyes can be embedded within a non-luminescent material.¹⁵ Despite these advantages, MOFs face challenges such as inherent instability and complexities in scalable production. Furthermore, the biocompatibility and degradation behavior of these materials are crucial, particularly for biomedical uses. As a result, periodic mesoporous organosilicas (PMOs) have emerged as an attractive alternative material for thermometry platforms. Periodic mesoporous organosilicas (PMOs) are a class of highly ordered porous materials first reported in 1999.¹⁹⁻²¹ PMOs are synthesized by the self-assembly of organoalkoxysilanes under mild conditions in the presence of surfactants or block copolymers. The resulting materials have mesoporous structures with uniform pore sizes, high surface areas, and tunable functionalities. Compared to traditional silica-based materials, PMOs exhibit superior stability, high thermal and chemical resistance, and low toxicity, making them attractive candidates for various applications in catalysis, drug delivery, imaging, and sensing.²²

In this study, we investigate the potential of PMOs and dyes as a ratiometric thermometry system that offers improved stability, sensitivity, and biocompatibility. Curcumin is a natural polyphenol and a well-known fluorescent dye, widely used in various biomedical and optical applications. In recent years, it has been incorporated into various matrix materials, including PMOs, due to its unique

properties such as antioxidant, anti-inflammatory, and fluorescent properties.²³ Therefore, curcumin functionalized PMOs (C-PMO) were developed through hydrolysis and co-condensation of curcumin-functionalized precursors with 1,2-bis(triethoxysilyl)ethane (BTESE) in the presence of cetyltrimethylammonium bromide (CTAB) surfactant. The resulting mesoporous curcumin nanoparticles (MCNs) exhibit pronounced autofluorescence and have been employed as a cargo delivery system in live-cell assays. These experiments utilize a supported lipid bilayer (SLB) to seal the pores, enabling the precise release of RhB into HeLa cells as a model cargo. Motivated by the capabilities of this C-PMO@RhB@LB system, we have adopted this composite for use as a ratiometric dual-emitting thermometer. Furthermore, we have introduced a novel curcumin-pyrazole functionalized precursor, leading to the creation of a modified curcumin-PMO (CP-PMO) system. This system features a more structurally rigid curcumin-pyrazole linkage, enhancing its potential applications.²⁴ The resulting PMOs showed highly temperature-dependent fluorescence properties. RhB was then encapsulated in the PMO pores to create a dual-emitting PMO@dye nanocomposite, which was further coated with a lipid bilayer (LB) to enhance biocompatibility and prevent dye leaching.²⁵ Among the previously reported dye-incorporated luminescent composites based on MOFs, C-PMO@RhB@LB and CP-PMO@RhB@LB demonstrate a very good maximum relative sensitivity (S_r) of up to 1.69 and 2.60 $\% \cdot K^{-1}$, respectively, within the physiological temperature range. Incorporating organic dyes into the PMO framework, as demonstrated in our work, enhances the stability of the dyes and reduces photobleaching. The novel dual-emitting PMO@dye system, especially with the addition of a lipid bilayer coating, offers a biocompatible and sensitive solution for temperature sensing. This advancement in ratiometric thermometry, leveraging the stability and biocompatibility of PMOs, represents a significant contribution to

the field, particularly in terms of reliability and applicability in various environments, including biomedical settings. This study enables the combination of luminescent host materials and RhB dyes, allowing for the future development of a range of ratiometric thermometers.¹⁵



Scheme 4.3 Schematic illustration of the preparation of the PMO@RhB@LB.

4.2 Experimental

4.2.1 Materials and Instrumentation

All chemicals were purchased from Sigma Aldrich, Fluorochem, Alfa Aesar, or TCI Europe and used without further purification.

Specifically, curcumin (from *curcuma longa*, powder) was purchased from Sigma-Aldrich with assay (HPLC, area%) $\geq 65\%$. Dulbecco's Modified Eagle Medium (DMEM), Fetal Bovine Serum (FBS), PrestoBlue™ HS (high sensitivity) Cell Viability Reagent, and Calcein-AM cell marker dye were purchased from ThermoFisher Scientific. Penicillin-Streptomycin was purchased from Sigma-Aldrich.

A Bruker D8 Advance diffractometer operating at 40kV/30mA using Cu-K α radiation ($\lambda=0.15418$ nm) equipped with a solid-state detector was employed to collect small-angle X-ray diffraction (SAXRD) patterns. Fourier transform infrared (FT-IR) spectroscopy measurements were conducted on a Thermo Nicolet 6700 FT-IR spectrometer using a KBr beam splitter and a nitrogen-cooled MCT-A detector.

Nitrogen adsorption data were acquired using a TriStar II gas analyzer at 77 K after degassing the samples under a vacuum at 393 K for 24 h. A Bruker 300 MHz AVANCE spectrometer was used for ^1H NMR, with CDCl_3 or DMSO-d_6 as the solvents. Elemental analysis (CHNS) was conducted using the Thermo Flash 2000 elemental analyzer, and V_2O_5 was used as a catalyst. Transmission electron microscopy (TEM) images were captured on a JEOL JEM-2200FS transmission electron microscope operated at 200 kV and equipped with a Cs corrector. All photoluminescence measurements were performed using an Edinburgh Instruments FLSP920 UV-vis-NIR spectrometer setup. The emission signals were detected using a Hamamatsu R928P photomultiplier tube, and a 450 W xenon lamp was employed as the steady-state excitation source. Luminescence decay profiles were measured using a 60 W pulsed xenon lamp. Temperature-dependent luminescent measurements were carried out using the Julabo refrigerated and heating F-25 circulator, which was attached to the sample holder and has a temperature range of 293 – 343 K with increments of 5 K. The TeSen program was utilized to process the temperature-dependent data.²⁶

4.2.2 Synthesis

4.2.2.1 Synthesis of 4-((1E,4Z,6E)-5-hydroxy-7-(3-methoxy-4-(((3-(triethoxysilyl) propyl) carbamoyl) oxy) phenyl)-3-oxohepta-1,4,6-trien-1-yl)-2-methoxyphenyl (3-(triethoxysilyl) propyl) carbamate (Curcumin-Si, 1b)

Curcumin-Si was synthesized according to a previously reported procedure.²³ In a three-necked flask, 25 mL of dry tetrahydrofuran (THF) was used to dissolve the (1E,6E)-1,7-bis (4-hydroxy-3-methoxyphenyl) hepta-1,6-diene-3,5-dione (Curcumin, 1.00 g, 2.71 mmol). Triethylamine (82.26 mg, 0.81 mmol) and (3-Isocyanatopropyl) triethoxysilane (IPTES, 2.68 g, 10.84 mmol) were then added while the mixture was being stirred, and it was then refluxed for 24 hours at 358 K with an Argon flow. After cooling to room temperature, the reaction mixture was filtered and washed

with ethyl acetate. Then, the filtrate was evaporated. The residue was purified by silica gel column chromatography (eluent: 65 v% ethyl acetate, 33 v% petroleum ether, 2 v% triethylamine) to give Curcumin-Si as an orange oil. The resulting product was dried for 12 hours under a high vacuum before being used. Yield: 67%. ¹H NMR (300 MHz, DMSO-d₆) δ 7.76 (t, J = 5.8 Hz, 2H), 7.65 (d, J = 15.9 Hz, 2H), 7.48 (d, J = 1.8 Hz, 2H), 7.30 (dd, J = 8.3, 1.9 Hz, 2H), 7.12 (d, J = 8.2 Hz, 2H), 6.97 (d, J = 15.9 Hz, 2H), 3.83 – 3.64 (m, 12H), 3.38 – 3.27 (m, 2H), 1.16 (td, J = 7.0, 2.8 Hz, 18H), 0.66 – 0.53 (m, 2H).

4.2.2.2 Synthesis of 4,4'-((1E,1'E)-(1H-pyrazole-3,5-diyl) bis(ethene-2,1-diyl)) bis(2-methoxyphenol) (Curcumin-Pyrazole Analog, 1c)

In the procedure used by Ahsan et al.,²⁷ curcumin (200 mg, 0.54 mmol, 1 equiv) and hydrazine hydrate (5 equiv) were dissolved in glacial acetic acid (10 mL). The solvent was then removed in a vacuum after the solution had refluxed for 8 hours. The residue was washed with water after being dissolved in ethyl acetate. The organic portion was collected, dried over sodium sulfate, and concentrated in a vacuum. Column chromatography (eluent: 65 v% ethyl acetate, 33 v% petroleum ether, 2 v% triethylamine) was used to purify the crude product. Yield: 82% ¹H NMR (300 MHz, DMSO-d₆) δ 12.72 (s, 1H), 9.15 (s, 2H), 7.14 (d, J = 1.9 Hz, 2H), 7.04 (d, J = 16.5 Hz, 2H), 7.01 – 6.69 (m, 4H), 6.61 (s, 1H), 3.83 (s, 6H).

4.2.2.3 Synthesis of 2,2'-(((1E,1'E)-(1H-pyrazole-3,5-diyl) bis(ethene-2,1-diyl)) bis(2-methoxy-4,1-phenylene))bis(N-(3-(triethoxysilyl)propyl)acetamide) (Curcumin-Pyrazole-Si, 1d)

To synthesize the novel Curcumin-Pyrazole-Si linker, in the analogous method used by Datz et al.,²³ in a three-necked flask, 25 mL of dry THF was used to dissolve the curcumin-pyrazole analog (1.00 g, 2.75 mmol). Triethylamine (83.48 mg, 0.83 mmol) and (3-Isocyanatopropyl) triethoxysilane (IPTES, 2.72 g, 11 mmol) were then

added while the mixture was being stirred, and it was then refluxed for 24 hours at 358 K with an argon flow. After cooling to room temperature, the reaction mixture was filtered and washed with ethyl acetate. Then, the filtrate was evaporated. The residue was purified by silica gel column chromatography (eluent: 65 v% ethyl acetate, 33 v% petroleum ether, 2 v% triethylamine) to give Curcumin-Si as a dark orange oil. The resulting product was dried for 12 hours under a high vacuum before being used. Yield: 61% ¹H NMR (300 MHz, DMSO-d₆) δ 7.43 – 7.02 (m, 10H), 3.99 (dq, J = 21.0, 7.1 Hz, 12H), 3.87 – 3.65 (m, 6H), 3.33 (s, 2H), 3.03 (q, J = 6.7 Hz, 2H), 2.93 (d, J = 6.9 Hz, 2H), 1.99 (s, 2H), 1.56 (dt, J = 23.4, 8.3 Hz, 2H), 1.16 (qd, J = 7.1, 3.1 Hz, 18H), 0.55 (ddd, J = 23.5, 11.9, 6.1 Hz, 2H).

4.2.2.4 Synthesis of mesoporous Curcumin-PMO (C-PMO) nanoparticles and Curcumin-Pyrazole PMO(CP-PMO)

Following a modified literature procedure, in a two-step sol-gel reaction, cetyl trimethyl-ammonium bromide (CTAB, 0.96 mmol, 350 mg) was dissolved in a solution of 5.83 g water in a 20 ml round bottom flask. The mixture was then stirred at 353 K for 30 min after adding of 3.63 mL of NH₄OH solution (25%). 120 mg of curcumin-Si (0.137 mmol) / 60 mg of curcumin-pyrazole-Si (0.52 mmol) and bis(triethoxysilyl)ethane (BTESE) in 10%:90% / 38%:62% ratios, respectively, were mixed with 1 mL of ethanol in a vial. This precursor solution was promptly injected into the stirred aqueous surfactant solution. A yellow suspension was formed, stirring for an additional two hours at 353 K. The organic surfactant was extracted by heating the sample under reflux at 363 K for 1 hour in a solution of 2 g ammonium nitrate and 100 mL ethanol. The sample was then redispersed in ethanol, heated under reflux for 45 minutes at 363 K in a solution of 100 mL ethanol, and centrifuged for 10 minutes at 8000 rpm. It was then dried overnight in an oven at 393 K.

4.2.2.5 Preparation of PMO@dye

A solution of RhB in distilled water was prepared in a glass vial (Table S4.1). Next, 2 mL of this solution was taken and added to a new vial containing 10 mg of dry PMO powder. The mixture was first redispersed using ultrasounds for 5 minutes and then stirred for 48 hours at room temperature and centrifuged for 10 minutes at 8000 rpm. It was then dried overnight in an oven at 353 K.

4.2.2.6 Preparation of PMO@dye@LB (hybrid nanocomposites with lipid bilayer)

Following the reported procedure of the preparation of the lipid bilayer around the hybrid nanocomposites,²⁵ 1,2-dioleoyl-sn-glycero-3-phosphocholine (DOPC) was utilized. 5 mg of either C-PMO@RhB or CP-PMO@RhB was dispersed in 100 μ L of 3.5 mM DOPC solution in a mixture of H₂O and EtOH (60/40). Then, 900 μ L distilled H₂O was quickly added and mixed. The addition of extra water resulted in precipitation of the lipid molecules, which were expected to cover the surface of the hybrid nanocomposite with a lipid layer. The PMO@dye@LB was purified by centrifugation and redispersion in a small amount of H₂O, and this process was repeated to ensure complete purification of the material. It was then dried overnight in an oven at 353 K.

4.2.3 Cytotoxicity test

4.2.3.1 Cell cultures:

For the cell viability assays, healthy Normal Human Dermal Fibroblast (NHDF) cells were cultivated using a cell growth medium solution (DMEM + 10% FBS + 1% Pen-Strep) and were subsequently seeded in 96-well plates with a seeding concentration of 5,000 cells/well upon reaching 80-90% confluency during early culture passage stages (P2-P5). The cell plates were incubated for 24 hours in the dark at 37 °C and 5% CO₂.

4.2.3.2 Cell viability assay:

Cytotoxicity tests were conducted on a series of sample concentrations: 0, 0.028, 0.056, 0.278, 0.556, 1.111, 1.667, and 2.778 mg/mL (or 0, 0.005, 0.01, 0.05, 0.1, 0.2, 0.3, and 0.5 mg/well respectively), to evaluate the effect of the prepared materials on *in vitro* cultured healthy NHDF cells. The obtained results summarize the data readout from five technical replicates per tested concentration per sample.

The compatibility of each of the samples with the *in vitro* cultured adherent healthy NHDF cells was investigated and quantified using the PrestoBlue™ HS cell viability assay *via* fluorescence spectroscopy measurements with $\lambda_{exc} = 560$ nm and $\lambda_{em} = 635$ nm. The samples (as dry powders) were suspended in the cell growth medium solution to prepare the respective stock solutions. To obtain uniform dispersions and eliminate particle agglomerates, the stock solutions were vortexed for 1 minute and ultrasonicated for 10 minutes before addition/dilution in the appropriate concentration to the wells containing previously seeded and incubated cells. The cytotoxic effect of the as-prepared materials was investigated in a series of sample concentrations ranging from 0 - 2.778 mg/mL, tested on five technical replicates per concentration. Upon sample addition, the cell plates were incubated for 24 hours in the dark at 37 °C and 5% CO₂. The following day, 20 µL of the PrestoBlue™ HS reagent was added to all wells and the plates were again incubated in the dark for 4 hours at 37 °C and 5% CO₂. Negative controls contained seeded cells, cell growth medium, and PrestoBlue™ HS cell viability reagent, while positive controls or PB-blanks contained PrestoBlue™ HS cell viability reagent and cell growth medium solution. The fluorescence emission of the cell plates was measured on a Tecan spectrophotometer equipped with a microplate reader.

The data readout is normalized with respect to the averaged negative controls in the following way:

$$\text{Cell viability/\%} = \frac{[FI(\text{technical replicate}) - FI(\text{PB blanks average})]}{[FI(\text{control average}) - FI(\text{PB blanks average})]} \times 100$$

where **FI** stands for fluorescence emission intensity at 635 nm; a **technical replicate** is a technically repeated sample concentration containing seeded cells, cell growth medium solution, and PrestoBlue™ HS cell viability reagent; **(negative) controls** represent plate wells containing seeded cells, cell growth medium solution, and PrestoBlue™ HS cell viability reagent; and **PB-blanks** represent plate wells containing cell growth medium solution and PrestoBlue™ HS cell viability reagent; all equalized to the same final volume per well by cell growth medium solution.

Simultaneously, parallel technical replicates were prepared for the widefield fluorescence microscopy imaging under identical treatment, replacing the PrestoBlue™ HS cell viability reagent with Calcein-AM fluorescent cell marker dye with a concentration of 0.3 μL/well or a final plate well concentration of 1.5 μM. After dye addition, the cell plates were incubated for 20 minutes in the dark at 37 °C and 5% CO₂. Cell visualization was performed using a Green Fluorescent Protein (GFP) long-pass filter on a Nikon Ti widefield microscope transmitting all emitted wavelengths ≥ 500 nm, under excitation of 470 nm.

Table 4.4 Textural properties of prepared C-PMO and CP-PMO.

Material	S _{BET} (m ² g ⁻¹)	Pore diameter ^a (nm)	Total pore volume (cm ³ g ⁻¹)
C-PMO	1254	3.2	0.63
CP-PMO	1149	3.2	0.59
C-PMO@RhB4@LB	721	3.2	0.33
CP-PMO@RhB1@LB	806	3.1	0.37

^acalculated from NLDFT, N2 at 77K, using the kernel of silica cylindrical pore, adsorption branch.

4.3 Results and discussion

4.3.1 Structural characteristics of PMO@dye@LB

Precursor preparation was the first step in the development of the nanomaterials. Compound **curcumin-Si (1b)** had been synthesized utilizing **IPTES** for silylation on **curcumin (1a)**. **Curcumin (1a)** was converted into **curcumin-Pyrazole**

(1c) analog by the addition of hydrazine, then **curcumin-pyrazole-Si** (1d) was produced using further reacting compound **curcumin-pyrazole** (1c) with IPTES (Scheme 4.1). Using a co-condensation technique with **BTESE**, **curcumin-Si** or **curcumin-pyrazole-Si** was finally covalently incorporated into the PMO frameworks.

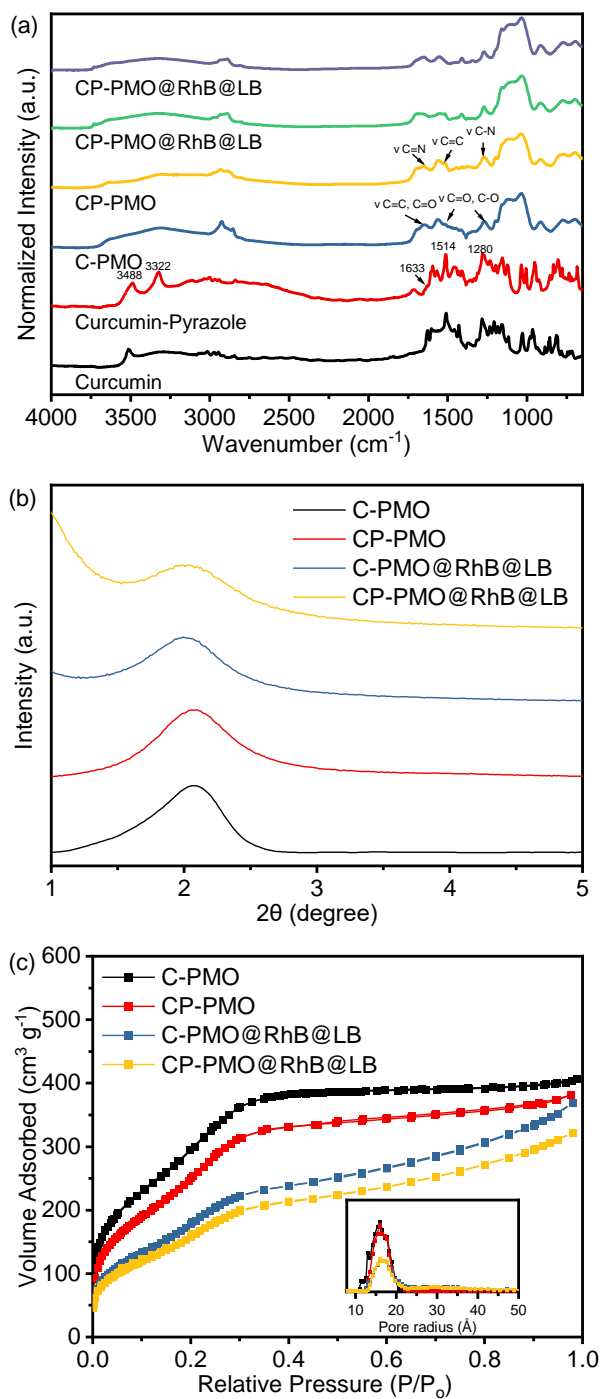


Figure 4.1 (a) FTIR spectra of PMO@RhB@LB; (b) PXRD patterns of PMOs@RhB@LB; (c) N₂ adsorption-desorption isotherms and pore size distributions of PMO@RhB@LB.

According to earlier research by Joseph et al. and Muddassar et al. on the vibrational spectra of curcumin and curcumin-pyrazole, respectively,^{28, 29} FT-IR spectra were used to determine the synthesis of **1c** and the formation of C-PMO and CP-PMO (Figure 4.1a). Firstly, when compared to **1a**, several typical variations in the **1c** spectrum may be seen. The overlap of C-OH and C-NH bond vibration may cause a strong, and broad peak at 3488/3322 cm^{-1} . For **1c**, because of the C=N stretching frequencies, a band can be seen at 1633 cm^{-1} .

Moreover, stretching vibrations of the C=C bonds were represented by a strong, intense band at 1514 cm^{-1} , while a second, similar band at 1280 cm^{-1} represented the C-N bond. Secondly, a new band at 1041 cm^{-1} represented the stretching vibrations of the Si-O-Si frameworks. Thirdly, the characteristic absorption peaks of the **1a** ($\nu_{\text{C=C, C=O}} = 1650 \text{ cm}^{-1}$, $\nu_{\text{C=O, C-O}} = 1511, 1272 \text{ cm}^{-1}$) and **1c** moieties ($\nu_{\text{C=N}} = 1650 \text{ cm}^{-1}$, $\nu_{\text{C=C}} = 1513 \text{ cm}^{-1}$, $\nu_{\text{C-N}} = 1276 \text{ cm}^{-1}$) remained after removal of the surfactant (CTAB), with showing the stable immobilization of curcumin and curcumin-pyrazole units into the silica framework. The FTIR spectra of the samples containing RhB showed negligible variations, and the distinctive absorption peaks of RhB could not be identified in the spectra. This is because the mass fraction of RhB in the material is considerably lower than that of the matrix materials. As a result, the IR absorptions of RhB have been concealed by the matrix materials, particularly when the characteristic absorption peaks are close to those of the matrix.³⁰ SAXRD and N_2 adsorption measurements were carried out to investigate the structural response of the materials to functionalization. The SAXRD profiles of the surfactant-free C-PMO and CP-PMO were shown in Figure 4.1b. The diffraction peak was observed at around $2\theta = 2^\circ$ for these two samples, indicative of a mesoscopically ordered structure.³¹ Figure 4.1c depicts the N_2 adsorption-desorption isotherm of these two materials. By comparing the isotherm of C-PMO with that of CP-PMO, it was

observed that the shape remained the same. Both materials had the type IV isotherm, indicating that the ordered mesoporous structure had successfully been formed.³² Brunauer–Emmett–Teller (BET) surface area for C-PMO and CP-PMO were $1254 \text{ m}^2 \text{ g}^{-1}$ and $1149 \text{ m}^2 \text{ g}^{-1}$, respectively, and the total pore volumes were $0.63 \text{ cm}^3 \text{ g}^{-1}$ and $0.59 \text{ cm}^3 \text{ g}^{-1}$, respectively. In addition, the pore size of PMOs calculated using the non-local density functional theory (NLDFT) method were both 3.2 nm (Table 4.1). Therefore, the resulting material's mesostructure is coincident with the results of XRD patterns. Additionally, the confirmation of a lipid bilayer on the surface of PMO particles was carried out using BET analysis. After the introduction of dyes inside the pores of PMO, the pristine C-PMO and CP-PMO particles were coated with a lipid bilayer (Scheme 4.2), resulting in a reduction in surface area to 901 and 979 m^2/g , respectively. The observed reduction in surface area implies that the lipid bilayer, along with the incorporated dyes, partially obstructs the pores of the PMO particles, while also wrapping around the particle structure. To confirm the feasibility of the sensing application, we compared the particle morphologies of these two materials by utilizing TEM. As shown in Figure 4.2b and 4.2d, both possess representative spheres with an average diameter of 69 ± 13 and 153 ± 11 nm, respectively. Regarding the TEM observations, we recognize the noted differences in particle size and aggregation between CP-PMO and C-PMO. This discrepancy can indeed be attributed to the differing chemical interactions and steric hindrance presented by the pyrazole moiety in CP-PMO, which may affect particle nucleation and growth. Besides higher concentration in precursors ratio of CP-PMO, the distinct interactions of functional groups in C-PMO and CP-PMO with solvents, surfactant can modulate the kinetics of polymerization or condensation reactions, impacting particle nucleation and growth.³³

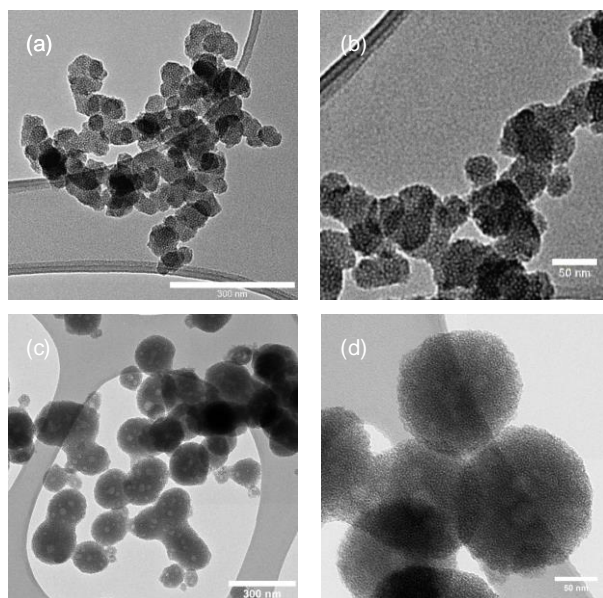


Figure 4.2 TEM images of (a) (b) C-PMO and (c) (d) CP-PMO.

4.3.2 Temperature-Related Fluorescence of PMO@dye@LB

4.3.2.1 Fluorescence of the prepared PMO@dye@LB.

Figure 4.3 presents the solid-state excitation and emission spectra of PMOs at room temperature. The excitation bands of the materials are broad, spanning from 250 nm to over 480 nm. All prepared materials exhibit strong visible emission, which can be observed with the naked eye (Figure S4.3a).

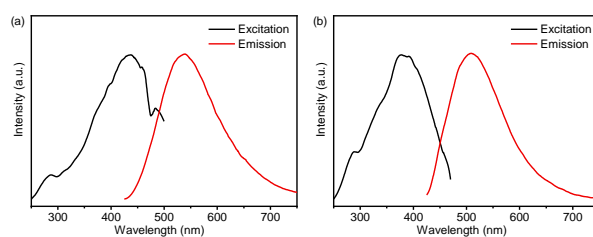


Figure 4.3 Combined RT excitation-emission spectrum of the (a) C-PMO and (b) CP-PMO in water (excited at 417 nm and observed at 525 nm).

The photoluminescence properties of the C-PMO and CP-PMO material were measured at room temperature, and the emission band was acquired by exciting at 417 nm. The C-PMO material emits over a broad range of wavelengths, ranging from 430 to 750 nm, with a peak maximum at 539 nm. The emission is related to the π -

π^* electron transition of the curcumin linker.²³ Compared similarly, the CP-PMO material shows a slight blue-shifted spectrum and exhibits a broad emission band ranging from 430 to 750 nm, with a peak maximum at 509 nm, which may be attributed to the change in the rigidity of the curcumin-pyrazole linker. The fluorescence emission spectrum of RhB in water exhibits a prominent emission peak at approximately 641 nm when excited at 385 nm, as shown in Figure S4.4a. Additionally, its UV-Vis absorption spectrum shows broad absorbance in the range of 450-600 nm (Figure S4.4b). Notably, there is a spectral overlap between the emission spectrum of PMOs and the absorption spectrum of RhB, as depicted in Figure S4.4b. This indicates the possibility of efficient energy transfer from PMO to RhB upon excitation at 417 nm. Further insight is offered through Figure S4.5, which elucidates the luminescence decay profiles of the individual emissions within the PMOs.³⁴ It is notable that the observed decay times for the curcumin functionalized PMOs appear to be extremely prolonged, comparing with existing literature.³⁵ The photoluminescence quantum yield of curcumin exhibits low values across various solvents, with a pronounced decrease observed in aqueous environments. Consequently, the fluorescence lifetime of curcumin in liquid phase at ambient temperature is notably short, typically less than 1 nanosecond.³⁶ The shortened fluorescence lifetime of such dyes in the picosecond range is hypothesized to stem from internal barrierless rotation within the excited state.³⁷ Given that rotational motions around double bonds are known to decrease fluorescence lifetime, it follows that restricting such rotations—by embedding the fluorophores within a rigid matrix (PMOs), reducing ambient temperature, or stabilizing the molecule's flexible segments—would mitigate nonradiative decay channels, thereby enhancing both fluorescence intensity and lifetime.^{38, 39} These profiles effectively demonstrate

a decrease in decay time of PMO's emission as the quantity of added RhB solution increases.

To enhance the performance of PMO@dye@LB, various composites of PMO@dye@LB with differing dye concentrations were synthesized, adhering to the ratios delineated in Table S4.1. Figure S4.6 and S4.7 present the emission spectra of PMO@dye@LB with different dye contents dispersed in water at room temperature. As anticipated, the PMO@dye@LB composite exhibits simultaneous emission profiles of the rigidified linker and RhB under the same conditions as PMO. The emission peak profile of RhB in PMOs (596 nm) is blue-shifted compared to that of the RhB water solution (641 nm) and is attributed to pore confinement of RhB within PMO due to strong interaction between curcumin/curcumin-pyrazole linker of PMO and RhB dye.⁵ It also suggests that RhB is uniformly accommodated as isolated molecules in the pores of PMO, avoiding the formation of excimers or aggregates in the solid phase.¹⁷ By decreasing the RhB content in the pores of the host framework, the emission color of PMO@dye@LB can be tuned, with the color depending on the combination of emissions from PMO and RhB, as well as the energy transfer process between the two. With decreasing RhB content, the orange emission (596 nm) of RhB is attenuated while the emission of PMOs is enhanced, resulting in a color change from orange to yellow. The observed blue shift in the emission peak of RhB with decreasing dye concentration is related to the confinement effect within the PMO's porous structure. This effect limits the RhB molecules' spatial orientation and their potential to aggregate. As RhB concentration decreases, spatial confinement becomes more significant, leading to an increased presence of isolated RhB molecules. These isolated molecules have emission characteristics distinct from those in aggregated states, causing the noted blue shift.⁴⁰ The CIE chromaticity

diagram for PMO@dye@LB was depicted to show the color changes from orange to red (Figure S4.8).

4.3.2.2 Ratiometric temperature sensing properties of PMO@dye@LB

To assess the potential of PMO@dye@LB as a ratiometric thermometer, a detailed investigation was conducted on its temperature-dependent photoluminescent properties. Initially, the host PMOs were excited at a wavelength of 417 nm, and the emission spectra were analyzed across a temperature range of 293 to 323 K (refer to Figure S4.9). A notable decrease in luminescence was observed for both the curcumin and curcumin-pyrazole linkers with increasing temperature, showing reductions of 0.74% and 1.29% per K, respectively (as depicted in Figure S4.9). This decline in fluorescence can be attributed to the thermal activation of nonradiative decay pathways and relaxation.¹⁸ Given the complexity of these processes and their dependence on the molecular structure and environment, pointing out the exact pathways without extensive additional studies can be challenging. Our current analysis was based on observed trends consistent with the general understanding of thermally induced nonradiative decay in similar systems. Additionally, Figure S4.10 presents the luminescence decay profiles for these emissions at varying temperatures, highlighting their temperature-responsive characteristics. The luminescence lifetime, which signifies the average duration of the excited state, is observed to decrease with rising temperatures due to the increased rate of nonradiative decay.

Subsequently, the temperature-dependent emission spectra of PMO@dye@LB were examined under identical conditions, extending the temperature range to 343 K (as shown in Figures S3b, S11, and S12). The intricate temperature-dependent changes in various emission bands are succinctly quantified by stating percentage changes per Kelvin (% K⁻¹). The intensity of the curcumin linker in C-PMO@RhB@LB

was found to decrease by 0.43% per Kelvin over the range of 293 to 343 K (Figure S4.11), a rate significantly higher than that in pristine C-PMO (0.74% K⁻¹). Conversely, the peak intensity of the curcumin-pyrazole linker in CP-PMO@RhB@LB displayed a decrease of 1.18% K⁻¹ (Figure S4.12), marginally lower than its rate in CP-PMO (1.29% K⁻¹). Detailed analysis of these materials and their CIE coordinates at different temperatures is presented in Figure S4.13. Within the C-PMO framework, the emission intensity of the curcumin linker remains stable with temperature increase, indicating minimal impact from thermal activation of nonradiative decay or relaxation processes. However, Figure S4.11 demonstrates that the luminescence of RhB is more susceptible to temperature-induced changes compared to the curcumin linker. It is acknowledged that rhodamine B (RhB) is highly sensitive to temperature variations.¹⁵ In contrast, the emission from the curcumin-pyrazole linker in CP-PMO@RhB@LB shows a marked intensity decline with increasing temperature, even more pronounced than the decrease observed for RhB (Figure S4.12). This suggests that the interaction between the CP-PMO host and the dye enhances the temperature sensitivity of the CP-PMO compared to RhB. Based on their clear intensity changing trends between curcumin PMO and RhB, we specifically focused on the spectra of C-PMO@RhB4@LB and CP-PMO@RhB1@LB. Figure 4.4 illustrates the temperature dependence by displaying the normalized intensities of their corresponding emissions. The PMO@dye composites effectively retain the emissions of both RhB and organic linkers, which exhibit distinct thermal dependencies. As a result, the intensity ratio between these emissions is highly sensitive to temperature, providing a self-calibrated thermometric parameter for accurate temperature sensing.

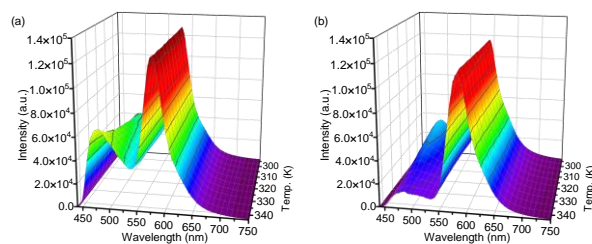


Figure 4.4 Temperature-dependent normalized emission spectra of (a) C-PMO@RhB4@LB and (b)CP-PMO@RhB1@LB dispersed in water recorded from 293.15 to 343.15 K, when excited at 417 nm.

Ratiometric luminescence temperature measurement involves utilizing the emission intensities of two distinct luminescence centers. This measurement technique utilizes an intensity ratio parameter ($\Delta = I_{\text{pro}}/I_{\text{ref}}$), which represents the emission intensity of the probe (I_{pro}) relative to that of the reference (I_{ref}) in the PMO@RhB@LB system. The temperature dependence of the parameter Δ was analyzed using the well-known Mott–Seitz model,^{41, 42} which takes into account the interplay between radiative and nonradiative decay processes of each emitting center. In summary, the temperature dependence of Δ can be described by eq 1.

$$\Delta = \frac{\Delta_0}{1 + \alpha \exp(-\Delta E/k_B T)} \quad (1)$$

where Δ_0 is the ratiometric parameter Δ at $T = 0$ K, the parameter α represents the ratio between the nonradiative and radiative probabilities of the deactivation channel. k_B refers to the Boltzmann constant, and ΔE represents the activation energy of the nonradiative process (thermal quenching). The differential temperature sensitivity of C-PMO and RhB leads us to designate the emission intensity of C-PMO as I_{ref} , reflecting its lower temperature responsiveness compared to RhB. Conversely, due to CP-PMO's heightened temperature sensitivity, surpassing that of RhB, the emission intensity of CP-PMO is denoted as I_{pro} . In accordance with eq 1, the experimental values of the parameters Δ for C-PMO@RhB4@LB and CP-PMO@RhB1@LB can be well fitted using the eq 1 with the correlation coefficient (R^2) of 0.997 and 0.992, respectively (Table S4.2).

The results obtained are in alignment with the predictions of equation 1, indicating the presence of a single pathway for thermally induced non-radiative deactivation in both compounds. The temperature calibration curves (depicted as red solid lines) in Figure 4.5a and 4.5c demonstrate the nature of the thermally activated channel in C-PMO@RhB4@LB and CP-PMO@RhB1@LB, respectively. The fitted α value for CP-PMO@RhB1@LB is higher than that of C-PMO@RhB4@LB, indicating a stronger nonradiative deactivation in the latter composite. Of particular importance, the S-shaped fitting of the calibration curves yielded two activation energies: $\Delta E_{C-PMO} = 3065.4 \text{ cm}^{-1}$ for C-PMO@RhB4@LB and $\Delta E_{CP-PMO} = 2936.5 \text{ cm}^{-1}$ for CP-PMO@RhB1@LB. A smaller activation energy typically indicates that the temperature-dependent process, such as a nonradiative decay pathway or an energy transfer mechanism, occurs more readily with changes in temperature. This means that the transition between different emitting states or energy levels within the material happens more easily, leading to a more pronounced change in the intensity or ratio of emission bands used for temperature sensing.¹⁸ In conclusion, it indicates that the curcumin-pyrazole linker is more sensitive to temperature changes compared to curcumin linker, even higher than RhB in CP-PMO@RhB@LB. These findings align with the earlier assessment of the temperature dependence of the luminescent intensity and lifetime.

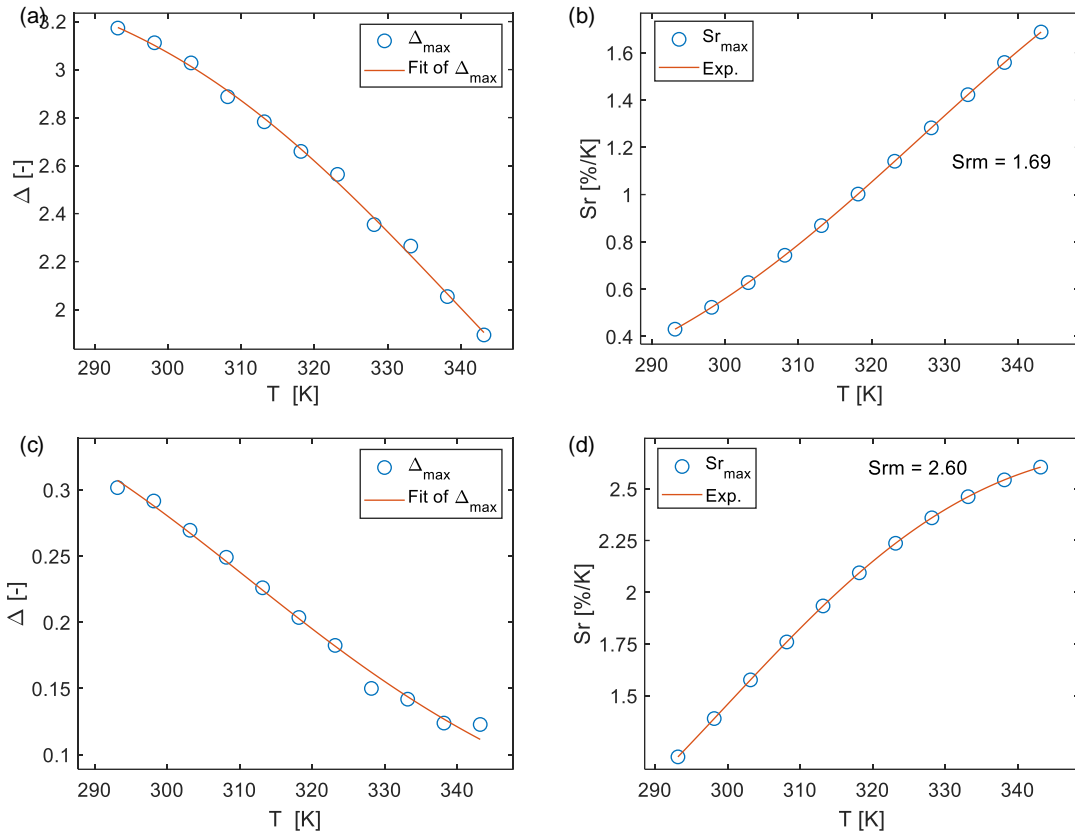


Figure 4.5 (a)(c) Delta calibration curve for C-PMO@RhB4@LB and CP-PMO@RhB4@LB when eq 1 is employed. The points show the experimental Δ parameters and the solid line shows the best fit of experimental points. (b)(d) S_r values at varying temperatures (293-343 K). The data is obtained based on the peak maxima.

The relative thermal sensitivity (S_r) is a commonly used figure of merit to evaluate and compare the performance of different dual-emitting thermometers.⁴² By comparing the S_r values of various thermometers, we can assess their effectiveness in accurately measuring temperature variations. Higher S_r values indicate a higher sensitivity to temperature changes, making a thermometer more suitable for precise temperature measurements. It can be defined as

$$S_r = \frac{1}{\Delta} \left| \frac{\partial \Delta}{\partial T} \right| \quad (2)$$

where Δ is the ratiometric parameter of our composites and T is the absolute temperature. In accordance with the aforementioned definition, the relative thermal sensitivity (S_r) values of C-PMO@RhB4@LB and CP-PMO@RhB1@LB were

calculated and presented in Figure 4.5. It can be observed that within the range of 293 to 343 K, the maximum S_r values for C-PMO@RhB4@LB and CP-PMO@RhB1@LB were determined to be 1.69% K⁻¹ and 2.60% K⁻¹, respectively. It is evident that the composite CP-PMO@RhB1@LB exhibit superior relative sensitivities compared to its respective counterpart, C-PMO@RhB4@LB. The enhanced sensitivity of CP-PMO@RhB1@LB can be attributed to the stronger interaction and reduced nonradiative decays between RhB and the CP-PMO framework. Since it is a novel concept to utilize PMO@dye composite as ratiometric thermometry system in biomedical applications, there are few reported analogous compounds for comparison. Within the spectrum of dye-embedded MOF-derived luminescent materials, our studies reveal that C-PMO@RhB4@LB and CP-PMO@RhB1@LB stand out for their good maximum relative sensitivity (S_{rm}) within the physiological temperature range, as detailed in Table S4.3. Notably, these composites exhibit enhanced sensitivities at elevated temperatures, underscoring their promising applicability for temperature sensing in higher temperature environments. Consequently, the RhB-doped PMO composites emerge as candidates for precise temperature monitoring applications under such conditions.

The temperature resolution (δT) is a crucial parameter for evaluating luminescent thermometers and can be defined as follows:⁴³

$$\delta T = \frac{1}{S_r} \frac{\delta \Delta}{\Delta} \quad (3)$$

where $\delta \Delta / \Delta$ is the relative standard deviation of the Δ .⁴⁴ The temperature uncertainty (δT) of the composites were calculated using eq 3, and the results indicate that it remains below 0.07 K across the entire temperature range under investigation (Figure S4.14).

To assess the reversibility of the luminescent thermometer, a series of temperature-dependent emission measurements were conducted over four consecutive cycles within the temperature range of 293 to 343K. The results demonstrate that the emission intensity ratio remains nearly constant at various temperatures throughout each cycle (Figure S4.15), indicating the excellent reversibility of the system.³

4.3.3 PrestoBlue™ HS cell viability assay conducted on NHDF cell line.

From the obtained graph (Figure 4.6), it can be observed that overall, all three materials generally manifest a slight cytotoxic effect across the investigated concentration range. The C-PMO and the C-PMO@RhB@LB materials are negligibly toxic to the NHDF cells in the entire investigated concentration range, especially in the first portion of the range (up to a concentration of 1.667 mg/mL which includes and coincides with the targeted values that may be readily and successfully exploited for the thermometric measurements (proposed in the literature as a maximum of 1 mg/mL). Increasing the concentration of C-PMO from 1.667 mg/mL to 2.778 mg/mL decreases the NHDF cell viability from ~88 to 60%, therefore it can be concluded that C-PMO is significantly toxic to the cells only at the highest tested concentration, which exceeds practical concentration limits for thermometry applications. However, for the C-PMO@RhB@LB material, even at the highest tested concentration the cell viability is determined to be ~80%, displaying that compared to the C-PMO, the C-PMO@RhB@LB material maintains non-toxicity in a wider range, indicating that incorporation of the lipid bilayer has a favorable influence contributing to the enhanced compatibility of the material with the healthy human fibroblast cells.

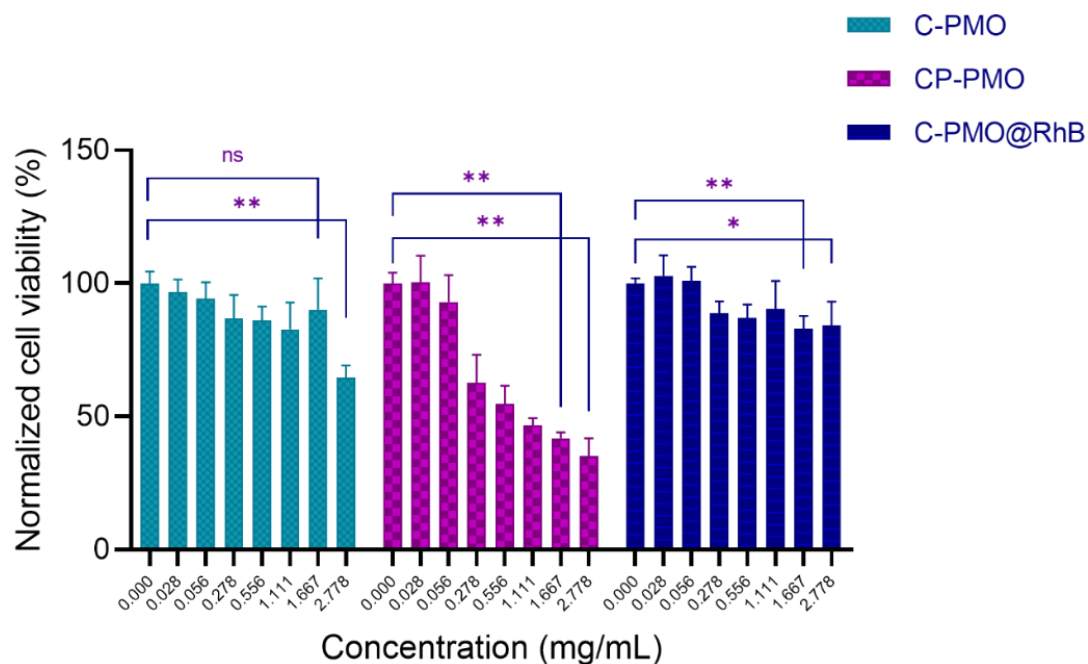


Figure 4.6 Cumulative grouped bar graph (mean + SD) of cytotoxicity test results obtained for the three tested materials. A nonparametric statistical analysis was conducted, employing the Mann-Whitney-Wilcoxon test to investigate for significant differences between the control median and any other concentration group median of a tested sample, where * represents $p < 0.05$ and ** represents $p < 0.01$, and ns stands for statistically non-significant differences.

The widefield microscopy images (Figure 4.7, Figure S4.16) also show the increasing aggregation of the sample in the same range of increasing sample concentration, making the spindle-shaped morphology of the NHDF cells less visible to entirely undetectable at the highest tested concentration because of the topical fluorescence emission from the aggregated particles themselves and not because of complete cell death (Figure S4.16). Because the particles fluoresce inherently, their emission is also detected on the widefield microscope, while the excitation wavelength of the cell labeling dye and the PMOs coincide. Since the stain emission readout for the cytotoxicity and microscopy replicates is collected at different emission wavelengths (635 nm and ≥ 500 nm respectively) it can be concluded that there are still viable cells in the wells treated with the highest concentration even though they are not visually detectable in the microscopy images since the

aggregations obstruct the visual field of the microscope. This can be attributed to the relatively high concentrations of sample added in a suspension to the seeded cells. For the CP-PMO material, the toxic effect is slightly more pronounced with cell viability decreasing from ~60 to ~30% in the concentration range from 0.278 to 2.778 mg/mL, resulting overall in a very steep toxicity slope at the higher portion of the concentration range. The fluorescence microscopy images show less aggregation for the CP-PMO sample as compared to the other two samples at the same concentrations, making it evident that the cell viability does decrease going from 0.278 to 2.778 mg/mL, depicted visually too (Figure S4.16). To conclude, comparatively, the C-PMO@RhB@LB material is the least toxic among the three tested, with cell viability decreasing down to ~80% for the highest tested concentration of 2.778 mg/mL even though some sample aggregation is evident at higher concentrations. This highlights the suitability and beneficial compatibility of this material to be exploited successfully in thermometry applications in optimal doses. The statistically significant differences between the control mean and the means of the other columns (shown on the bar graph) could be due to the notable aggregates with different dimensions present in the plate wells at much higher concentrations of the materials. Additionally, it's worth noting the comparative lower toxicity and higher applicability of the C-PMO@RhB@LB system in bioapplications, highlighting its potential as a safer alternative for biomedical use. While acknowledging that the CP-PMO@RhB@LB system remains a viable option for other applications, the selection between these systems should be guided by the specific requirements of the application in question, balancing factors such as toxicity, biocompatibility, and functional performance.

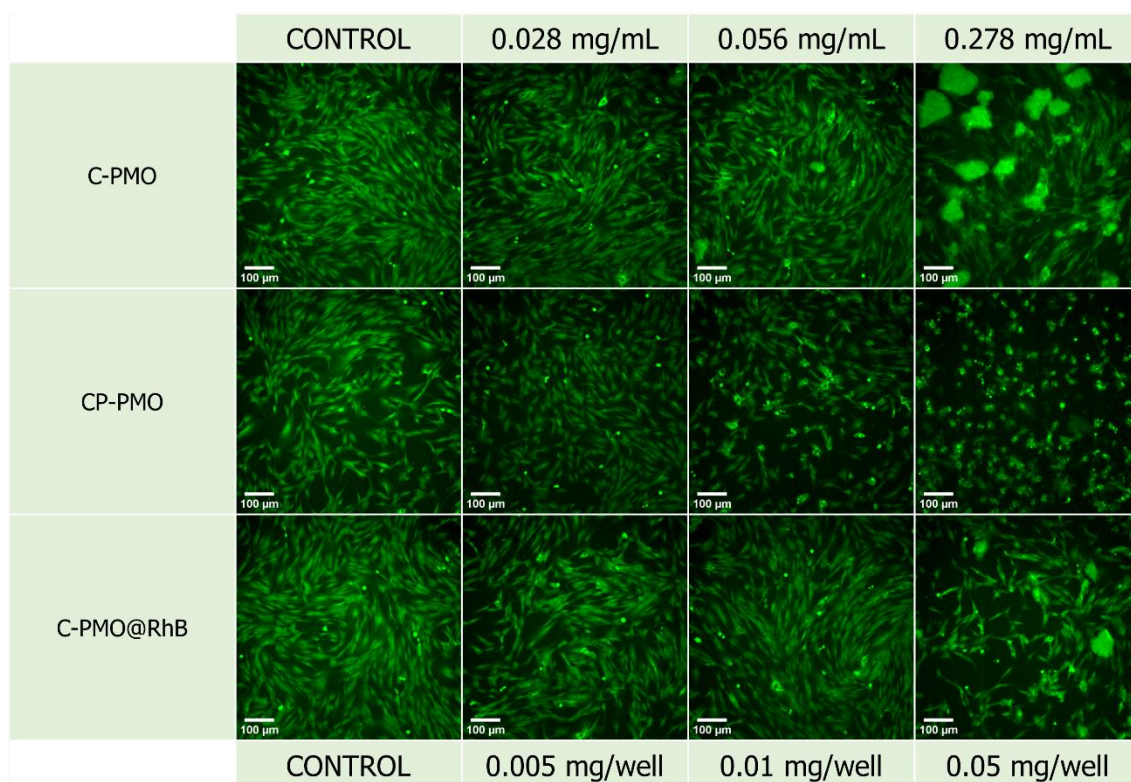


Figure 4.7 Fluorescence microscopy images of the technical replicates with stained NHDF cells for the three samples (C-PMO, CP-PMO, C-PMO@RhB@LB). Calcein-AM was used as the cell stain at a final well concentration of 1.5 μ M. All scale bars are set to 100 μ m.

Here, we underscore the advantages of utilizing RhB dye-incorporated curcumin PMOs for ratiometric dual-emitting thermometry. Our selection of the soaking post-functionalization technique underscores its simplicity, versatility, and adaptability for optimized dye integration and a broader dye selection, aligning well with diverse application needs and scalability for mass production. We acknowledge the existence of an alternative synthetic strategy, where dyes are integrated during the PMO synthesis, potentially offering more uniform dye distribution.⁴⁵ However, this alternative could introduce challenges, such as a narrower dye selection and increased synthesis complexity. It is crucial to note that our investigation was deliberately focused on the post-functionalization approach, without exploring the comparative merits of the in-synthesis dye incorporation, hence a direct comparison remains outside the scope of this study.

Furthermore, despite the excitation and emission wavelengths' limitation to the visible range potentially limiting some biomedical applications, the unique properties of these materials open up possibilities, particularly in precise cellular temperature measurements within laboratory settings. The ability to accurately track and comprehend intracellular temperature fluctuations is vital for delving into cellular functions, metabolic activities, and reactions to external stimuli. Employing ratiometric dual-emitting thermometry facilitated by RhB dye-incorporated curcumin PMOs offers a novel way for exploring cellular temperature dynamics. This information can contribute to advancements in cellular biology, drug delivery systems, temperature imaging, and the development of targeted therapies.⁴⁶

4.4 Conclusions

In conclusion, our research has successfully developed two novel ratiometric thermometers: curcumin-functionalized PMOs (C-PMO) and curcumin-pyrazole-functionalized PMOs (CP-PMO), both incorporating RhB as a model dye. The C-PMO serves as an excellent host matrix for RhB, ensuring efficient encapsulation and stability of the dye within its structure. This combination results in dual-emitting properties, leveraging the fluorescence emissions of both the curcumin linker and RhB for a temperature-dependent response. The C-PMO@RhB demonstrates a higher relative sensitivity compared to previous thermometers within the physiological temperature range and exhibits the least toxicity among the materials tested, making it particularly suitable for biomedical applications. Furthermore, the CP-PMO represents an advanced step in this research, introducing a modified curcumin-pyrazole linker. This modification enhances the temperature sensitivity of the composite, as indicated by its good maximum relative sensitivity. The incorporation of the curcumin-pyrazole linker in CP-PMO not only contributes to a diverse emission profile but also suggests potential for even broader applications

due to its enhanced thermal response. The synthesis of both C-PMO and CP-PMO, and their incorporation with RhB, mark an advancement in the realm of luminescent thermometry. These dual-emitting ratiometric thermometers offer innovative and promising approaches for accurate temperature sensing. The successful demonstration of these composites underscores their potential for practical applications and sets a precedent for future explorations in luminescent temperature sensing technologies.

4.5 Supporting information

Table S4.1 Preparation of PMO@dye.

Material (x=)	C-PMO@RhBx@LB		CP-PMO@RhBx@LB	
	Rhb (mg)	Water (mL)	Rhb (mg)	Water (mL)
1	0.1	2	0.1	2
2	0.1	4	0.1	10
3	0.1	10	0.1	20
4	0.1	20		

Table S4.2 Fitting parameters of prepared C-PMO and CP-PMO.

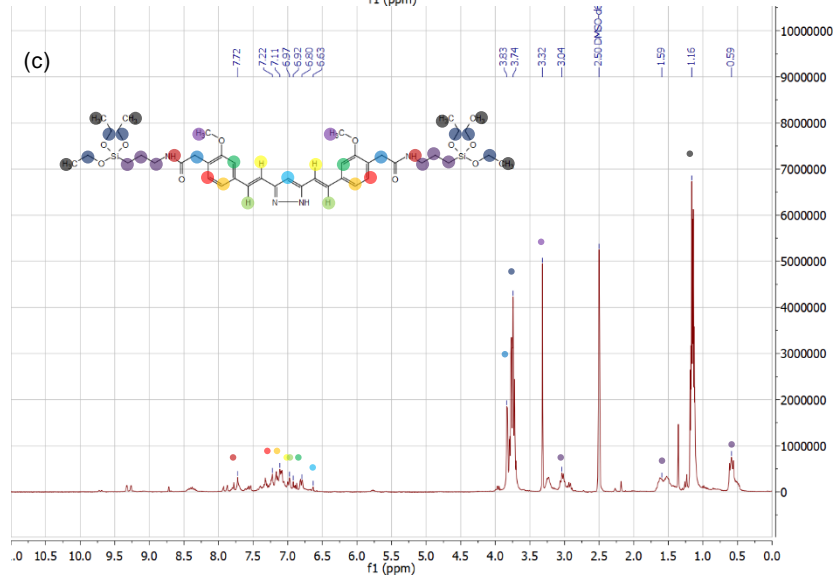
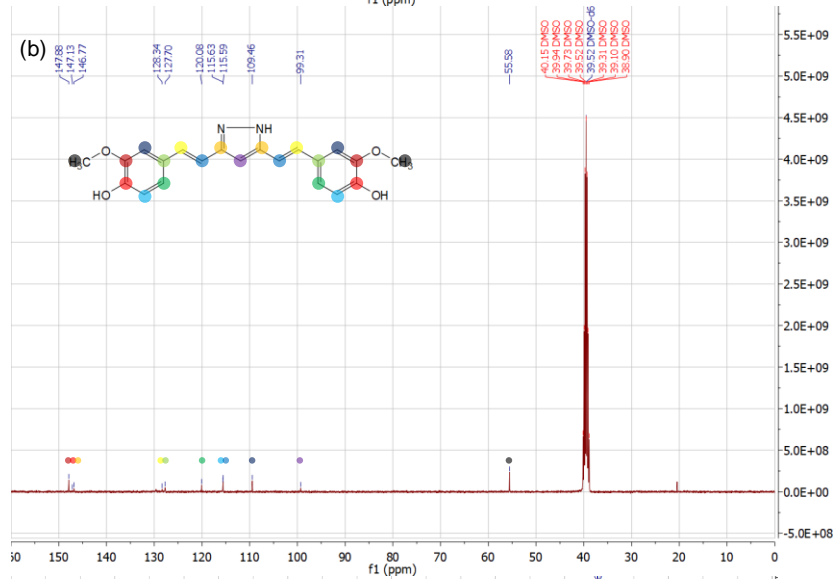
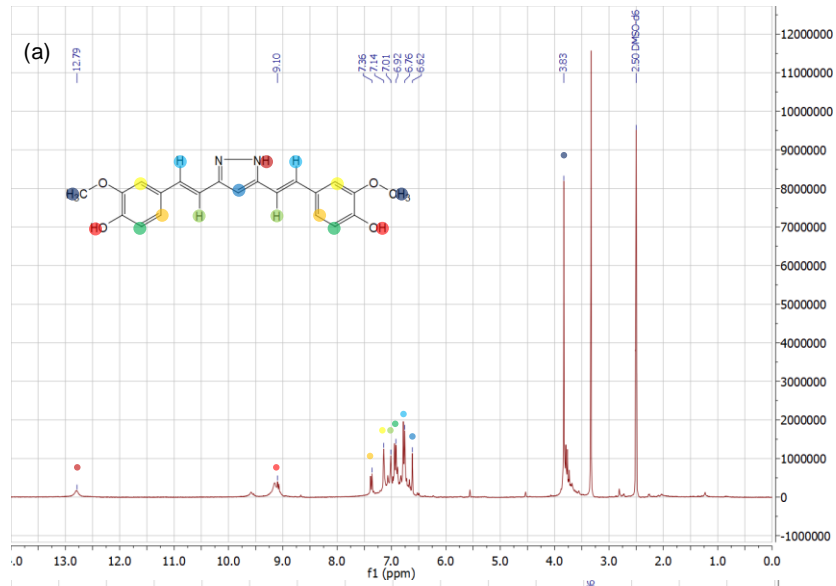
Material	Δ_0	α	ΔE (cm ⁻¹)
C-PMO@RhB3@LB	3.47	$3.13 \cdot 10^5$	3065.4
CP-PMO@RhB1@LB	0.41	$5.89 \cdot 10^5$	2936.5

Δ_0 is the thermometric parameter at $T = 0$ K.; $\alpha = W_0/W_R$ is the ratio between the nonradiative rates (W_0 is at $T = 0$ K) and radiative rates (W_R); ΔE is the activation energy of the nonradiative process.

Table S4.3. Comparison to the maximum relative sensitivities of several previously reported luminescent host-guest MOFs for temperature sensing.

Materials	Temperature range	Max S_r	T_m	Ref.
DSM@ZnPZDDI	298-338 K	$0.44 \% \cdot K^{-1}$	298 K	18
DSM@ZJU-56	298-343 K	$1.11 \% \cdot K^{-1}$	298 K	
Rh101@UiO-67	293-333 K	$1.30 \% \cdot K^{-1}$	333 K	5
ZJU-88 \rightarrow perylene	293-353 K	$1.28 \% \cdot K^{-1}$	293 K	47
TbTATAB \rightarrow C460	100-300 K	$4.484 \% \cdot K^{-1}$	300 K	48
CsPbBr ₃ @Eu-BTC	20-100 °C (293-373 K)	$3.9 \% \cdot K^{-1}$	20 °C (293 K)	49
RhB@IRMOF-3	20-70 °C (293-343 K)	$0.87 \% \cdot K^{-1}$	70 °C (343 K)	50
FL@IRMOF-3	20-80 °C (293-353 K)	$0.66 \% \cdot K^{-1}$	80 °C (353 K)	
Dye _{0.01} @Eu-BTC		$0.50 \% \cdot K^{-1}$	363 K	
Dye _{0.005} @Eu-BTC	283-363 K	$0.45 \% \cdot K^{-1}$	363 K	51
Dye _{0.001} @Eu-BTC		$0.30 \% \cdot K^{-1}$	363 K	
RhB@ZnNDPA	30-90 °C (303-363 K)	$0.42 \% \cdot K^{-1}$	30 °C (303 K)	16
ZJU-21 \rightarrow DMASM	20-80 °C (293-353 K)	$5.20 \% \cdot K^{-1}$	20 °C (293 K)	17
C-PMO@RhB@LB	293-343 K	$1.69 \% \cdot K^{-1}$	343 K	
CP-PMO@RhB@LB	293-343 K	$2.60 \% \cdot K^{-1}$	343 K	This work

S_r is relative sensitivity; T_m is temperature when S_r is maximum.



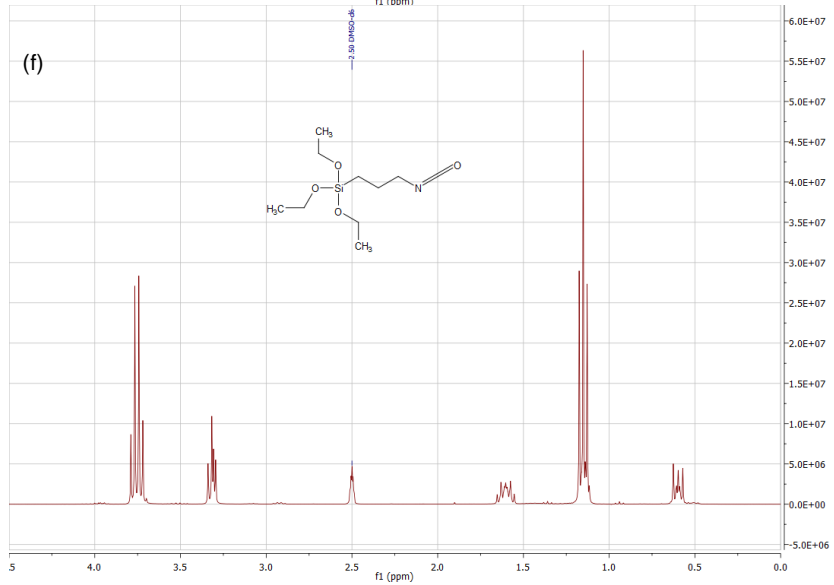
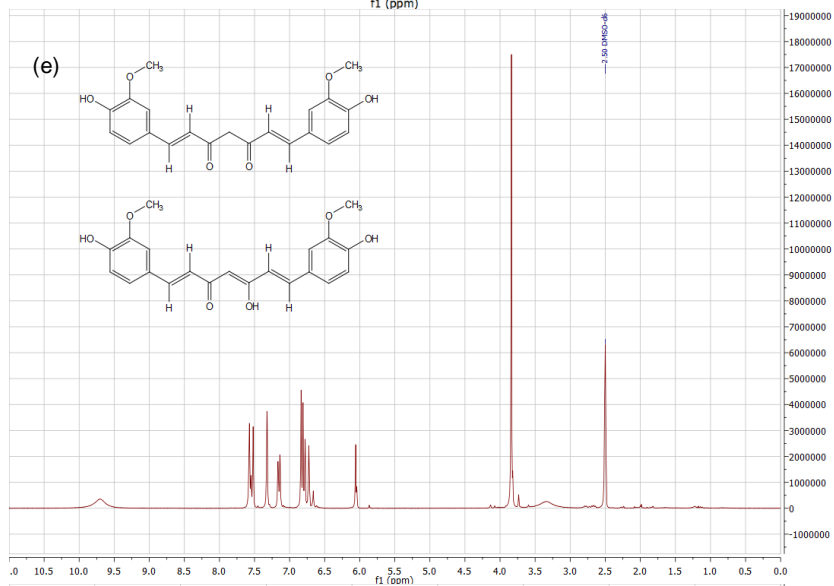
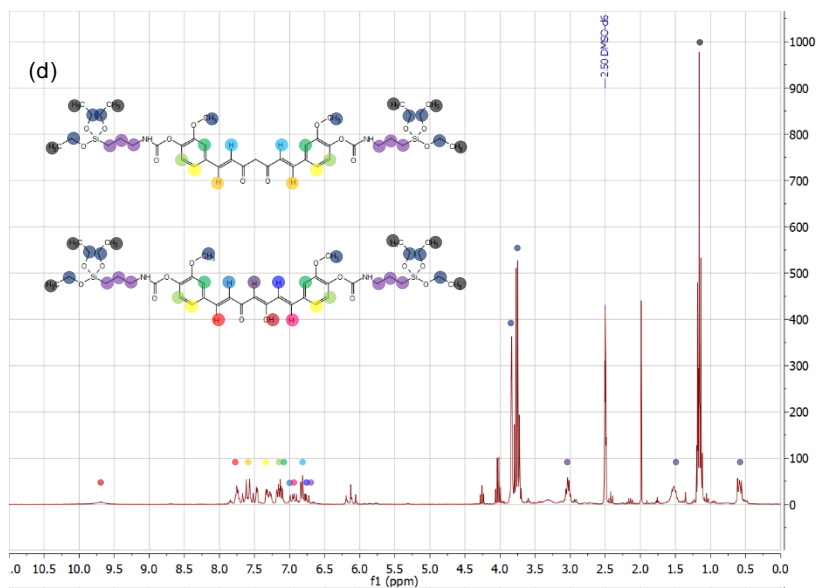


Figure S 4.1 ^1H NMR of (a) curcumin-pyrazole analog, 1c; (c) curcumin-pyrazole-Si, 1d; (d) curcumin-Si, 1b (e) curcumin, 1a; (f) (3-Isocyanatopropyl) triethoxysilane (IPTES), and ^{13}C NMR of (b) curcumin-pyrazole analog, 1c.

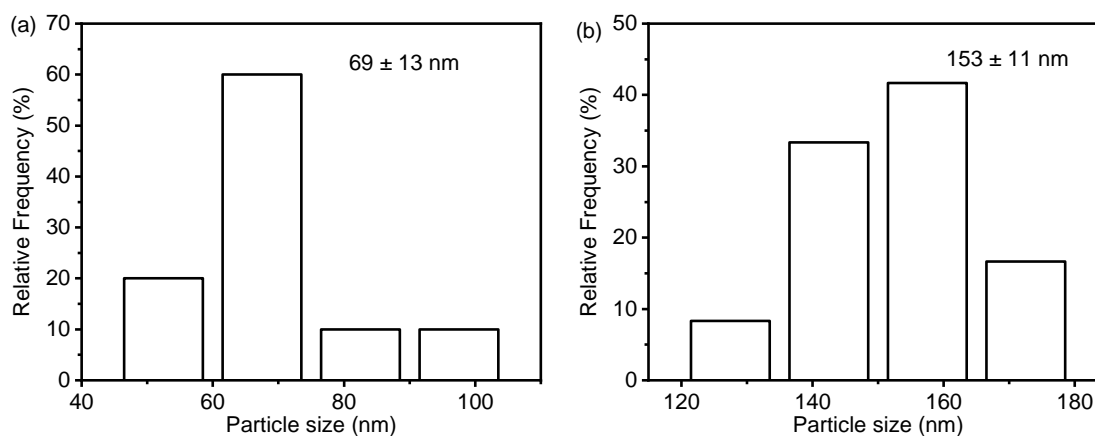


Figure S 4.2 Histograms showing the particle size distribution of: (a) C-PMO; (b) CP-PMO. The particle size is based on collected TEM images.



Figure S 4.3 Photograph of the prepared PMO@RhB@LB samples at (a) daylight (up) and when placed under a laboratory UV lamp with an excitation wavelength of 365 nm (down); (b) 293 K (20 °C) in water (up), and 343 K (70 °C) in water (down) under a laboratory UV lamp of 365 nm excitation.

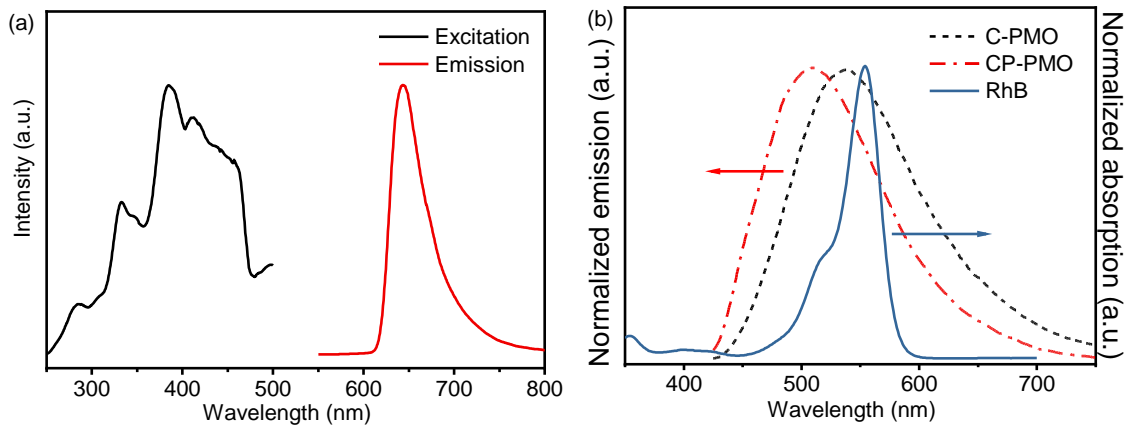


Figure S 4.4 (a) Excitation and emission spectra of RhB in water at room temperature (excited at 385 nm observed at 641 nm). (b) Emission spectra of the two PMOs – C-PMO AND CP-PMO (excited at 417 nm) and UV-vis absorption spectrum of RhB in water at room temperature.

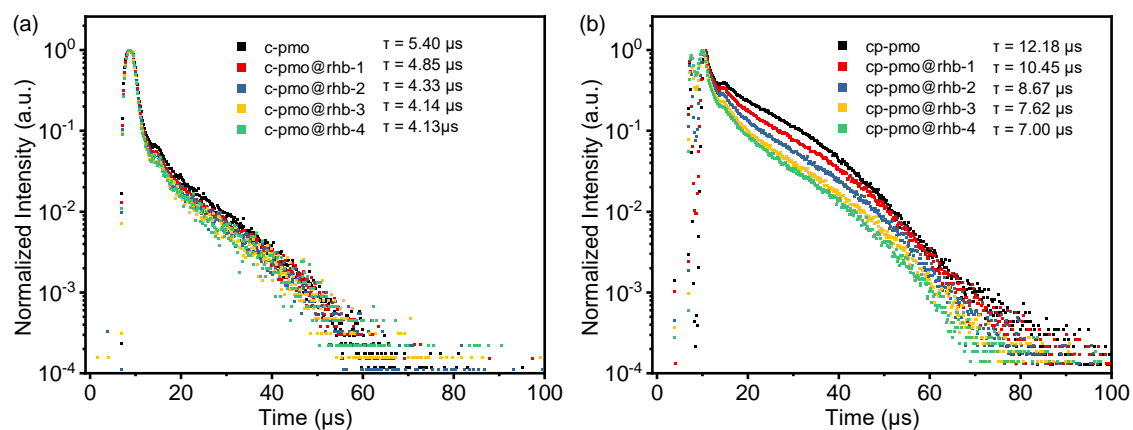


Figure S 4.5 Luminescence decay profiles of (a) C-PMO, and (b) CP-PMO in water upon added increasing concentrations of RhB water solution, ex = 417 nm, em = 525 nm (τ : average decay time).

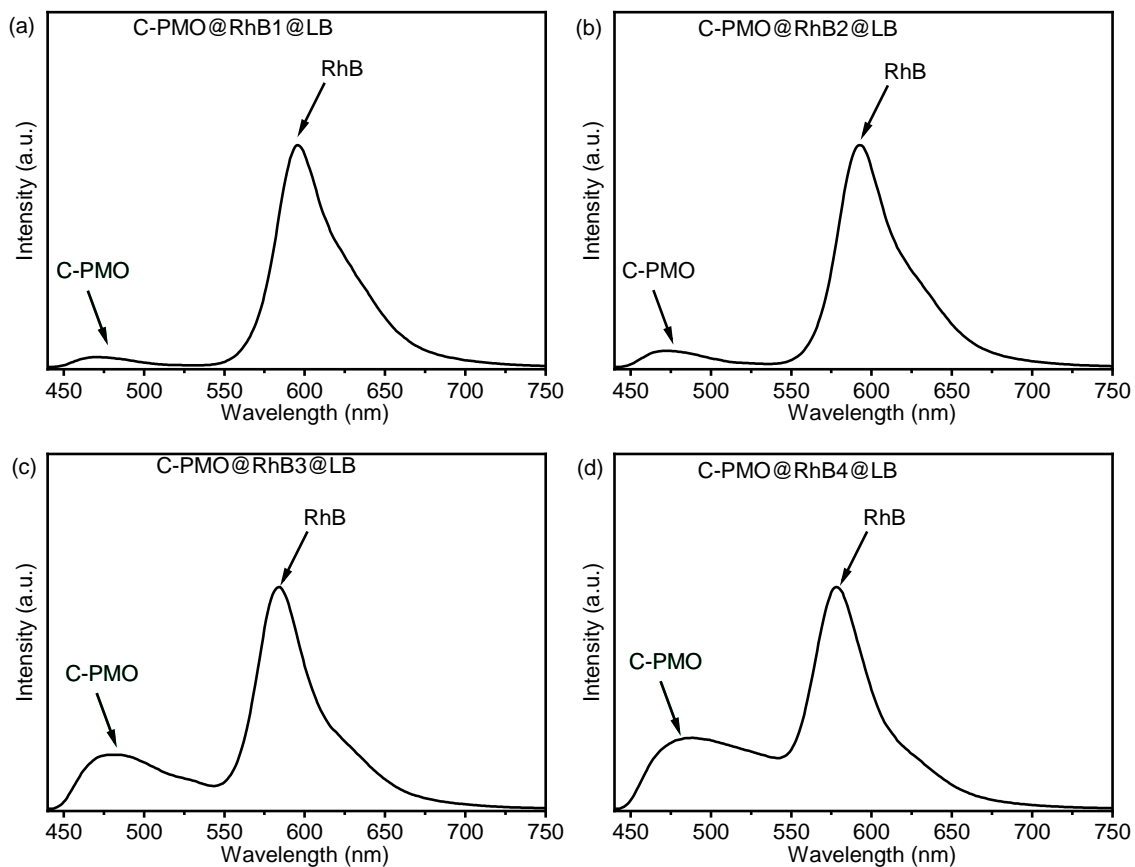


Figure S 4.6 Emission spectra of C-PMO@RhB with different dye contents in water excited at 417 nm.

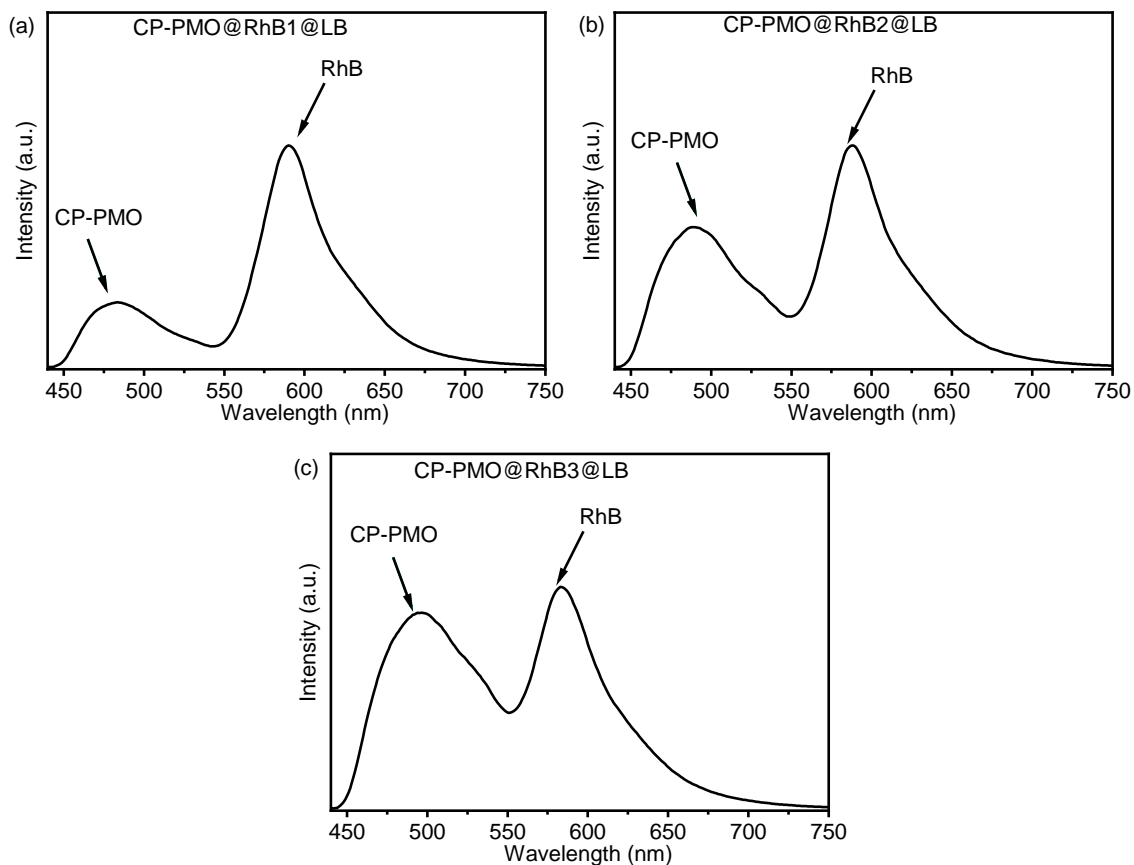


Figure S 4.7 Emission spectra of CP-PMO@RhB with different dye contents in water excited at 417 nm.

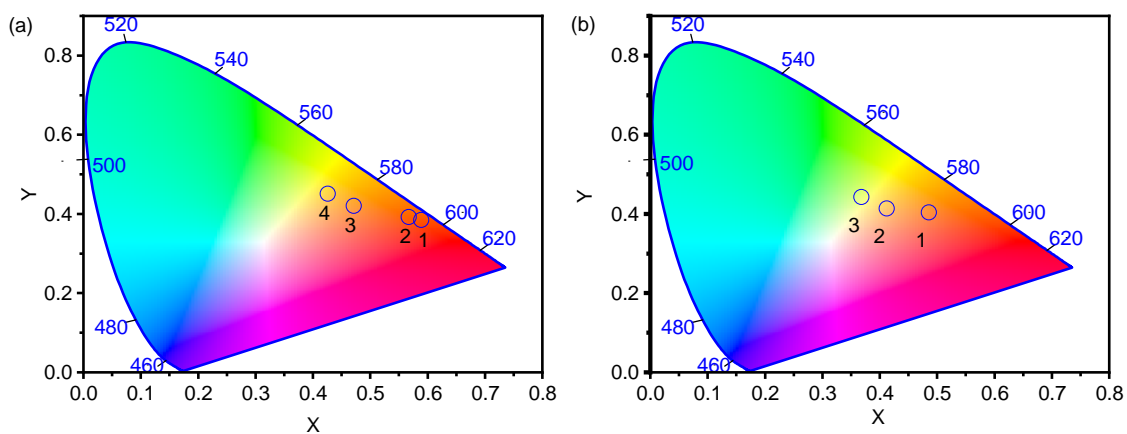


Figure S 4.8 CIE chromaticity diagram for (a) C-PMO@RhB_x@LB (x=1~4) and (b) C-PMO@RhB_x@LB (x=1~3) with decreasing dye contents excited at 417 nm.

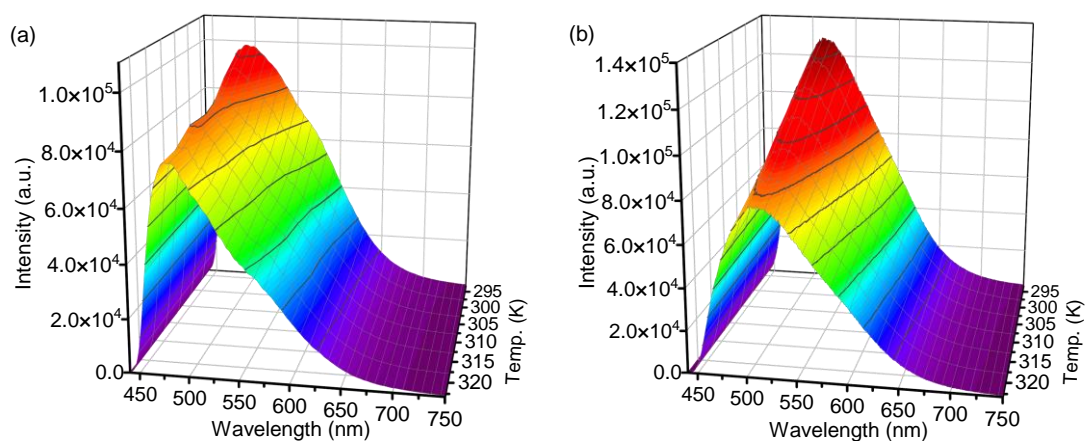


Figure S 4.9 Temperature-dependent emission spectra of (a) C-PMO and (b) CP-PMO dispersed in water recorded from 293.15 to 323.15 K, excited at 417 nm.

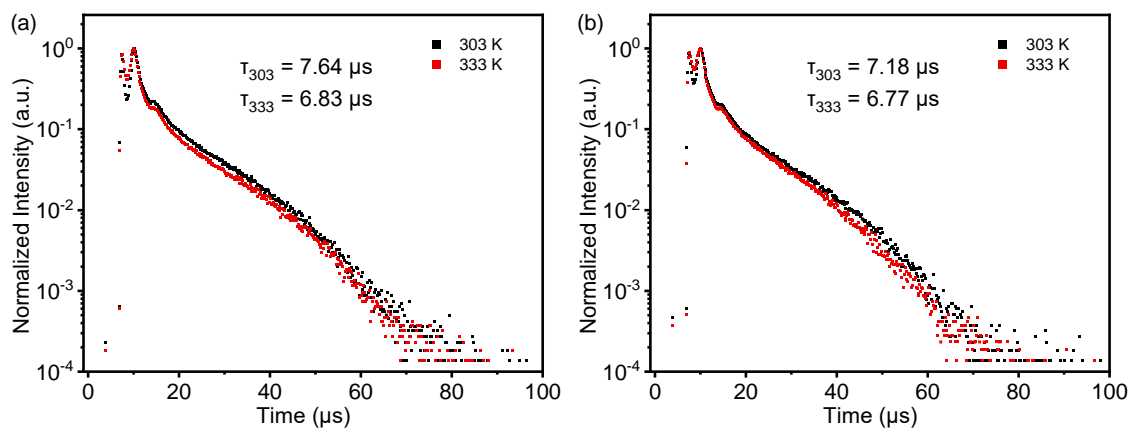


Figure S 4.10 Luminescence decay profile of (a) C-PMO in water, ex = 417 nm, em = 539 nm; (b) CP-PMO in water, ex = 417 nm, em = 533 nm.

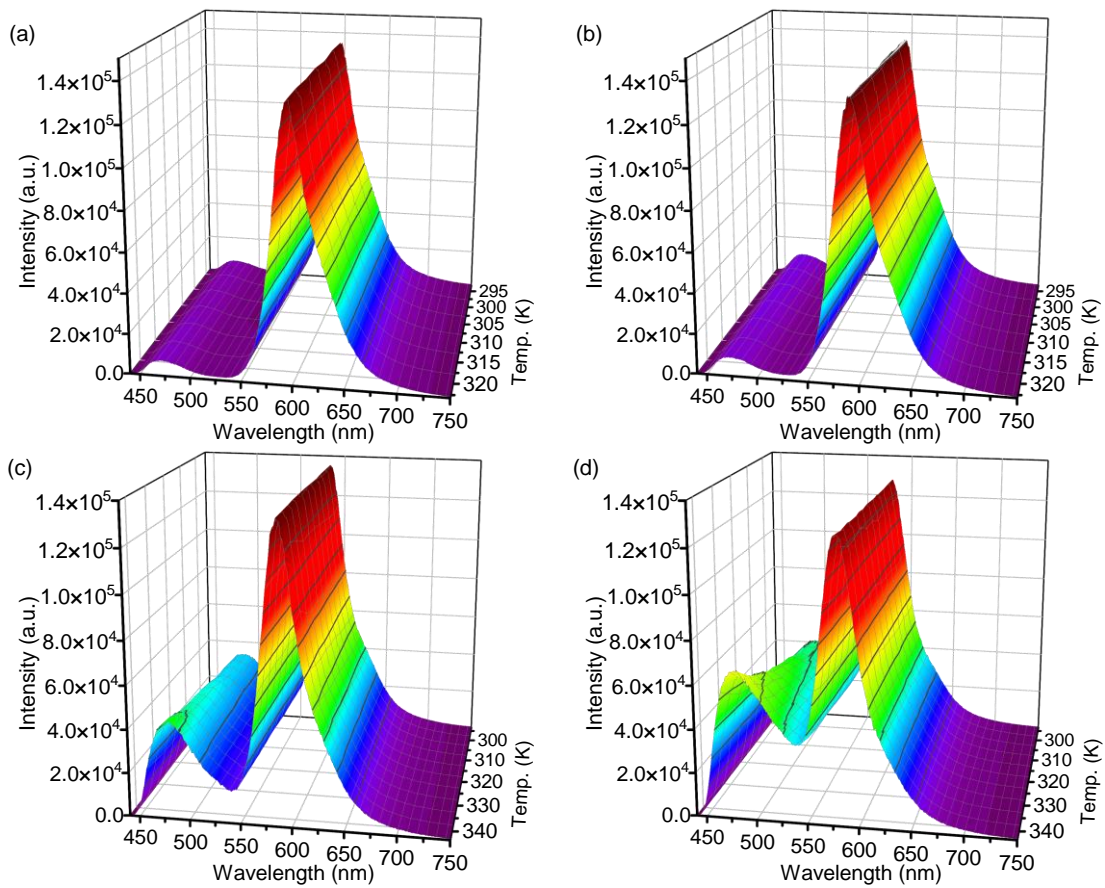


Figure S 4.11 Normalized Emission spectra of C-PMO@RHB@LB with different dye contents (C-PMO@RhBx@LB, x = 1 - 4) in water recorded from 293.15 to 343.15 K, excited at 417 nm.

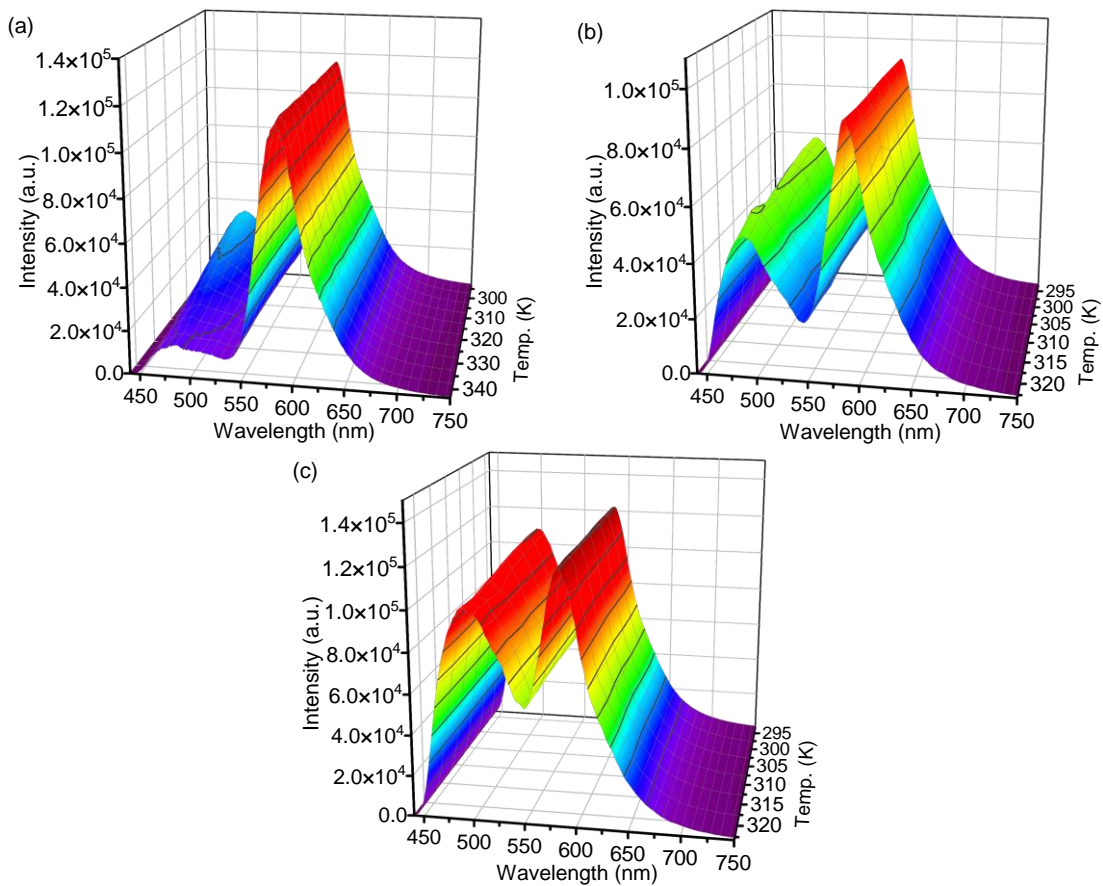


Figure S 4.12 Normalized Emission spectra of CP-PMO@RHB@LB with different dye contents (CP-PMO@RhB_x@LB, x = 1 - 3) in water recorded from 293.15 to 343.15 K, excited at 417 nm.

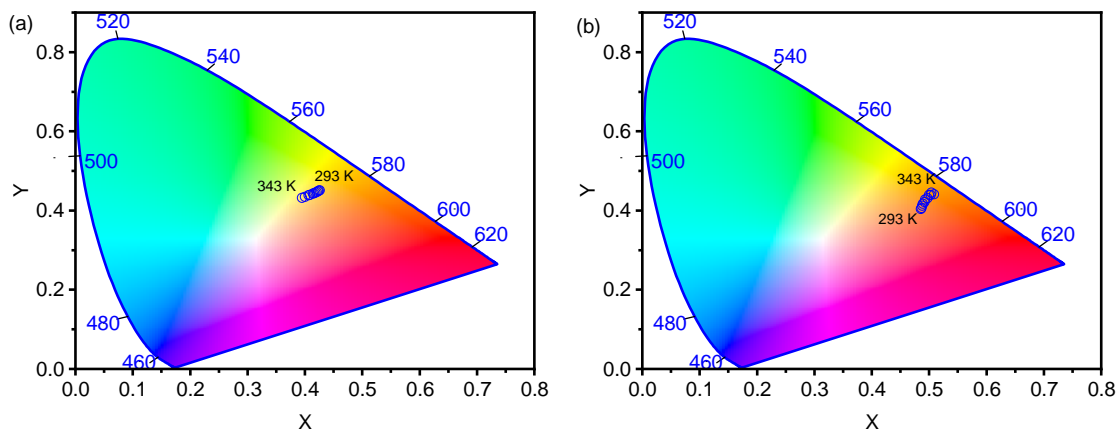


Figure S 4.13 CIE coordinates diagram for (a) C-PMO@RhB@LB; (b) CP-PMO@RhB@LB at different temperatures (293–343 K).

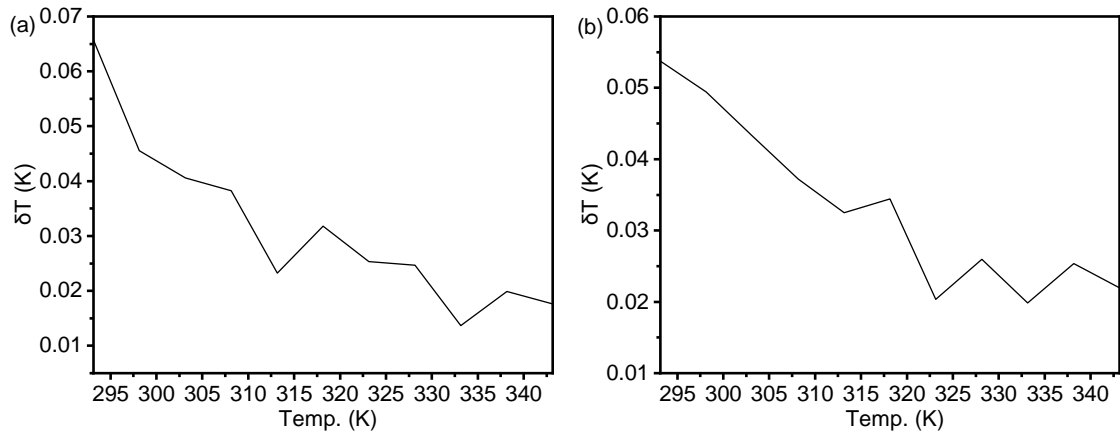


Figure S 4.14 Temperature uncertainty for (a) C-PMO@RhB@LB; (b) CP-PMO@RhB@LB at varying temperatures (293-343 K).

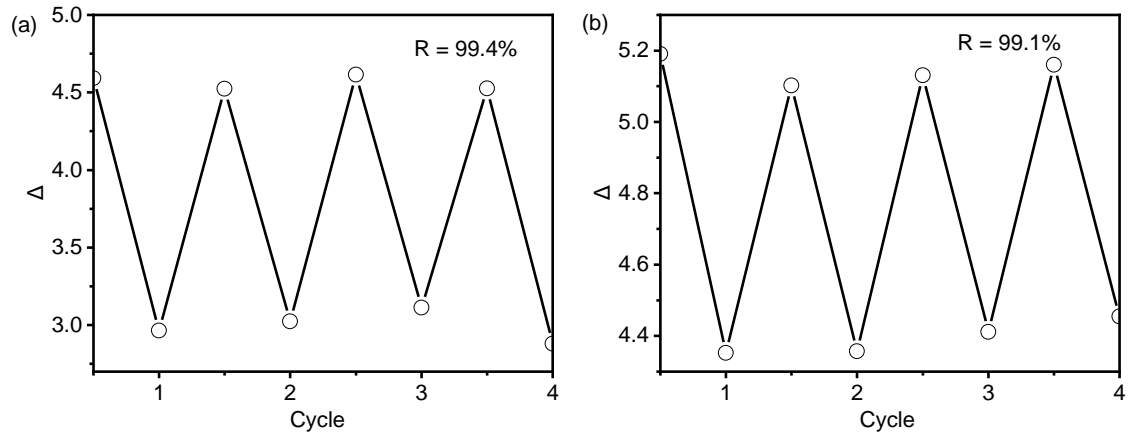


Figure S 4.15 Cycle tests for (a) C-PMO@RhB@LB, and (b) CP-PMO@RhB@LB (R - repeatability).

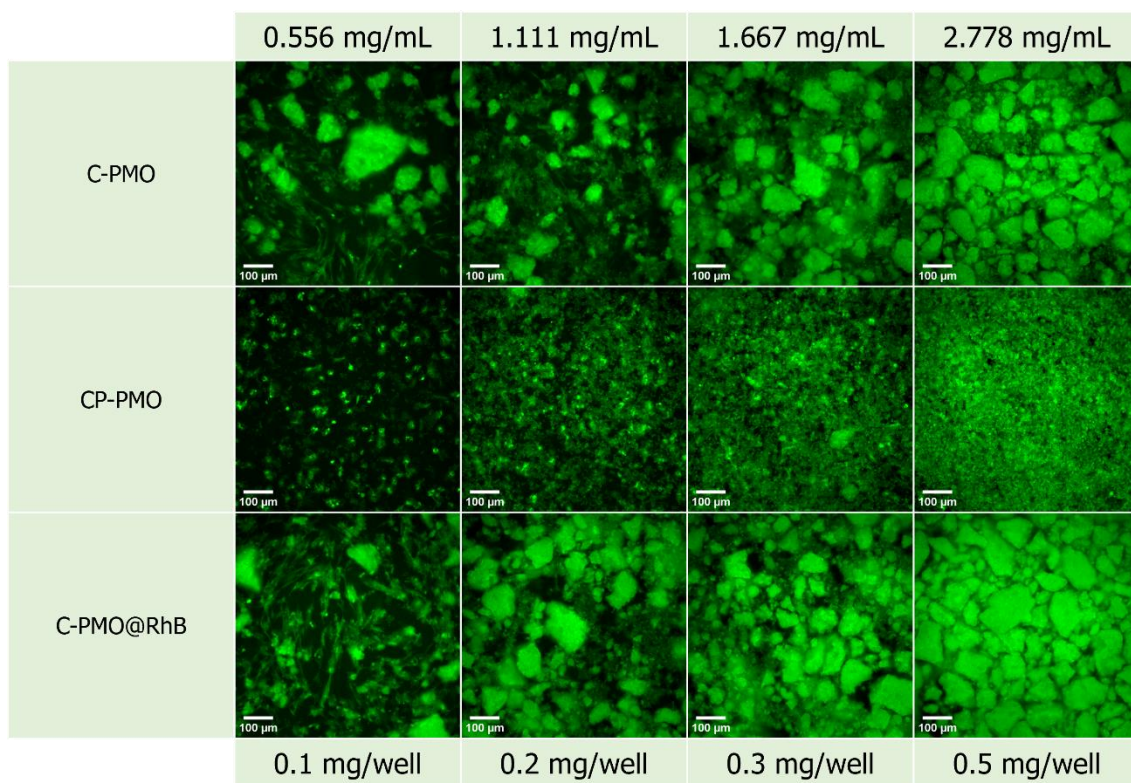


Figure S 4.16 Fluorescence microscopy images of the technical replicates with stained NHDF cells for the three samples (C-PMO, CP-PMO, C-PMO@RhB@LB) in the range of 0.1-0.5 mg/well. Calcein-AM was used as the cell stain at a final well concentration of 1.5 μ M. All scale bars are set to 100 μ m.

4.6 Reference

1. X. D. Wang, O. S. Wolfbeis and R. J. Meier, *Chem Soc Rev*, 2013, **42**, 7834-7869.
2. D. I. Bradley, R. E. George, D. Gunnarsson, R. P. Haley, H. Heikkinen, Y. A. Pashkin, J. Penttila, J. R. Prance, M. Prunnila, L. Roschier and M. Sarsby, *Nat. Commun.*, 2016, **7**, 10455.
3. A. M. Kaczmarek, H. S. Jena, C. Krishnaraj, H. Rijckaert, S. K. P. Veerapandian, A. Meijerink and P. Van Der Voort, *Angew Chem Int Ed Engl*, 2021, **60**, 3727-3736.
4. A. Bednarkiewicz, L. Marciniak, L. D. Carlos and D. Jaque, *Nanoscale*, 2020, **12**, 14405-14421.
5. Y. Zhou, D. Zhang, J. Zeng, N. Gan and J. Cuan, *Talanta*, 2018, **181**, 410-415.
6. H. Suo, X. Zhao, Z. Zhang, Y. Wang, J. Sun, M. Jin and C. Guo, *Laser Photonics Rev.*, 2021, **15**, 2000319.
7. A. M. Kaczmarek, Y. Y. Liu, M. K. Kaczmarek, H. Liu, F. Artizzu, L. D. Carlos and P. Van Der Voort, *Angew Chem Int Ed Engl*, 2020, **59**, 1932-1940.
8. Y. Cheng, Y. Gao, H. Lin, F. Huang and Y. S. Wang, *J Mater Chem C*, 2018, **6**, 7462-7478.
9. C. D. S. Brites, P. P. Lima, N. J. O. Silva, A. Millan, V. S. Amaral, F. Palacio and L. D. Carlos, *New J Chem*, 2011, **35**, 1177-1183.
10. G. Liu, D. Liu, X. Han, X. Sheng, Z. Xu, S. H. Liu, L. Zeng and J. Yin, *Talanta*, 2017, **170**, 406-412.
11. H. L. Zeng, Y. L. Zhu, L. L. Ma, X. H. Xia, Y. H. Li, Y. Ren, W. Y. Zhao, H. Yang and R. J. Deng, *Dyes Pigm.*, 2019, **164**, 35-42.
12. Y. Wu, J. Liu, J. Ma, Y. Liu, Y. Wang and D. Wu, *ACS Appl. Mater. Interfaces*, 2016, **8**, 14396-14405.
13. C. D. S. Brites, P. P. Lima, N. J. O. Silva, A. Millan, V. S. Amaral, F. Palacio and L. D. Carlos, *Nanoscale*, 2012, **4**, 4799-4829.
14. W. J. Chi, W. T. Yin, Q. K. Qi, Q. L. Qiao, Y. Y. Lin, Z. H. Zhu, S. Vijayan, M. Hashimoto, G. Udayakumar, Z. C. Xu and X. G. Liu, *Mater. Chem. Front.*, 2017, **1**, 2383-2390.
15. M. Peng, A. M. Kaczmarek and K. Van Hecke, *ACS Appl. Mater. Interfaces*, 2022, **14**, 14367-14379.
16. M. Y. Gong, Z. J. Li, W. Q. Xiang, T. F. Xia and D. Zhao, *J Solid State Chem*, 2022, **311**, 123147.
17. D. Zhao, D. Yue, K. Jiang, Y. Cui, Q. Zhang, Y. Yang and G. Qian, *J Mater Chem C*, 2017, **5**, 1607-1613.
18. S. Wang, M. Gong, X. Han, D. Zhao, J. Liu, Y. Lu, C. Li and B. Chen, *ACS Appl. Mater. Interfaces*, 2021, **13**, 11078-11088.
19. T. Asefa, M. J. MacLachlan, N. Coombs and G. A. Ozin, *Nature*, 1999, **402**, 867-871.
20. S. Inagaki, S. Guan, Y. Fukushima, T. Ohsuna and O. Terasaki, *J. Am. Chem. Soc.*, 1999, **121**, 9611-9614.
21. B. J. Melde, B. T. Holland, C. F. Blanford and A. Stein, *Chem. Mater.*, 1999, **11**, 3302-3308.
22. P. Van der Voort, D. Esquivel, E. De Canck, F. Goethals, I. Van Driessche and F. J. Romero-Salguero, *Chem. Soc. Rev.*, 2013, **42**, 3913-3955.
23. S. Datz, H. Engelke, C. V. Schirnding, L. Nguyen and T. Bein, *Microporous Mesoporous Mater.*, 2016, **225**, 371-377.
24. S. Mishra, S. Patel and C. G. Halpani, *Chem Biodivers*, 2019, **16**, e1800366.
25. H. Rijckaert, S. Premcheska, S. Mohanty, J. Verduijn, A. Skirtach and A. M. Kaczmarek, *Physica B Condens. Matter*, 2022, **626**, 413453.
26. A. M. Kaczmarek, R. Van Deun and M. K. Kaczmarek, *Sens. Actuators B Chem.*, 2018, **273**, 696-702.
27. N. Ahsan, S. Mishra, M. K. Jain, A. Surolia and S. Gupta, *Sci. Rep.*, 2015, **5**, 1-16.
28. P. K. Mohan, G. Sreelakshmi, C. Muraleedharan and R. Joseph, *Vib Spectrosc*, 2012, **62**, 77-84.
29. M. Ahmed, M. A. Qadir, A. Hameed, M. N. Arshad, A. M. Asiri and M. Muddassar, *Bioorg. Chem.*, 2018, **76**, 218-227.
30. R. M. Dukali, I. M. Radovic, D. B. Stojanovic, D. M. Sevic, V. J. Radojevic, D. M. Jovic and R. R. Aleksic, *J. Serbian Chem. Soc.*, 2014, **79**, 867-880.

31. M. Abboud and A. Sayari, *Microporous Mesoporous Mater.*, 2017, **249**, 157-164.
32. M. Gao, C. Xing, X. Jiang, L. Xu, P. Li and C. D. Hsiao, *Luminescence*, 2021, **36**, 951-957.
33. B. Guan, Y. Cui, Z. Ren, Z. A. Qiao, L. Wang, Y. Liu and Q. Huo, *Nanoscale*, 2012, **4**, 6588-6596.
34. T. Fujii, K. Kodaira, O. Kawauchi, N. Tanaka, H. Yamashita and M. Anpo, *J. Phys. Chem. B*, 1997, **101**, 10631-10637.
35. K. I. Priyadarsini, *J. Photochem. Photobiol. C*, 2009, **10**, 81-95.
36. Y. Erez, I. Presiado, R. Gepshtein and D. Huppert, *J Phys Chem A*, 2011, **115**, 10962-10971.
37. S. L. Logunov, T. M. Masciangioli, V. F. Kamalov and M. A. El-Sayed, *J. Phys. Chem. B*, 1998, **102**, 2303-2306.
38. M. Y. Berezin and S. Achilefu, *Chem Rev*, 2010, **110**, 2641-2684.
39. S. Inagaki, O. Ohtani, Y. Goto, K. Okamoto, M. Ikai, K. Yamanaka, T. Tani and T. Okada, *Angew Chem Int Ed Engl*, 2009, **48**, 4042-4046.
40. S. M. Radiul, J. Chowdhury, A. Goswami and S. Hazarika, *Laser Phys*, 2022, **32**, 075602.
41. A. M. Kaczmarek, J. Liu, B. Laforce, L. Vincze, K. Van Hecke and R. Van Deun, *Dalton Trans.*, 2017, **46**, 5781-5785.
42. J. Rocha, C. D. Brites and L. D. Carlos, *Chem. Eur. J.*, 2016, **22**, 14782-14795.
43. H. Rijckaert and A. M. Kaczmarek, *ChemComm*, 2020, **56**, 14365-14368.
44. C. Brites, A. Millán and L. Carlos, in *Handbook on the Physics and Chemistry of Rare Earths*, Elsevier, 2016, vol. 49, pp. 339-427.
45. T. Tani, N. Mizoshita and S. Inagaki, *J. Mater. Chem.*, 2009, **19**, 4451-4456.
46. X. Huang, J. Song, B. C. Yung, X. Huang, Y. Xiong and X. Chen, *Chem. Soc. Rev.*, 2018, **47**, 2873-2920.
47. Y. Cui, R. Song, J. Yu, M. Liu, Z. Wang, C. Wu, Y. Yang, Z. Wang, B. Chen and G. Qian, *Adv. Mater.*, 2015, **27**, 1420-1425.
48. T. Xia, T. Song, Y. Cui, Y. Yang and G. Qian, *Dalton Trans.*, 2016, **45**, 18689-18695.
49. J. Liu, Y. Zhao, X. Li, J. Wu, Y. Han, X. Zhang and Y. Xu, *Cryst. Growth Des.*, 2019, **20**, 454-459.
50. C. He, H. Yu, J. Sun, C. Zhou, X. Li, Z.-M. Su, F. Liu and V. Khakhinov, *Dyes Pigm.*, 2022, **198**, 110000.
51. J. Liu, X. Yue, Z. Wang, X. Zhang and Y. Xu, *J Mater Chem C*, 2020, **8**, 13328-13335.

CHAPTER 5. Conclusion and Perspectives

This dissertation has advanced the field of luminescent periodic mesoporous organosilicas (LPMOs) by exploring their synthesis, functionalization, and application in sensing, catalysis, and temperature monitoring.

Chapter 2 describes the development of a novel yolk-shell structure based on lanthanide periodic mesoporous organosilica (LnPMO) for luminescence turn-off sensing of Hg^{2+} ions. This innovative design combines the advantages of LnPMOs (broad detection range) with the high sensitivity of upconversion luminescent nanoparticles (UCNPs) to achieve efficient and selective detection of mercury ions in water. We successfully fabricated a well-defined yolk-shell structure with a Tb^{3+} -complex grafted diureido-benzoicacid hollow PMO (shell) and $\text{NaYF}_4:\text{Yb,Er}$ (UCNP, yolk) exhibiting both downshifting (DS) and upconversion (UC) luminescence. This design allowed for the integration of the Hg^{2+} -responsive Rhodamine B thiolactone (RBT) dye within the yolk-shell structure, enabling sensitive detection in the upconversion mode. Importantly, the downshifting sensing functionality of the Tb^{3+} complex grafted PMO was preserved even after UCNP incorporation.

Chapter 3 presented the development and application of a novel platform: acac-functionalized periodic mesoporous organosilicas (acac-PMOs). These materials offer promise for diverse applications in luminescence ion sensing and catalysis. The successful synthesis of a new acac-bridged bissilane precursor (acac-Si) enabled the creation of acac-PMOs capable of grafting metal complexes. This work demonstrates the potential of acac-PMOs for various applications. A new synthetic approach was established, providing a robust platform for incorporating acac functionalities within the PMO framework. Eu^{3+} -grafted acac-PMO exhibited initial promise for ion sensing applications, although further research is needed to optimize its selectivity and sensitivity towards specific target ions. Additionally, vanadyl (VO^{2+}) grafted acac-PMO demonstrated catalytic activity in a model

Mannich-type reaction, highlighting the potential of acac-PMOs as recyclable and efficient catalysts for various organic transformations.

Chapter 4 investigated the potential of PMOs and organic dyes for application in a novel ratiometric thermometry system. The miniaturization of technology has created a growing demand for nanoscale temperature sensing techniques, particularly in fields like biomedicine, where traditional contact thermometers have limitations. Luminescence-based thermometry offers a promising solution due to its simplicity, high sensitivity, and exceptional spatial and temporal resolution. This work focused on developing a ratiometric approach, which utilizes the intensity ratio of two distinct emission peaks for enhanced sensing performance.

Organic dyes have emerged as attractive materials for ratiometric thermometry due to their advantageous properties. This study explored the use of curcumin, a natural polyphenol with well-known fluorescent properties. Curcumin-functionalized PMOs (C-PMO) and a modified curcumin-pyrazole functionalized PMO (CP-PMO) system were successfully synthesized. PMO materials exhibited highly temperature-dependent fluorescence. To create dual-emitting nanocomposites, RhB dye was encapsulated within the PMO pores. A lipid bilayer (LB) coating was then applied to enhance biocompatibility and prevent dye leaching. The resulting C-PMO@RhB@LB and CP-PMO@RhB@LB systems demonstrated good maximum relative sensitivity (S_r) within the physiological temperature range. This finding highlights the effectiveness of incorporating organic dyes into the PMO framework, which enhances dye stability and reduces photobleaching. The addition of the lipid bilayer coating further strengthens the platform's suitability for biocompatible and sensitive temperature sensing applications.

Perspectives

This dissertation has laid a base for advancements in LPMO research. Looking towards the next five years, several specific directions offer the potential for significant breakthroughs:

Chapter 2: Yolk-Shell LPMOs for Hg²⁺ Sensing - Going Ultra-Sensitive and Multiplexed

The current research on yolk-shell LPMOs for Hg²⁺ detection demonstrates promising sensitivity. The next challenge is to achieve ultra-low detection limits (LODs) below 10 nM, competing with the performance of state-of-the-art techniques. Future research directions include exploring methods to improve sensitivity by optimizing the UCNP composition and RBT loading within the yolk-shell structure. Additionally, investigating the influence of different ancillary ligands on the performance of the Tb³⁺ complex grafted PMO in the downshifting mode would be beneficial. Evaluating the sensor's selectivity for Hg²⁺ ions in complex environmental and biological samples is crucial for real-world applications. Finally, developing a practical method for utilizing the yolk-shell sensor for real-time Hg²⁺ detection in water samples would be a contribution to environmental and industrial monitoring.

A critical direction for the next phase of research is to expand the yolk-shell sensor's capabilities beyond single-analyte detection. By incorporating multiple responsive dyes within the yolk-shell structure and utilizing advanced signal processing algorithms, researchers can develop a versatile sensing platform capable of simultaneous detection of various heavy metal ions, including mercury, lead, and cadmium, in complex environmental samples. Achieving this milestone would revolutionize environmental monitoring practices, providing comprehensive insights into water quality and facilitating timely interventions to safeguard public health.

Chapter 3: Acac-Functionalized LPMOs for Sensing and Catalysis - Expanding the Horizons

The potential of acac-PMOs extends beyond ion sensing. The next steps involve exploring their application for the detection of other crucial analytes such as biomolecules (glucose, cholesterol) or environmental pollutants (nitrates, phosphates). This can be achieved by incorporating specific recognition units like aptamers or antibodies within the PMO framework or by designing responsive organic fluorophores that interact selectively with the target analyte.

Integrating transition metal complexes as functional molecules has the potential to create LPMOs with enhanced catalytic activity for various organic transformations, such as C-C bond formation reactions and selective oxidation processes. Furthermore, detailed mechanistic investigations are crucial to understand the role of acac functionalities in both ion sensing and catalysis processes within acac-PMOs.

Recent research explores exciting new applications for lanthanide-based PMOs (LnPMOs) beyond their established role. These include nanoscale thermometry due to their unique luminescence properties, and solvent sensing through their responsiveness to environmental shifts. Additionally, LnPMOs hold promise for photodynamic therapy (PDT) by incorporating photosensitizers for light-activated cancer treatment. Their inherent porous structure further allows for drug encapsulation and controlled release, with potential for targeted delivery through further functionalization. This research paves the way for LnPMOs to play a significant role in diverse fields.

Chapter 4: PMO-Dye Nanocomposites for Thermometry - In vivo and Clinical Applications

The future of PMO-dye nanocomposites lies in in vivo temperature monitoring within living organisms. This necessitates addressing biocompatibility concerns and developing strategies for targeted delivery of the nanocomposite to specific tissues using biocompatible polymers or functionalization with targeting moieties. Investigating the long-term stability of PMO-dye nanocomposites under physiological conditions is crucial. This involves studying potential degradation pathways, dye leaching, and the performance of the lipid bilayer coating over extended timeframes. Finally, the development of clinical-grade PMO-dye nanocomposites for real-time temperature monitoring during minimally invasive surgeries or for monitoring localized inflammation within the body holds immense promise. However, this necessitates rigorous biocompatibility testing and navigating regulatory approval processes.

By pursuing these specific directions, LPMO research can unlock their full potential for a multitude of sensing, catalysis, and thermometry applications, with significant implications for environmental monitoring, healthcare diagnostics, and technological advancements.